UNITED NATIONS EDUCATIONAL, SCIENTIFIC AND CULTURAL ORGANIZATION
INTERNATIONAL ATOMIC ENERGY AGENCY
INTERNATIONAL CENTRE FOR THEORETICAL PHYSICS
I.C.T.P., P.O. BOX 586, 34100 TRIESTE, ITALY, CABLE: CENTRATOM TRIESTE

H4.SMR/916 - 39

SEVENTH COLLEGE ON BIOPHYSICS:

Structure and Function of Biopolymers: Experimental and Theoretical Techniques.

4 - 29 March 1996

Protein Structure and Molecular Recognition

S. Subramaniam

University of Illinois at Urbana Champaign
Urbana, U.S.A.

Centre for Biophysics and Computational Biology
Dept. of Physiology and Biophysics,
National Center for Supercomputing Applications

PROTEINS: Structure, Function, and Genetics 18:231–245 (1994)

Treatment of Electrostatic Effects in Proteins: Multigrid-Based Newton Iterative Method for Solution of the Full Nonlinear Poisson–Boltzmann Equation

Michael Holst,[1] Richard E. Kozack,[2] Faisal Saied,[1] and Shankar Subramaniam[2,3]
[1]Numerical Computing Group, Department of Computer Science and [2]Center for Biophysics and Computational Biology, Department of Physiology and Biophysics, National Center for Supercomputing Applications, [3]Beckman Institute for Advanced Science and Technology, University of Illinois at Urbana-Champaign, Urbana, Illinois 61801

ABSTRACT **The nonlinear Poisson–Boltzmann equation (NPBE) provides a continuum description of the electrostatic field in an ionic medium around a macromolecule. Here, a novel approach to the solution of the full NPBE is developed. This robust and efficient algorithm combines multilevel techniques with a damped inexact Newton's method. The CPU time required for solution of the full NPBE, which is less than that for standard single-grid approaches in solving the corresponding linearized equation, is proportional to the number of unknowns enabling applications to very large macromolecular systems. Convergence of the method is demonstrated for a variety of protein systems. Comparison of the solutions to the linearized Poisson–Boltzmann equation shows that the damping of the electrostatic field around the charge is increased and that the potential scales logarithmically with charge. The inclusion of the full nonlinearity thus reduces the impact of highly charged residues on protein surfaces and provides a more realistic representation of electrostatic effects. This is demonstrated through calculation of potential around the active site regions of the 1,266-residue tryptophan synthase dimer and in the computation of rate constants from Brownian dynamics calculations in the superoxide dismutase–superoxide and antibody–antigen systems.**

Key words: nonlinear elliptic equations, nonlinear multigrid, inexact Newton methods, damped Newton methods, crambin, BPTI, HyHEL-5, superoxide dismutase, rhinovirus, tryptophan synthase, electrostatic steering, Brownian dynamics, antibody–antigen complex

INTRODUCTION

It is now clear that continuum models of molecules in ionic solutions, which were first proposed in 1923 by Debye and Hückel,[1] are invaluable for studying electrostatic interactions. Since the electrostatic behavior determines to a large degree the structure and kinetics of complex molecules such as proteins, modeling these interactions accurately is an important goal in biophysics[2–5] and molecular dynamics simulations.[6–8] The Debye–Hückel model is depicted in Figure 1. There are three relevant regions in the problem. In the solvent, which is assigned the dielectric constant of water, the charge density of the mobile ions is assumed to be given by a Boltzmann distribution. The molecule, from which ions are excluded, is taken to be a low dielectric region in which point charges are embedded. Often a third region, the Stern layer, is added to simulate the finite size of the ions in the electrolyte. Ions are excluded from the Stern layer, but the dielectric constant is equal to that of the solvent. These assumptions lead to the *nonlinear Poisson–Boltzmann equation* (NPBE), a three-dimensional second order nonlinear elliptic partial differential equation describing the electrostatic potential $\Phi(r)$ at a field position r. If we define a dimensionless potential by $u(r) = e_c\Phi(r)/k_BT$, then the NPBE for a 1:1 electrolyte can be written in the form:

$$-\nabla \cdot [\epsilon(r)\nabla u(r)] + \epsilon(r)\kappa^2(r)\sinh[u(r)] = \frac{e_c^2}{k_BT}\sum_{i=1}^{N_m} z_i\delta(r - r_i) \qquad \text{in } \Omega \subset \mathbb{R}^3, \tag{1}$$

$$u(r) = g(r) \text{ on the boundary } \partial\Omega. \tag{2}$$

The constants e_c, k_B, and T in (1) represent the elementary unit of charge, Boltzmann's constant, and the absolute temperature, respectively. The piecewise constant dielectric is $\epsilon(r)$ and the inverse Debye–Hückel length $\kappa^2(r)$ is given by $\kappa^2 = 2Ie_c^2/\epsilon kT$, where I is the solvent ionic strength. The charge distribution of the molecule is described by the N_m point charges $q_i = z_ie_c$ at positions r_i, yielding the

Received August 16, 1993; revision accepted October 8, 1993.
Address reprint requests to Shankar Subramaniam, Beckman Institute, University of Illinois at Urbana-Champaign, 405 N. Mathews Avenue, Urbana, Illinois 61801.

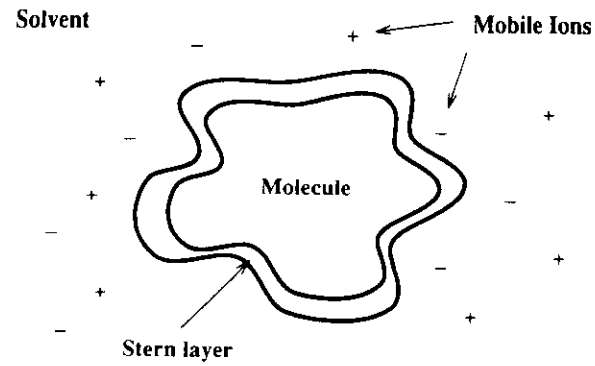

Fig. 1. The Debye–Hückel model for macromolecules in ionic solution.

delta functions in (1). The domain Ω is a rectangular box that encloses the protein and the function $g(r)$ on $\partial\Omega$, the surface of the box, is chosen to reflect the asymptotic behavior of the potential at large distances from the molecule. In practical investigations involving protein electrostatics, it is frequently assumed that u is small compared to unity and therefore the $\sinh(u)$ term can be replaced by u, the first term in its power series expansion. This simplification results in the widely used *linearized Poisson–Boltzmann equation* (LPBE).

Although it can be shown using standard techniques that both the NPBE and LPBE always have unique solutions,[9] closed form expressions for such solutions are quite complex, even in the few simple situations for which they exist.[10] A very early analytical approximation approach to the NPBE for a spherical molecule appears in Brenner and Roberts,[11] whereas analytical approaches to closely related equations can be found in Fujita[12] and Ting et al.[13] Due to advances in computational algorithms and hardware in recent years, several investigations into the efficiency and accuracy of numerical methods for the linearized Poisson–Boltzmann equation (LPBE) have appeared.[14–18] In such approaches, the LPBE is recast as a finite-difference equation on a cubic grid,[19] and iterative matrix techniques are employed to handle the resulting system of algebraic equations. However, difficulties are encountered when standard linear methods are generalized to nonlinear problems, because they are not globally convergent,[20] meaning they are not guaranteed to arrive at the true solution from an arbitrary initial guess. Hence, the NPBE is only now beginning to find use as a tool for studying electrostatic properties, and various numerical methods are being proposed and investigated.[17,21–26] Until now, though, there have been no detailed studies or comparisons of the efficiency and robustness of the proposed numerical methods.

In spite of the increased complexity of the NPBE, there are cases where the linear approximation is inadequate, and the full equation must be solved. As stated above, the LPBE assumes that u is much less than one. However, if we look at the analytic solution at the surface of a spherical molecule, we find that $u = 7.1Q/a(1 + \kappa a)$ at room temperature, where Q is the molecular charge in units of e_c, and a is the radius in Å. It is clear that u can be quite large for reasonable values of Q and a, particularly at lower ionic strengths. The solutions of the NPBE and LPBE also have entirely different scaling properties with respect to molecular charge. By investigating simple systems, we have found that the magnitude of u grows only logarithmically with the magnitude of the charge in the NPBE, whereas it grows linearly for the LPBE. Thus the NPBE tends to suppress effects arising from high concentrations of electric charge. This can be especially important near the active sites of certain enzymes and, indeed, it has been found that reduced reaction rates are obtained for diffusion-controlled catalysis by superoxide dismutase[21] when the NPBE is used instead of the LPBE.

These considerations make the development of an efficient method for solving the full NPBE a worthwhile goal and various methods have been proposed to circumvent the problems associated with the exponential nonlinearity in (1). One approach, which has been applied in a variety of systems, has been to represent the hyperbolic sine by its first three Taylor series terms, resulting in a fifth-degree polynomial.[17,22,25] Although this represents an improvement over the LPBE, it still suffers from the same deficiencies and again gives the improper scaling behavior with charge. Another method involves building up a solution to the full NPBE by solving a sequence of auxiliary equations in which $\sinh u$ is represented by more and more terms of its power series.[21] This has been used in an investigation of the effects of nonlinearities in the diffusion-controlled reaction between O_2^- and superoxide dismutase. This technique is extremely time-consuming versus the linear solution and for highly nonlinear problems, an increasing amount of effort is required to obtain a fully converged solution. In an alternate procedure, a variational formulation of the NPBE is used along with optimization techniques to find the minimum of an associated energy integral, which corresponds to the solution of the NPBE.[23] This approach, which is a special case of the Fletcher–Reeves algorithm,[27] has so far been applied only to problems with spherical symmetry. More recently, an application of multigrid techniques to the NPBE has been pursued by Oberoi and Allewell[26] in an investigation of lysozyme titration curves.

We have previously presented a multigrid, or multilevel, method for numerical solution of the LPBE[28] and showed that for two test problems, the multilevel method was superior to relaxation and Krylov subspace methods that had previously been dis-

cussed in the literature,[14] as well as to some improved versions of the existing methods that had not been previously applied to the LPBE. It was demonstrated that the method becomes more advantageous as the problem size grows, which will become increasingly important as more accurate numerical solutions, and hence larger discrete problem sizes, are required. In this paper, we present a hybrid method in which a robust nonlinear Newton iteration scheme is combined with a rapid linear multilevel algorithm in order to obtain a solution of the nonlinear system of equations arising from discretization of the full NPBE. The form of the Newton algorithm that is employed is globally convergent and yields superlinear convergence as the trial solution becomes sufficiently close to the true solution. We show that the hybrid algorithm is superior to other methods for the NPBE, including a more standard nonlinear multigrid implementation and as in the linear multilevel case, this superiority grows with the problem size. In fact, it is observed that this nonlinear method is so efficient that it solves the full nonlinear problem in less time than some of the best existing linear methods take to solve only the linearized problem. In addition, it is the only method robust enough to solve highly nonlinear cases.

The remainder of the paper is structured as follows. We first review multilevel methods for solving linear elliptic equations and describe inexact Newton and damped Newton methods for nonlinear equations. Our algorithm, which is employed in subsequent computations, is based on a combination of these techniques. The NPBE is then solved for a variety of proteins including crambin, BPTI, the Fv fragment of HyHEL-5, superoxide dismutase, the rhinovirus coat protein, and tryptophan synthase. The present approach is shown to give far superior performance compared with other nonlinear methods for a weakly nonlinear sample problem. The superlinear convergence of the algorithm is demonstrated. It is also shown that the time required for a solution is proportional to the number of unknowns and that this time is less than that necessary for a conjugate gradient solution of the corresponding linearized equation. The scaling of the potential with respect to charge is investigated for a spherical molecule with the LPBE, NPBE, and the fifth-order truncation of the NPBE. The effect of ionic strength on the validity of the various approximations is discussed. One of the most effective tests of models for protein electrostatics is provided by Brownian dynamics simulations of diffusion-controlled reactions. The effect of nonlinearities in these studies is explored in this paper, where simulations are run for both superoxide dismutase catalysis and a model antibody–antigen system. Finally, the power of the multilevel approach for solving large systems is demonstrated by an application of the method to the tryptophan synthase dimer, one of the largest proteins for which a crystal structure exists. Contour maps for the electrostatic potential from both the LPBE and the NPBE are shown. We conclude with a brief summary of our results.

MATERIALS AND METHODS

Numerical Methods for Nonlinear Elliptic Equations

In an earlier paper,[28] multilevel methods were designed and applied to the LPBE with very good results; the methods were shown to be superior to highly competitive techniques such as preconditioned conjugate gradient algorithms and successive overrelaxation. Multigrid methods have additionally been shown to be extremely effective for a wide range of problems and are provably of *optimal order complexity* for certain classes of problems,[29–31] in that the work required to solve for N unknowns is $O(N)$. This means that the advantages of multigrid over other methods will increase with the size of the problem, since no other methods are known to share this optimal complexity property. Here we wish to exploit some of these previously developed techniques[28] to the more numerically challenging NPBE. Although nonlinear generalizations of multilevel algorithms are available in the literature,[32–37] we often encountered difficulties in obtaining convergence when these methods were applied to the NPBE for various proteins. We thus adopted a different approach in which the advantages of the linear multigrid algorithm are combined with more robust nonlinear methods.

The nonlinear solver to be used below employs a variant of the multidimensional Newton's method. At each Newton iteration, a solution to a system of linear equations is required. This will be handled by linear multigrid techniques, which enables us to retain the speed and $O(N)$ convergence associated with the method. The additional use of the nonlinear Newton solver, however, enables us to include features which increase both the efficiency and robustness of the algorithm. One such improvement, referred as an inexact Newton method, solves the linear system only approximately during the first few iterations. Another enhancement involves the modification of the iterative equations by judiciously chosen damping parameters. The technique to be discussed below combines all of the above ideas and will be referred to as the multigrid damped inexact Newton (MUGDIN) algorithm. The method yields solutions of the NPBE faster than all previously used techniques, except multigrid, for the LPBE and, more importantly, has provided converged results for all of the cases that we have so far examined.

Linear Multigrid Methods

Multigrid methods are efficient numerical algorithms for solving the algebraic equations which

arise from discretizations of partial differential equations. We refer to our study of the LPBE[28] or to the standard references[31,38] for discussions of the basic correction scheme algorithm for linear elliptic equations, as well as examples of prolongation, restriction, and smoothing operators, and the distinctions between the V-Cycle, W-Cycle, and the FMG algorithms. An elementary introduction to the subject is given by Briggs.[39]

In a standard single-grid algorithm, an iterative scheme is devised to solve the matrix equation which arises from a discrete (finite difference, finite volume, or finite element) approximation. That is, an initial guess is made for the solution and the error to this guess is reduced through the repeated application of an equation based on the original matrix. Although this procedure is quite efficient at smoothing out the error, i.e., eliminating the portions of the error which have length scales on the order of the grid spacing, it is much less successful in handling the lower frequency components of the error. This is because the discrete approximation, for local operators allows for efficient communication only between neighboring nodes. Multilevel algorithms circumvent this problem by simultaneously discretizing the partial differential equation on grids of several resolutions. In some earlier studies of the LPBE, a multiple-grid approach was employed to obtain an improved initial guess prior to iteration.[40] In the algorithm presented here, the various grids are also used to accelerate the convergence of the iterative process.

We outline the multilevel method for a linear elliptic equation $Lu = f$ as this algorithm will be employed in our solution to the full nonlinear equation. We define a sequence of discrete problems, $L_{h_i} u_{h_i} = f_{h_i}$, by some discretization method, which we number $h_1, \ldots, h_k$ with $h = h_k$ denoting the finest grid and $H = h_{k-1}$ denoting the next finest grid. We can furthermore define linear *restriction* and *prolongation* operators R and P, respectively, which map grid function from the fine grid to the coarse grid, and from the coarse grid to the fine, respectively. For certain discretizations, such as the finite element method, it is automatically the case that

$$L_H = RL_hP \tag{3}$$

where R and P are chosen appropriately. In the finite-difference computations presented here, the various L_{h_i} are constructed by directly discretizing the partial differential equation on each grid. This method is suitable provided that the discontinuity in the dielectric constant is not too large[9] as is the case for protein electrostatics. Alternatively, the matrix L_H can be obtained algebraically from L_h by directly using (3). This procedure is computationally more intensive, but may be possibly advantageous from a theoretical standpoint.[31]

The linear multigrid method[31] or correction scheme[38] for solution of the discretized equations

$$L_h u_h = f_h \tag{4}$$

is based on the *error equation;* at iteration j the method solves for the *error* $e_h^j = u_h - u_h^j$ from

$$L_h e_h^j = L_h(u_h - u_h^j) =$$
$$L_h u_h - L_h u_h^j = f_h - L_h u_h^j = r_h^j \tag{5}$$

where r_h^j is the *residual.* If the error is smooth compared to the scale of the grid spacing, it can be equally well represented on a coarser grid. Therefore, a *smoothing* method, such as Gauss–Seidel or Jacobi iteration,[41] which efficiently damps out the high-frequency components of the error is performed on the fine grid. In such an approach, L_h is split into $L_h = M_h - N_h$. If M_h is taken to be the diagonal part of L_h, this procedure yields the Jacobi method, while if M_h is the lower triangular part of L_h, Gauss–Seidel iteration is obtained. The solution to (4) obeys the equation

$$u_h = M_h^{-1} N_h u_h + M_h^{-1} f_h \tag{6}$$

which is used to generate the iterative scheme

$$u_h^{j+1} = S_h u_h^j + T_h f_h \tag{7}$$

where $S_h = M_h^{-1} N_h$ *and* $T_h = M_h^{-1}$. After the above smoothing method, which is chosen to be Gauss–Seidel iteration for the present algorithm, is performed on the fine grid, the error equation is then solved on a coarse grid. This result is transferred back to the fine grid through the use of the prolongation operator P. Finally, the smoothing method can again be applied to the corrected solution.

A simple two-grid version of this iteration can be formulated as

$$\left\{\begin{array}{ll}
\text{Let } u_h^0 \text{ be an initial approximation.} & \\
\text{Do } j = 0,1,2,\ldots \text{ until convergence:} & \\
\quad 1.\ \text{Presmooth:} & \bar{u}_h = S_h u_h^j + T_h f_h \\
\quad 2.\ \text{Restrict residual:} & r_H = R(f_h - L_h \bar{u}_h) \\
\quad 3.\ \text{Solve for correction:} & e_H = L_H^{-1} r_H \\
\quad 4.\ \text{Prolongate and correct:} & \bar{\bar{u}}_h = \bar{u}_h + Pe_H \\
\quad 5.\ \text{Postsmooth:} & u_h^{j+1} = S_h \bar{\bar{u}}_h + T_h f_h \\
\text{End Do.} &
\end{array}\right\} \tag{8}$$

It can be seen that step 3 requires the solution of a linear equation on the coarser grid. Thus, the error to this equation can be corrected on the next coarsest grid in the same manner as above. One can continue to recursively descend to the coarsest grid h_1 where, if the initial grid size is properly specified, the linear equation can be effectively solved using direct matrix inversion. Some standard approaches for cycling between fine and coarse grids are depicted graphically in Figure 2; these algorithms are described in more detail elsewhere.[28,31]

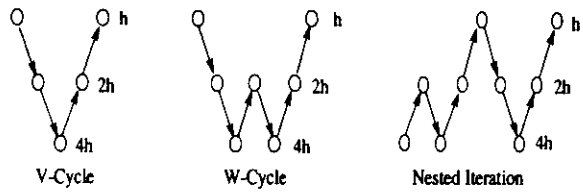

Fig. 2. Nested sequence of meshes in three common multigrid algorithms. The leftmost diagram shows the V-cycle which involves correcting with the coarse grid once at each iteration. The W-cycle entails two coarse grid corrections per level at each iteration. The final diagram illustrates a boot-strapping technique which provides improved initial approximations.

Newton-Multigrid Iteration

We first remark that the question of uniqueness of solution is a nontrivial matter, especially in the nonlinear case. For example the nonlinear Bratu problem,[42] which is quite similar to the NPBE, possesses nonunique solutions in certain cases. It has been shown,[9] however, that both the NPBE and the nonlinear algebraic equations arising from a standard finite volume discretization are uniquely solvable for any molecule defining the right-hand side function f_h.

The method adopted for solving the discretized approximation to the nonlinear problem involves a generalization of Newton's method for finding the roots of a one-dimensional function.[20] In this simpler case, the function $a(x)$ is approximated by the first two terms of its Taylor series leading to

$$a(x) \approx a(x^0) + (x - x^0)a'(x^0) = 0 \qquad (9)$$

where x^0 is an initial guess to the solution. This yields the iteration

$$x^{j+1} = x^j - a(x^j)/a'(x^j). \qquad (10)$$

This equation has a simple geometrical interpretation; the updated guess x^{j+1} is where the tangent line of $a(x)$ at x^j intersects with the x-axis. There may, however, be instances when $a'(x^j)$ becomes very small, leading to divergence of the second term in the above equation. In practice, this implies that (10) is not guaranteed to converge from an arbitrary initial guess. Thus *damping parameters* ω_j are introduced such that

$$x^{j+1} = x^j - \omega_j a(x^j)/a'(x^j) \qquad (11)$$

in order to ensure convergence of the algorithm. Of course, the ω_j must go to one as x^j approaches the solution.

Now, let $N_h(u_h) = f_h$ denote the system of n nonlinear algebraic equations corresponding to a discretization of the second-order nonlinear elliptic partial differential equation $N(u) = f$, and denote the derivative, or Jacobian matrix, of N_h at u as $DN_h(u)$. Since we wish to solve the equation $N_h(u_h) - f_h = 0$, the appropriate analog to the above procedure is as follows:

$$\left\{\begin{array}{l} \text{Let } u_h^0 \text{ be an initial approximation.} \\ \text{Do } j = 0,1,2,\ldots \text{ until convergence.} \\ \quad 1.\ \text{Solve linear system for} \\ \qquad \text{correction:} \quad DN_h(u_h^j)\,\delta_h^j = f_h - N_h(u_h^j) \\ \quad 2.\ \text{Correct the solution:} \quad u_h^{j+1} = u_h^j + \omega_j \delta_h^j \\ \text{End Do.} \end{array}\right\} \qquad (12)$$

The vector δ_h^j defines a direction in multidimensional space along which to find a correction to the solution and the damping parameters ω_j increase the robustness of the algorithm. In fact, it can be shown[20] that the Newton direction δ_h^j is always a *descent direction*, in the sense that for each Newton direction δ_h^j, there exists some steplength ω_j such that

$$\|N_h(u_h + \omega_j \delta_h^j) - f_h\| \leq \|N_h(u_h) - f_h\|. \qquad (13)$$

Therefore, we perform one-dimensional line searches along the Newton direction δ_h^j until (13) is satisfied. In this sense, the method is globally convergent.

Step 1 of iteration (12), which requires the solution of a linear system of equations, can be efficiently implemented with the linear multigrid method discussed above. An advantage to the above method is that if the approximation u_h^j is close enough to the solution u_h, then the Newton's method will converge superlinearly or even quadratically, although the convergence rate of the entire iteration will be dominated asymptotically by the linear convergence of the multigrid method.[31,43] Such a Newton-multigrid iteration has been used successfully for other applications.[43,44]

Another modification which increases the efficiency and robustness of the algorithm is motivated by the observation that, for the first few iterations when u_h^j is far from the true solution, it is hardly necessary to solve the linear system in Step 1 of (12) exactly; the only requirement is that the Newton direction be approximately correct. This is the reasoning behind the inexact Newton methods,[45–48] in which the system of linear equations is solved only within a very loose tolerance at first, with the tolerance being gradually tightened to the desired accuracy of solution as the iteration proceeds. With the appropriate tolerance criteria at each Newton iteration, it can be shown that this algorithm also convergences superlinearly.[47] An analysis of the interplay of the damping and inexact solutions of the Newton equations can yield criteria for both the damping parameters and the tolerances to which the linear equations are solved which guarantee a global superlinear convergence of the Newton iteration.[46]

The solutions of the nonlinear Poisson–Boltzmann equation to be presented here employ the Newton

iteration given in (12) with linear multigrid, designed specifically for the linearized Poisson–Boltzmann operator,[49] used as an inexact solver in Step 1 and the damping parameter in Step 2 chosen to provide global convergence properties. As noted above, this hybrid procedure is referred to here as the MUGDIN algorithm.

RESULTS

Performance of Algorithm

Calculations are performed below for a variety of proteins in order to test the present algorithm within the context of applications to biological systems. Since the MUGDIN method is based on a solution of the system of equations which results from the finite-difference approximation to the Poisson–Boltzmann equation, it can be incorporated into any program which employs such a formalism. We have implemented our code as a module within the UHBD program,[6] which sets up the problem for the multigrid solver.

The following details hold for each of the calculations described in this section. All of the atomic coordinates are taken from the Brookhaven Protein Data bank. The molecular volume is obtained by identifying radii from the OPLS force field[50] with each of the atoms. A residue-based model is used to define the charge distribution of the protein by assigning appropriate unit charges to the following atoms: CG of Asp, CD of Glu, NZ of Lys, and CZ of Arg. Where necessary, charges are also given to the N and C atoms of the N- and C-termini, respectively, and to CE1 of His. We note that the multigrid algorithm works just as well for more detailed atomic charge models, as will be shown in the next section. No Stern layer is used and this tends to emphasize the magnitude of nonlinear effects, since the ion density is nonzero up to the surface of the molecule where the potential tends to be strongest. The dielectric constant inside the molecule is assumed to be 2 and the dielectric constant of the solvent taken as 78. At the protein–solvent boundary, a smoothing procedure is employed in which the dielectric constant is assigned an intermediate value according to how close a grid point is to the interface.[6] All calculations are done at a temperature of 300 K and are deemed to be converged when the norm of the residual vector r_h divided by the norm of f_h becomes less than 10^{-8}. For the conjugate gradient methods, the convergence criterion is that the norm of $(u_h^{j+1} - u_h^j)$ be less than 10^{-8} times the norm of u_h^j. The timings are obtained by running the program in double precision on one vector processor of a Convex C240 for crambin and that of a Convex C3880 for all other cases.

The boundary condition $g(r)$ for both the LPBE and NPBE, as defined in (2), is obtained by summing the potentials of all of the charged atoms as if each atom is an independent Debye–Hückel sphere of radius 2 Å. This assumes the validity of a linear approximation on $\partial\Omega$. As long as the boundary is chosen sufficiently far away from the surface of the molecule, the magnitude of u will be small and this should be a good approximation. Ultimately, however, it will be best to choose the boundary conditions so as to properly reflect the nonlinear nature of the equation. One possible way to achieve this would be to construct look-up tables based on the solution of the NPBE for Debye–Hückel spheres of various charges and radii. The construction of $g(r)$ is potentially very time-consuming, particularly when charges are assigned to each atom, as it requires on the order of $l^2 N_m$ operations, where l is the number of nodes in each direction and N_m is the number of charges. In order to present a more clean comparison between various calculations, each CPU time reported on below is that which is required only to solve the appropriate finite-difference equation and does not include any of the set-up time associated with the problem.

Comparison With Other Methods

The exponentials that occur in the hyperbolic sine function of the NPBE are a source of great difficulty for nonlinear methods. For most of the cases discussed here, standard nonlinear solvers were unable to achieve converged solutions to the NPBE. We therefore show in Figure 3 a comparison of various methods using a small, mildly nonlinear problem. The electrostatic potential for the 46-residue protein crambin,[51] with a total of six charges and a net charge of zero, is solved for on a 31^3 grid, with 2 Å spacing at an ionic strength of 1 mM. Although the grid is quite small for the molecule being considered and the salt concentration is very low from an experimental standpoint, this example is indicative of the conditions that are necessary in order to obtain converged solutions to the NPBE for methods other than the one described here. We note that we have had better success with other methods when the fifth-order polynomial approximation to the nonlinearity is employed.

The MUGDIN algorithm yields by far the most rapid convergence and is considerably faster than a more straightforward generalization of the multigrid method similar to that used by Oberoi and Allewell.[26] Next after the multigrid-based methods are the nonlinear conjugate gradient method, followed by the nonlinear successive over-relaxation algorithm. Each of these is at least three times as fast as the nonlinear Gauss–Seidel solver which was employed in a previous study of the NPBE, as described earlier.[21]

We note that it is certainly possible to devise other schemes for handling the NPBE. For example, one might use the Newton's method described in the preceding section in conjunction with some other linear

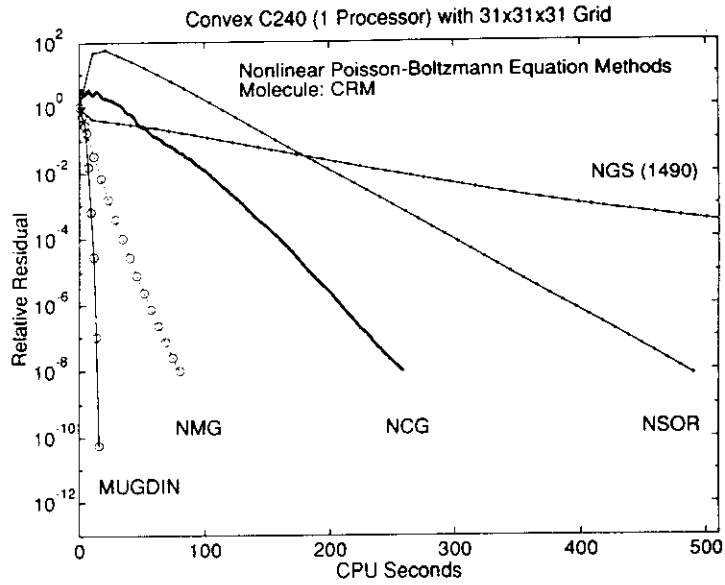

Fig. 3. Performance for various nonlinear solvers of the full Poisson–Boltzmann equation for the protein crambin at 1 mM ionic strength. The norm of the relative residual, which is a measure of the amount that the approximate solution differs from the true solution, is plotted as a function of iteration number and CPU time. The curve labeled MUGDIN is obtained using the algorithm described in the text. The other curves result from the application of straightforward nonlinear generalizations of standard linear solvers including multigrid (NMG), conjugate gradient (NCG), successive overrelaxation (NSOR), and Gauss–Seidel (NGS).

equation solver, such as a conjugate gradient method or the Gauss–Seidel iteration. However, given the advantages of the linear multigrid method for handling such systems, it is likely that such approaches will yield inferior performance against the MUGDIN solver. Interestingly, we have found that our algorithm runs faster with the full nonlinearity of the NPBE compared to its fifth-order polynomial approximation. This is due to the fact that the hyperbolic sine is a machine-level intrinsic function, while the polynomial is evaluated in higher level code. It does illustrate, though, the success of the present algorithm at handling an exponential nonlinearity.

Scaling and Convergence Properties

The remainder of the computations performed in this section are done at 5 mM ionic strength with a grid spacing of 1 Å. The proteins and grid sizes considered below are bovine pancreatic trypsin inhibitor (BPTI)[52] with 58 residues at a grid size of 63^3, the Fv fragment of the HyHEL-5 antibody[53] with 221 residues at 95^3, the superoxide dismutase (SOD) dimer[54,55] with 304 residues at 127^3, the rhinovirus coat protein monomer[56] with 804 residues at 159^3, and the tryptophan synthase dimer[57] with 1266 residues at 191^3. The properties of the above systems have been collected in Table I. The Fv fragment has zero total charge has no center of charge and in this instance, the center of the grid is chosen according to the requirement that the diagonal moments of the quadrupole tensor vanish with respect to this point.[58] In all other cases, the grid is centered at the molecular center of charge. When residues are absent from the crystallographic structures due to disorder, they are omitted from the calculation. These missing residues only occur at the N-terminal ends of some chains in the rhinovirus protein and at the end of a few helices and strands in tryptophan synthase.

In the previous section, we have discussed the superlinear convergence properties of the MUGDIN algorithm when the trial solution becomes sufficiently close to the true solution. This behavior is displayed in Table II for BPTI as well as the rhinovirus coat protein. In each case, the relative residual decreases dramatically during the last few iterations. Thus the inexact Newton's method becomes more advantageous the greater the accuracy demanded of the solution. In comparison, the norm of the residual as a function of iteration number for the multigrid solution of the corresponding LPBE shows linear convergence. An inspection of Figure 3 reveals that the straightforward nonlinear generalization of the multigrid algorithm also yields linear convergence. We have also solved the LPBE for these systems using the linearly convergent diagonally scaled conjugate gradient method which required 294 iterations for BPTI and 694 iterations for the rhinovirus protein, although each of these iterations is less expensive in terms of CPU time than a multigrid iteration.

As with the multigrid method, the MUGDIN approach is of optimal order, meaning that the work

TABLE I. Sample Proteins*

	Residues	Grid nodes	CPU time
Bovine pancreatic trypsin inhibitor	58	63 × 63 × 63	65
HyHEL-5 antibody (Fv fragment only)	221	95 × 95 × 95	235
Superoxide dismutase (homodimer)	304	127 × 127 × 127	634
Rhinovirus coat (monomer)	804	159 × 159 × 159	1220
Tryptophan synthase (homodimer)	1266	191 × 191 × 191	1690

*Sample proteins used in the present study. The first column gives the total number of residues, the second column shows the total number of grid nodes used for discretization on the finest grids, and the third column gives the CPU seconds required for a solution of the full nonlinear Poisson–Boltzmann equation at 5 mM ionic strength by the multigrid damped inexact Newton algorithm described herein.

TABLE II. Convergence Properties of Multilvel-Based Algorithms*

	Norm of relative residual			
	BPTI		Rhinovirus	
Iteration	LMG	MUGDIN	LMG	MUGDIN
0	1.00E+00	1.00E+00	1.00E+00	1.00E+00
1	1.01E−01	5.30E−01	2.80E−01	7.93E−01
2	6.88E−03	3.81E−02	3.65E−02	5.30E−01
3	1.13E−03	4.35E−03	5.58E−03	7.72E−02
4	1.78E−04	6.62E−04	1.19E−03	1.14E−02
5	5.03E−05	5.85E−05	4.28E−04	1.83E−03
6	1.72E−05	8.84E−07	9.74E−05	2.62E−04
7	2.85E−06	3.68E−10	1.78E−05	1.55E−05
8	6.68E−07		4.18E−06	1.19E−07
9	1.15E−07		8.40E−07	1.82E−11
10	1.74E−08		2.61E−07	
11	6.04E−09		7.83E−08	
12			1.75E−08	
13			4.49E−09	

*Norm of the relative residual versus iteration number for a multigrid solution (LMG) of the linearized Poisson–Boltzmann equation and a multigrid damped inexact Newton (MUGDIN) solution of the full nonlinear Poisson–Boltzmann equation. The two sample proteins for which results have been displayed are bovine pancreatic trypsin inhibitor and the rhinovirus coat protein. The LMG method displays linear convergence as a function of iteration number while the MUGDIN algorithm yields superlinear convergence during the last few iterations when the trial solution is sufficiently close to the true solution.

needed to solve for N unknowns is proportional to N. This desirable property is shown in Figure 4, where the CPU times required to solve the LPBE and NPBE with several methods for various proteins are plotted. It is seen that while the multigrid solution of the LPBE is faster than the MUGDIN method for the NPBE, the latter is still much more efficient than the diagonally scaled conjugate gradient method for the LPBE by as much as a factor of three. Since the nonlinear solver displays optimal order behavior, the advantages are greater the larger the problem size. Thus, not only does the present algorithm provide for a full consideration of nonlinear effects implied by the Poisson–Boltzmann equation, it also allows for the treatment of large systems which have heretofore been computationally intractable.

Scaling With Respect to Charge

From a simple inspection of the NPBE, it can be inferred that the electrostatic potential increases only logarithmically with charge as opposed to linearly with the LPBE. As noted previously, this feature of the NPBE significantly reduces the biological consequences of highly charged molecules. To investigate this property, we have performed calculations for spherical molecules at various charges and ion concentrations. Shown in Figure 5 is the potential 2 Å away from the surface of a sphere of 15 Å radius as a function of charge at two ionic strengths. A numerical solution of the full NPBE is given as well as the analytical solution of the LPBE. For comparison, the potential has also been computed using a fifth-order polynomial approximation for the hyperbolic sine function. For the nonlinear equations, the imposed boundary condition is that the solution approach the LPBE potential at the outer faces of the grid. A very large grid size, 191 nodes on a side, was employed to minimize the effects of this approximation, with 2 Å spacing at 30 mM ionic strength and 1 Å resolution for 150 mM.

The logarithmic scaling of the NPBE can be

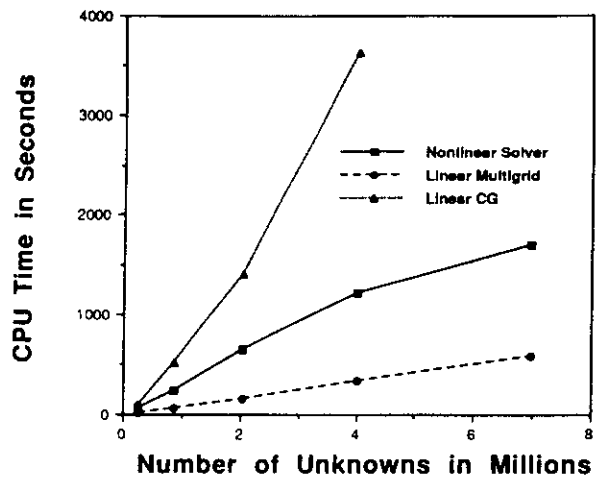

Fig. 4. CPU time as a function of the number of unknowns for solution of the linear and nonlinear Poisson–Boltzmann equations. The solid line gives the MUGDIN solution time, while the other curves represent the time required for the multigrid and diagonally scaled conjugate gradient methods to solve the linearized Poisson–Boltzmann equation. The sample proteins are listed in Table I and all calculations are done at 5 mM.

clearly observed in the graphs. It is also seen that the fifth-order result is often a very reasonable approximation, particularly for lower charge and higher ionic strengths. There are regimes, however, where this representation breaks down as the potential asymptotically scales as the one-fifth power of the charge rather than the logarithm. Although in some cases, the charge of the sphere is much larger than what would be expected for proteins, the study is meant to be merely illustrative and we have indeed found the same qualitative behavior in biological systems, as has been explicitly discussed for the case of SOD.[59]

Electrostatic Steering

An important application of the Poisson–Boltzmann equation is to Brownian dynamics simulations of diffusion-controlled biomolecular reactions.[60] In some systems, it has been found that the rates for such reactions are enhanced through long-range forces, as the two molecules can mutually guide each other into a configuration favorable for reaction. The interactions which are responsible for the steering are electrostatic in nature and can be determined through solution of a Poisson–Boltzmann equation. The NPBE is particularly relevant in this regard as appreciable steering occurs primarily when u approaches unity, which is precisely the regime where the LPBE breaks down.

A comparative study by Allison, Sines, and Wierzbicki[21] has been carried out for simulations of SOD catalysis with both the LPBE and NPBE. It was found that significantly reduced reaction rates can occur when the NPBE is used, with the amount of reduction dependent on the ionic strength. These results can be understood in terms of the contour maps that we have calculated for SOD,[59] where the potential in the vicinity of the active sites can be seen to be much larger with the LPBE than for the NPBE. This is a specific example of the increased damping of the field due to the protein that occurs in the NPBE, since the mobile ions are allowed to react to external fields beyond a linear response approximation. This is of course related to the different scaling behaviors with respect to charge of the two equations.

The Brownian dynamics simulations reported on in this section are carried out with the UHBD code.[6] In these computations, one molecule is held fixed and rigid at the center of two concentric spheres while the other (in both cases below, a charged sphere) undergoes diffusional motion under the influence of the field of the first. The second molecule is initially placed on the inner sphere and its motion is propagated in discrete time steps Δt according to the equation[61]

$$\Delta \mathbf{r} = \frac{D}{k_B T} \mathbf{F} \Delta t + \mathbf{R} \tag{14}$$

where $\Delta \mathbf{r}$ is the change in position, D is the relative diffusion constant, and $\mathbf{R}$ is a random vector satisfying certain statistical constraints. The quantity $\mathbf{F}$ gives the electrostatic force obtained from the Poisson–Boltzmann solution for the first molecule as $\mathbf{F} = -\nabla\Phi$. The motion is continued until either a predetermined reaction condition is met or the outer sphere is reached. The reaction rate k, which is determined statistically from a large sample of trajectories, can be related to the probability β that such a trajectory will yield a reaction by the equation[62]

$$k = \frac{k_s(b)\beta}{1 - (1 - \beta)k_s(b)/k_s(q)} \tag{15}$$

where b and q are the radii of the inner and outer spheres, respectively, and $k_s(a)$ is the analytical result for the reaction rate for diffusion to a sphere of radius a in a spherically symmetric potential $U(r)$ which obeys the expression

$$k_s(a) = 4\pi D \left[\int_a^\infty \frac{\exp[U(r)/kT]}{r^2} dr \right]^{-1}. \tag{16}$$

We note that in order to be consistent with the use of the NPBE, one should employ the nonlinear solution in computing the above integral. For the antibody-antigen system below, the antibody is uncharged and thus $U(r) = 0$ in (16). For SOD, $U(r)$ is sufficiently small in the range of integration that essentially the same results are obtained whether the linear or nonlinear expression for $U(r)$ is used. Hence, all of the differences reported below arise in the

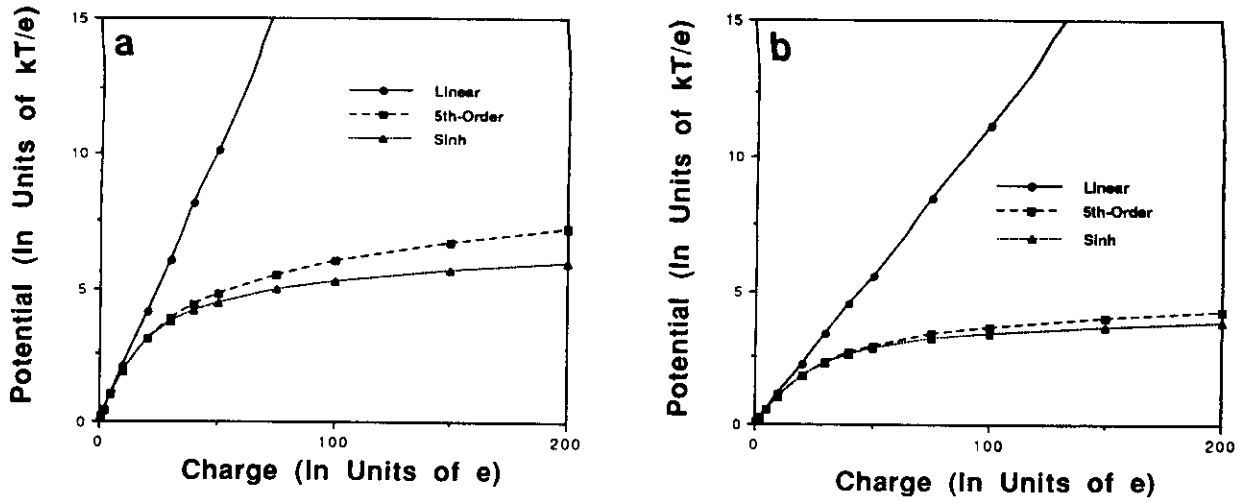

Fig. 5. The electrostatic potential at a distance of 2 Å away from the surface of a 15 Å spherical molecule at (a) 30 mM and (b) 150 mM ionic strength. The graphs compare the solutions of linearized, fifth-order, and full nonlinear Poisson–Boltzmann equations.

reaction probability β as obtained from the Brownian trajectories.

Antibody–Antigen System

Both experimental and theoretical evidence suggests that the rate for antibody–antigen association is limited by diffusion.[63,64] A detailed study of electrostatic steering in such a system has been undertaken through the use of Brownian dynamics.[58] The calculations were based on the X-ray crystal structure for the monoclonal antibody HyHEL-5 bound to hen-egg lysozyme.[53] The lysozyme carries a large net positive charge and the complex is stabilized by three salt bridges involving two charged residues from each of the proteins. Experimentally, it has been found that mutations of these important residues have a drastic effect on antibody–antigen binding.[65,66] Here some of the same simulations are repeated with the exception that the NPBE is used in place of the LPBE. The Fv fragment of the antibody plays the role of the fixed molecule in the above description while the lysozyme is approximated as a positively charged sphere. The NPBE for the Fv fragment is solved on a 95^3 grid exactly as described in the preceding section, except that the ionic strength is varied from 5 to 350 mM. In all other aspects, the calculations are performed as described previously.[58]

The simulations are run for the wild-type Fv fragment at several ionic strengths and with three different lysozyme charges. The ratios of the reaction rates for the NPBE solution to the LPBE solution are presented in Table III. As has been found in the SOD simulations, the use of the NPBE has resulted in a decrease of the reaction rate in all cases. Again this is presumably due to the increased electrostatic screening by the ions which is reflected by the nonlinear terms. The ratios vary in an irregular fashion with both salt concentration and charge and the reaction rate may be suppressed by as a much as an order of magnitude. The difference between the linear and nonlinear cases also appears to be getting smaller at lower lysozyme charge and higher ionic strength where electrostatic steering is less important. It is clear that use of the NPBE may affect the ionic strength dependence of the reaction rates calculated through Brownian dynamics. Moreover, the unpredictable manner in which the reaction probability is altered as a function of charge provides indications that the LPBE may be unreliable for computing *relative* reaction rates between various mutants of a system.

Superoxide Dismutase

There is an extensive history of Brownian dynamics simulations for SOD catalysis as it has been a prototype for the study of electrostatic steering in biomolecular reactions. Early researchers employed simple charge distributions[67] to simulate the field of superoxide dismutase. More sophisticated atomic charge models,[68–71] along with the LPBE, have been used to determine the effects of point mutations on the reaction rate.[72,73] Getzoff et al.[74] have performed computations in which reaction rates for wild-type human SOD catalysis are compared with various mutants of the protein. Although most of the calculated relative rates are in reasonable agreement with experiment, there are some quantitative differences particularly concerning one of the double mutants, which has been attributed to structural changes in the enzyme. As noted above, Allison et al.[21] have found that the use of the NPBE can have

TABLE III. Supression of Reaction Rates in Brownian Dynamics Simulations*

Lysozyme charge ionic strength in mM	(Nonlinear Rate/linear rate) 5e	3e	1e
5	0.62 ± 0.02	0.34 ± 0.04	0.45 ± 0.12
25	0.34 ± 0.04	0.19 ± 0.08	0.47 ± 0.13
75	0.16 ± 0.07	0.24 ± 0.10	0.59 ± 0.15
150	0.22 ± 0.09	0.45 ± 0.12	0.66 ± 0.16
350	0.56 ± 0.12	0.67 ± 0.17	0.69 ± 0.16

*Ratio of reaction rates for a model antibody–antigen system using the linear and nonlinear Poisson–Boltzmann equation to determine the extent of electrostatic steering. The ratio gives the reaction rate obtained with the nonlinear equation over the reaction rate implied by the linear equation. The estimated errors are statistical.

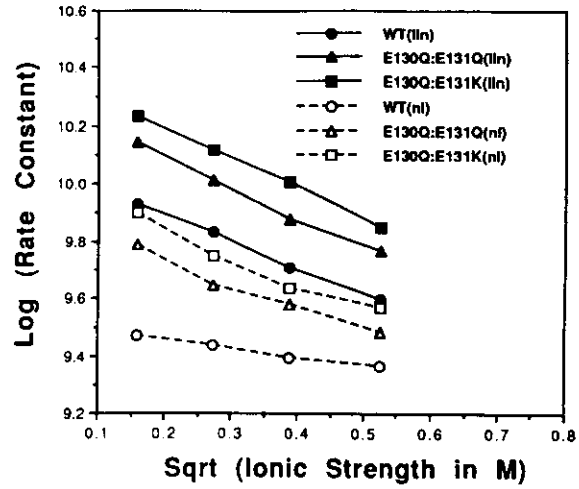

Fig. 6. Rate constants as a function of ionic concentration obtained from Brownian dynamics simulations of catalysis of superoxide by wild-type bovine superoxide dismutase and two mutants. The solid curves result from using the linearized Poisson–Boltzmann equation to determine the electrostatic steering, while the dashed curves give the rate constants when the full nonlinear equation is used.

a considerable effect in the SOD system. We have therefore performed our own simulations with the NPBE in order to reexamine the results of Getzoff et al.[74]

Because the atomic coordinates for human SOD are not yet generally available, the present investigation is performed with bovine SOD rather than human SOD. Otherwise, we have attempted to keep as close to the above calculation as possible. Thus we have added hydrogens to the structure and employed an all-atom charge model based on the OPLS force field. The reduced SOD form is considered in which the copper ions are given a charge of $+1e$ rather than $+2e$, with the extra charge being shifted to the His-61 residues. From the simulations of Sines et al.[72] and our own studies, it has been found that this slight change has a negligible effect on the reaction rate. The boundary condition on $\partial\Omega$ is enforced by assuming that $g(r)$ is generated by a single Debye–Hückel sphere with the total enzyme charge and a radius of 30 Å. The parameters associated with the diffusional trajectories are kept identical to those of Getzoff et al.,[74] who also utilized the UHBD program except that in the present case only 10,000 trajectories are run for each mutant.

We have run simulations for the wild-type bovine SOD and the two double mutants analogous to those of Getzoff et al.[74] Each double mutant involves the modification of two consecutive Glu residues near the active site and with the bovine protein these are given by A: (Glu-130→Gln,Glu-131→Gln) and B: (Glu-130→Gln,Glu-131→Lys). Reaction rates for simulations with both the LPBE and NPBE are presented in Figure 6. The relative rates and ionic strength dependence for the LPBE are very similar to those obtained for human SOD. One feature of the NPBE simulations is that the plots of the logarithm of the rate versus $\sqrt{I}$ are less linear for the NPBE simulations. As in the previous system, the NPBE rates are again lower, but the relative rates are qualitatively unchanged, whereas experiment indicates that the reaction rates for the analogous mutation to mutant B are less than those for the analog to mutant A. Given the similarity between human and bovine SOD, it is likely that this conclusion will hold for both cases. Thus it appears that the use of the NPBE does not resolve the discrepancy between theory and experiment in this instance. It has been suggested that the difference lies in structural changes in the enzyme[74] and such questions are more appropriately addressed within the framework of molecular dynamics.[75] We finally note that as the total electrostatic potential of the molecule decreases, the differences between the LPBE and NPBE calculations will become smaller, although the use of the NPBE is always to be preferred for Brownian dynamics simulations since it represents a more physically realistic model.

Tryptophan Synthase

As a final application of the MUGDIN algorithm, we undertake an investigation of the tryptophan synthase homodimer, a protein roughly 150 Å in length, which contains 1266 residues that have been resolved to 2.5 Å through X-ray crystallography.[57] Each monomer of the complex consists of two subunits, α and β, which catalyze a two-step reaction; the α-subunit reacts with an indole 3-glycerol phosphate molecule to produce indole which is then apparently channeled through an internal tunnel to the β-subunit to react with a serine in order to form the final product, tryptophan.[76] The subunits of the molecule are arranged in a roughly linear fashion as αββα, which can be seen in Figure 7.

The calculation is done on a 191^3 grid with 1 Å

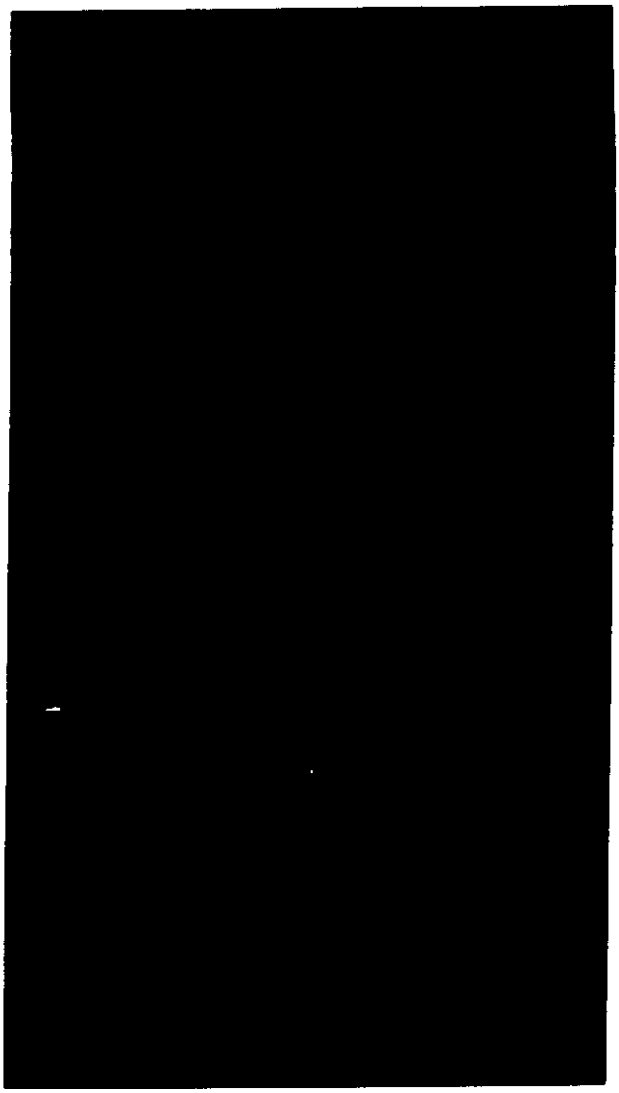

Fig. 7. Depiction of the tryptophan synthase dimer. The two identical β-subunits are flanked by the α-subunits. Each chain is shown in a different color.

spacing and all other aspects of the calculation are as outlined previously with exception that a Stern layer of 2 Å thickness is now included. As alluded to earlier, this modification tends to suppress effects arising from the nonlinearity. The His residues near the active sites of the β-subunits, B86 and B115, are assumed to be positively charged making the total charge of the system $-24e$. We note that the size of problem could possibly be reduced through the use of rectangular grids, or perhaps through focusing techniques. However, because it is wished to demonstrate the MUGDIN method for a large problem and since the calculation requires only 5 CPU minutes for the LPBE and 30 CPU minutes for the NPBE, we have followed the above formulation.

Color contour maps of the electrostatic potentials in a plane near the β active sites are shown in Figure 8, with calculations for both the LPBE and NPBE performed at 5 and 150 mM ionic strength. The excluded volume of the protein together with the Stern layer is rendered in white and the molecule has the same orientation as in Figure 7. The distinctions between the LPBE and NPBE are larger at 5 mM, but still persist at 150 mM. It is apparent that these differences are greater when the magnitude of the potential is larger, although changes in the contour lines where u is less than one can also be discerned. As expected the magnitude of the potential is always smaller for the NPBE, again due to the increased efficiency of electrostatic screening.

CONCLUSIONS

We have herein described a practical method for numerically solving the discretized version of the three-dimensional full nonlinear Poisson–Boltzmann equation. The technique combines a multilevel approach with an inexact damped Newton's method for solving nonlinear systems of equations. The algorithm scales linearly with the number of unknowns and converges superlinearly to the solution as the iteration proceeds. Our results indicate that the present algorithm is extremely robust in providing converged solutions to the NPBE in a wide range of ionic strengths for a variety of proteins. Furthermore, the algorithm yields a solution to the NPBE more rapidly than do the commonly used single-grid algorithms for the corresponding linearized equation. We are also able to test the validity of low-order polynomial representations of the nonlinearity, although use of the present method appears to make such approximations unnecessary.

The above properties have been verified for a number of proteins using grid sizes of up to 191^3 nodes, with the advantages becoming especially apparent for the largest systems. The application of the nonlinear solver to tryptophan synthase shows that it is possible to consider large molecules which otherwise might have been thought to be intractable. In attempting to compare our method with straightforward nonlinear generalizations of various linear equation solvers, it was found that the latter yielded converged solutions only for very small problems at extremely low ionic strength, due to the exponential terms that occur in the equation. We also encountered some of the same difficulties with the straightforward nonlinear multigrid technique. Thus, as of now, the present algorithm offers the most efficient and robust method for solving the full nonlinear Poisson–Boltzmann equation.

Although we have confined our investigations to monovalent electrolytes, the Poisson–Boltzmann equation, with suitable modifications, can be employed to describe polyvalent and mixed electrolytes. For these cases, the nonlinearity will be more severe than in Eq. (1) and hence the robustness of

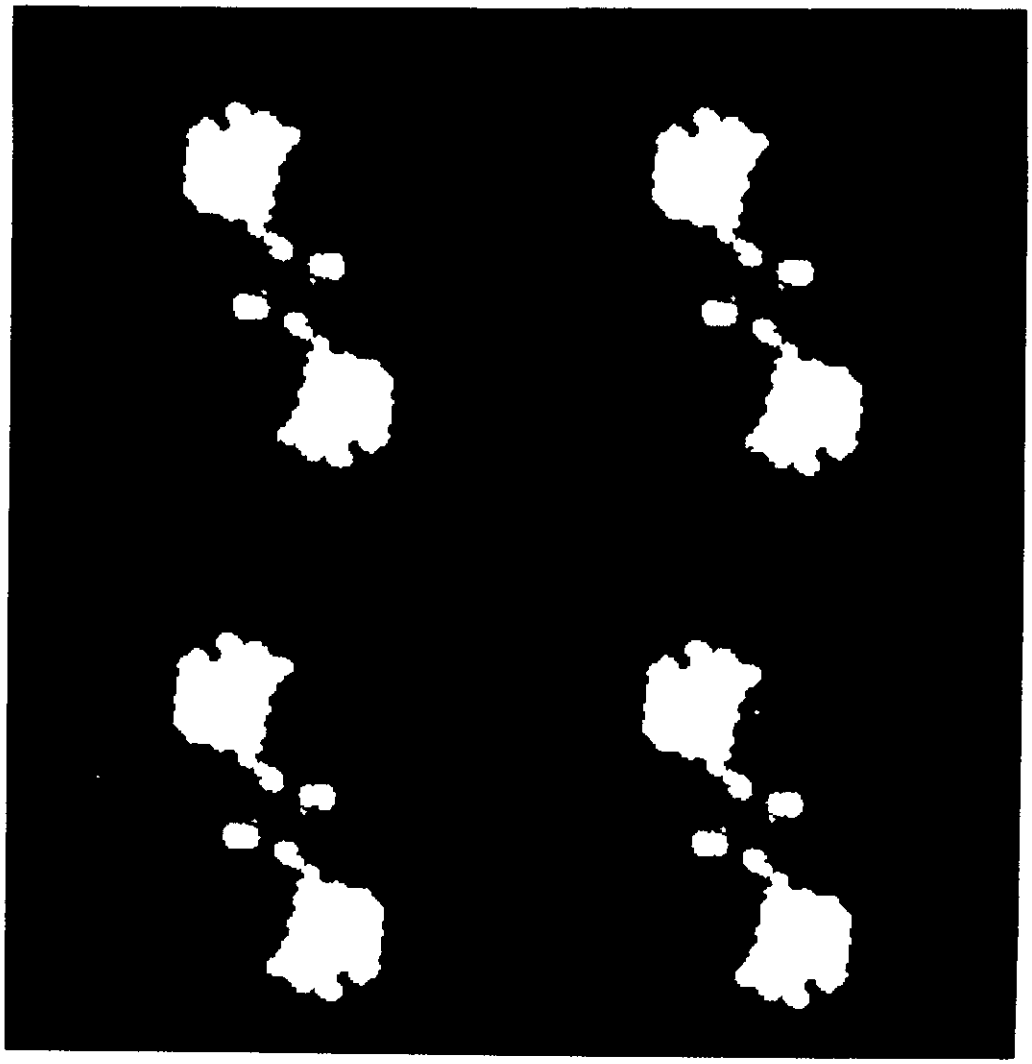

Fig. 8. Color contour maps of the electrostatic potential in a two-dimensional slice through the tryptophan synthase dimer. The top two diagrams represent solutions at 5 mM obtained from the linearized (**left**) and nonlinear (**right**) Poisson–Boltzmann equations. The bottom two pictures show maps for 150 mM, with the left and right again respectively representing linear and nonlinear solutions. The molecule is in the same orientation as in Figure 7. The excluded volume is given in white. The red portion is where the potential is larger than $2kT$, the green area is where it is between kT and $2kT$, and the border of the blue and gray areas is the $kT/2$ contour line.

the solver will take on increased importance. It should be noted, though, that such a continuum model, which treats ion–ion correlations in only an average manner, may have less validity in these situations. In fact, even for 1:1 electrolytes the Poisson–Boltzmann approach breaks down at sufficiently high ionic strengths. However, detailed atomic-level descriptions are currently difficult to implement for ionic solutions. Thus, the NPBE remains a useful and necessary tool for modeling salt effects in biological systems for a wide range of conditions.

The ability to solve the full nonlinear Poisson–Boltzmann equation implies that one can undertake investigations of biomolecular systems with a more accurate representation of ionic strength effects. In our studies, we have found that the electrostatic potential from the NPBE tends to be more strongly damped than with the LPBE because the ions are allowed to fully respond to the molecular charge. As this charge increases in magnitude, the resulting electrostatic potential grows only logarithmically with the NPBE rather than linearly as with the LPBE. This mechanism tends to mitigate the biological effects of highly charged systems and can be of importance near the active sites of enzymes where large concentrations of charge are sometimes found. As one application, we have briefly examined pos-

sible consequences on computer simulations of diffusion-controlled reactions, although such considerations will be of significance whenever continuum models of protein electrostatics are employed. It is clear that the multigrid damped inexact Newton algorithm described here can be of use in such studies.

ACKNOWLEDGMENTS

This work is based in part on a Ph.D. thesis submitted by M.H. to the University of Illinois. We are grateful to J.A. McCammon for providing us with a copy of the UHBD program. We also thank A. Nicholls for helpful discussions. We appreciate the comments of the anonymous referees for stimulating us to clarify the presentation of the Methods section. This work was supported in part by NIH Grant (S.S.) RO1 GM46535 (subcontract from Texas A & M), NSF Grant (F.S.) ASC 92 09502 RIA, DOE Grant (M.H.) DE-FG02-91ER25099, and a grant from FMC Corporation (S.S.). We thank the National Center for Supercomputing Applications for providing access to various computational resources.

REFERENCES

1. Debye, P., Hückel, E. On the theory of electrolytes: Freezing point depression and related phenomena. In: "The Collected Works of Peter J.W. Debye," New York: Interscience, 1923: pp. 217–263.
2. Warshel, A., Russell, S. T. Calculations of electrostatic interactions in biological systems and in solution. Quart. Rev. Biophys. 17:238–422, 1984.
3. Harvey, S. C. Treatment of electrostatic effects in macromolecular modeling. Proteins 5:78–92, 1989.
4. Davis, M. E., McCammon, J. A. Electrostatics in biomolecular structure and dynamics. Chem. Rev. 90:509–521, 1990.
5. Sharp, K. A., Honig, B. Electrostatic interactions in macromolecules: Theory and applications. Annu. Rev. Biophys. Biophys. Chem. 19:301–332, 1990.
6. Davis, M. E., Madura, J. D., Luty, B. A., McCammon, J. A. Electrostatics and diffusion of molecules in solution: Simulations with the University of Houston Brownian dynamics program. Comp. Phys. Commun. 62:187–197, 1991.
7. Niedermeier, C., Schulten, K. Molecular dynamics simulations in heterogeneous dielectrica and Debye-Hückel media—application to the protein bovine pancreatic trypsin inhibitor. Technical report, Department of Physics and Beckman Institute, University of Illinois at Urbana-Champaign, 1990.
8. Sharp, K. A. Incorporating solvent and ion screening into molecular dynamics using the finite-difference Poisson-Boltzmann method. J. Comput. Chem. 12:454–468, 1991.
9. Holst, M. Multilevel methods for the Poisson-Boltzmann equation. Ph.D. thesis, Numerical Computing Group, Department of Computer Science, University of Illinois at Urbana-Champaign, 1993.
10. Tanford, C. "Physical Chemistry of Macromolecules." New York: Wiley, 1961.
11. Brenner, S. L., Roberts, R. E. A variational solution of the Poisson-Boltzmann equation for a spherical colloidal particle. J. Phys. Chem. 77:2367–2370, 1973.
12. Fujita, H. On the nonlinear equations $\Delta u + e^u = 0$ and $\partial v/\partial t = \Delta v + e^v$. Bull. Am. Math. Soc. 75:132–135, 1969.
13. Ting, A. C., Chen, H. H., Lee, Y. C. Exact solutions of a nonlinear boundary value problem: the vortices of the two-dimensional sinh-Poisson equation. Physica D 26:37–66, 1987.
14. Davis, M. E., McCammon, J. A. Solving the finite difference linearized Poisson-Boltzmann equation: A comparison of relaxation and conjugate gradient methods. J. Comput. Chem. 10(3):386–391, 1989.
15. Gilson, M. K., Sharp, K. A., Honig, B. H. Calculating the electrostatic potential of molecules in solution: Method and error assessment. J. Comput. Chem. 9:327–335, 1988.
16. Juffer, A. H., Botta, E. F. F., van Keulen, B. A. M., van der Ploeg, A., Berendsen, H. J. C. The electric potential of a macromolecule in a solvent: A fundamental approach. J. Comput. Phys. 97:144–171, 1991.
17. Nicholls, A., Honig, B. A rapid finite difference algorithm, utilizing successive over-relaxation to solve the Poisson-Boltzmann equation. J. Comput. Chem. 12:435–445, 1991.
18. Yoon, B. J., Lenhoff, A. M. A boundary element method for molecular electrostatics with electrolyte effects. J. Comput. Chem. 11:1080–1086, 1990.
19. Warwicker, J., Watson, H. C. Calculation of the electric potential in the active site cleft due to α-helix dipoles. J. Mol. Biol. 157:671–679, 1982.
20. Ortega, J. M., Rheinboldt, W. C. "Iterative Solution of Nonlinear Equations in Several Variables." New York: Academic Press, 1970.
21. Allison, S. A., Sines, J. J., Wierzbicki, A. Solutions of the full Poisson-Boltzmann equation with application to diffusion-controlled reactions. J. Phys. Chem. 93:5819–5823, 1989.
22. Jayaram, B., Sharp, K. A., Honig, B. The electrostatic potential of B-DNA. Biopolymers 28:975–993, 1989.
23. Luty, B. A., Davis, M. E., McCammon, J. A. Solving the finite-difference non-linear Poisson-Boltzmann equation. J. Comput. Chem. 13:1114–1118, 1992.
24. Rashin, A. A., Malinsky, J. New method for the computation of ionic distribution around rod-like polyelectrolytes with helical distribution of charges. I. General approach and a nonlinearized Poisson-Boltzmann equation. J. Comput. Chem. 12:981–993, 1991.
25. Sharp, K. A., Honig, B. Calculating total electrostatic energies with the nonlinear Poisson-Boltzmann equation. J. Phys. Chem. 94:7684–7692, 1990.
26. Oberoi, H., Allewell, N. M. Multigrid solution of the nonlinear Poisson-Boltzmann equation and calculation of titration curves. Biophys. J. 65:48–55, 1993.
27. Fletcher, R., and Reeves, C. Function minimization by conjugate gradients. Comput. J. 7:149–154, 1964.
28. Holst, M., Saied, F. Multigrid solution of the Poisson-Boltzmann equation. J. Comput. Chem. 14:105–113, 1993.
29. Bank, R. E., Dupont, T. F. An optimal order process for solving finite element equations. Math. Comp. 36:35–51, 1981.
30. Bramble, J. H., Pasciak, J. E. New convergence estimates for multigrid algorithms. Math. Comp. 49:311–329, 1987.
31. Hackbusch, W. "Multi-grid Methods and Applications." Springer-Verlag, Berlin, Germany, 1985.
32. de Zeeuw, P. M. Nonlinear multigrid applied to a one-dimensional stationary semiconductor model. SIAM J. Sci. Statist. Comput. 13:512–530, 1992.
33. Hackbusch, W. On the fast solutions of nonlinear elliptic equations. Numer. Math. 32:83–95, 1979.
34. Hackbusch, W., Reusken, A. On global multigrid convergence for nonlinear problems. In: "Robust Multigrid Methods." Hackbusch, W. ed. Vieweg: Braunschweig, 1988, pp. 105–113.
35. Hackbusch, W., Reusken, A. Analysis of a damped nonlinear multilevel method. Numer. Math. 55:225–246, 1989.
36. Reusken, A. Convergence of the multigrid full approximation scheme for a class of elliptic mildly nonlinear boundary value problems. Numer. Math. 52:251–277, 1988.
37. Reusken, A. Convergence of the multilevel full approximation scheme including the V-cycle. Numer. Math. 53: 663–686, 1988.
38. Brandt, A. Multi-level adaptive solutions to boundary-value problems. Math. Comp. 31:333–390, 1977.
39. Briggs, W. L. "A Multigrid Tutorial." Philadelphia, PA: SIAM, 1987.
40. Klapper, I., Hagstrom, R., Fine, R., Sharp, K., Honig, B. Focusing of electric fields in the active site of cu-zn superoxide dismutase: Effects of ionic strength and amino-acid modification. Proteins 1:47–59, 1986.
41. Varga, R. S. "Matrix Iterative Analysis." Englewood Cliffs, NJ: Prentice-Hall, 1962.

42. Davis, H. T. "Introduction to Nonlinear Differential and Integral Equations." New York: Dover, 1960.
43. Bank, R. E., Rose, D. J. Analysis of a multilevel iterative method for nonlinear finite element equations. Math. Comp. 39:453–465, 1982.
44. Bank, R. E. A multi-level iterative method for nonlinear elliptic equation. In: "Proceedings of the Conference on Elliptic Problem Solvers." Birkhoff, G., Schoenstadt, A., eds. New York: Academic Press, 1984.
45. Bank, R. E., Rose, D. J. Parameter selection for Newton-like methods applicable to nonlinear partial differential equations. SIAM J. Numer. Anal. 17:806–822, 1980.
46. Bank, R. E., Rose, D. J. Global approximate Newton methods. Numer. Math. 37:279–295, 1981.
47. Dembo, R. S., Eisenstat, S. C., Steihaug, T. Inexact Newton methods. SIAM J. Numer. Anal. 19:400–408, 1982.
48. Eisenstat, S. C., Walker, H. F. Globally convergent inexact Newton methods. Technical report, Dept. of Mathematics and Statistics, Utah State University, 1992.
49. Holst, M., Saied, F. Multilevel methods for three-dimensional nonlinear Poisson equations. Technical Report no. UIUCDCS-R-93-1821, Numerical Computing Group, Department of Computer Science, University of Illinois at Urbana-Champaign, 1993.
50. Jorgensen, W. L., Tirado-Rives, J. The OPLS [optimized potentials for liquid simulations] potential functions for crystals of cyclic peptides and crambin. J. Am. Chem. Soc. 110:1657–1669, 1988.
51. Teeter, M. M. Water structure of a hydrophobic protein at atomic resolution: Pentagon rings of water molecules in crystals of crambin. Proc. Natl. Acad. Sci. U.S.A. 81:6014–6018, 1984.
52. Wlodawer, A., Nachman, J., Gilliland, C. L., Gallagher, W., Woodward, C. Structure of form III crystals of bovine pancreatic trypsin inhibitor. J. Mol. Biol. 198:469–480, 1987.
53. Sheriff, S., Silverton, S., Padlan, E. A., Cohen, G. H., Smith-Gill, S. J., Finzel, B. C., Davies, D. R. Three-dimensional structure of antibody-antigen complex. Proc. Natl. Acad. Sci. U.S.A. 84:8075–8079, 1987.
54. Tainer, J. A., Getzoff, E. D., Beem, K. M., Richardson, J. S., Richardson, D. C. Determination and analysis of the 2 Å structure of copper, zinc superoxide dismutase. J. Mol. Biol. 160:181–216, 1982.
55. Tainer, J. A., Getzoff, E. D., Richardson, J. S., Richardson, D. C. Structure and mechanism of copper, zinc superoxide dismutase. Nature (London) 306:284–287, 1983.
56. Arnold, E., Vriend, G., Luo, M., Griffith, J. P., Kamer, G., Erickson, J. W., Johnson, J. E., Rossmann, M. G. The structure determination of a common cold virus, human rhinovirus 14. Acta Crystallogr. Sect. A 43:346–361, 1987.
57. Hyde, C. C., Ahmed, S. A., Padlan, E. A., Miles, E. W., Davies, D. R. Three-dimensional structure of the tryptophan synthase $\alpha_2\beta_2$ multienzyme complex from *Salmonella typhimurium*. J. Biol. Chem. 263:17857–17871, 1988.
58. Kozack, R. E., Subramaniam, S. Brownian dynamics simulations of molecular recognition in an antibody-antigen system. Protein Sci. 2:915–926, 1993.
59. Holst, M., Kozack, R. E., Saied, F., Subramaniam, S. Protein electrostatics: Rapid multilvel solution of the full nonlinear poisson-boltzmann equation. Submitted.
60. Davis, M. E., Madura, J. D., Sines, J., Luty, B. A., Allison, S. A., McCammon, J. A. Diffusion-controlled enzymatic reactions. Methods Enzymol. 202:478–497, 1990.
61. Ermak, D. L., McCammon, J. A. Brownian dynamics with hydrodynamic interactions. J. Chem. Phys. 69:1352–1360, 1978.
62. Northrup, S. H., Smith, J. D., Boles, J. O., Reynolds, J. C. L. The effect of dipole moment on diffusion controlled biomolecular reaction rates. J. Chem. Phys. 84:5536–5544, 1986.
63. Northrup, S. H., Erickson, H. P. Kinetics of protein-protein association explained by brownian dynamics computer simulation. Proc. Natl. Acad. Sci. U.S.A. 89:3338–3342, 1992.
64. Raman, C. S., Jemmerson, R., Nall, B. T., Allen, M. J. Diffusion-limited rates for monoclonal antibody binding to cytochrome *c*. Biochemistry 31:10370–10379, 1992.
65. Smith-Gill, S. J., Wilson, A. C., Potter, M., Prager, E. M., Feldmann, R. J., Mainhart, C. R. Mapping the antigenic epitope for a monoclonal antibody against lysozyme. J. Immunol. 128:314–322, 1982.
66. Lavoie, T. B., Kam-Morgan, L. N. W., Hartman, A. B., Mallett, C. P., Sheriff, S., Saroff, D. G., Mainhart, C. R. Hamel, P. A., Kirsch, J. F., Wilson, A. C., Smith-Gill, S. J. Structure-function relationships in high-affinity antibodies to lysozyme. In: "The Immune Response to Structurally Defined Proteins: The Lysozyme Model." Smith-Gill, S.J., Secarz, E.E., eds. New York: Adenine Press, 1989.
67. Allison, S. A., Ganti, G., McCammon, J. A. Simulation of the diffusion-controlled reaction between superoxide and superoxide dismutase i. simple models. Biopolymers 24: 1323–1336, 1985.
68. Allison, S. A., Northrup, S. H., McCammon, J. A. Simulation of biomolecular diffusion and complex formation. Biophys. J. 49:167–175, 1986.
69. Sharp, K., Fine, R., Honig, B. Computer simulation of the diffusion of a substrate to the active site of an enzyme. Nature (London) 236:1460–1463, 1987.
70. Sharp, K., Fine, R., Schulten, K., Honig, B. Brownian dynamics simulation of diffusion to irregular bodies. J. Phys. Chem. 91:3624–3631, 1987.
71. Allison, S. A., Bacquet, R. J., McCammon, J. A. Simulation of the diffusion-controlled reaction between superoxide and superoxide dismutase II. Detailed models. Biopolymers 27:251–269, 1988.
72. Sines, J. J., Allison, S. A., McCammon, J. A. Point-charge distributions and electrostatic steering in enzyme-substrate encounter: Brownian dynamics of modified copper-zinc superoxide dismutases. Biochemistry 29:9403–9412, 1990.
73. Sines, J. J., McCammon, J. A., Allison, S. A. Kinetic effects of multiple charge modifications in enzyme-substrate reactions: Brownian dynamics simulations of cu,zn superoxide dismutases. J. Comput. Chem. 13:66–69, 1992.
74. Getzoff, E. D., Fisher, C. L., Parge, H. E., Viezzoli, M. S., Banci, L., Hallewell, R. A. Faster superoxide dismutase mutants designed by enhancing electrostatic steering. Nature (London) 330:84–86, 1992.
75. Shen, J., Subramaniam, S., Wong, C. F., McCammon, J. A. Superoxide dismutase: Fluctuations in the structure and solvation of the active site channel studied by molecular dynamics simulation. Biopolymers 28:2085–2096, 1989.
76. Hyde, C. C., Miles, E. W. The tryptophan synthase multienzyme complex: Exploring structure-function relationships with x-ray crystallography and mutagenesis. Bio/Technology 8:27–32, 1990.

Biophysical Journal Volume 68 March 1995 807–814

Computer Modeling of Electrostatic Steering and Orientational Effects in Antibody-Antigen Association

Richard E. Kozack,*‡ Michael J. d'Mello,*§ and Shankar Subramaniam*‡

*National Center for Supercomputing Applications, ‡Department of Physiology and Biophysics and Beckman Institute for Advanced Science and Technology, University of Illinois at Urbana-Champaign, Urbana, Illinois 61801; and §Thinking Machines Corporation, Cambridge, Massachusetts 02142 USA

ABSTRACT Brownian dynamics simulations are performed to investigate the role of long-range electrostatic forces in the association of the monoclonal antibody HyHEL-5 with hen egg lysozyme. The electrostatic field of the antibody is obtained from a solution of the nonlinear Poisson-Boltzmann using the x-ray crystal coordinates of this protein. The lysozyme is represented as an asymmetric dumbbell consisting of two spheres of unequal size, an arrangement that allows for the modeling of the orientational requirements for docking. Calculations are done with the wild-type antibody and several point mutants at different ionic strengths. Changes in the charge distribution of the lysozyme are also considered. Results are compared with experiment and a simpler model in which the lysozyme is approximated by a single charged sphere.

INTRODUCTION

The recognition of a specific antigen by an antibody molecule is an important component of immune response. Recent investigations employing both experimental techniques and computational modeling indicate that the rate of association between antigen and antibody is diffusion limited. Stopped-flow spectrophotometric experiments on the monoclonal antibody 2B5 raised against cytochrome *c* yield a viscosity-dependent rate constant that is consistent with such behavior (Raman et al., 1992). More recently, this behavior has also been observed in the D1.3-lysozyme system (J. Foote, Fred Hutchinson Cancer Research Center, 1994 personal communication). In addition, Brownian dynamics computer simulations on a schematic antibody-antigen system yield association rates with the proper order of magnitude (Northrup and Erickson, 1992). Earlier theoretical arguments (Creighton, 1982), whereby the Schmoluchowski reaction rate for two diffusing spheres is multiplied by the probability that they will approach each other in the precise geometry required for docking, had suggested a much smaller rate. The key to the numerical result is the entrapment of the proteins upon collision by the surrounding solvent, allowing the antibody and antigen to reorient themselves during an encounter, thus making a reaction more likely (Northrup and Erickson, 1992).

Because a given antibody has a high affinity for its corresponding antigen, it is likely there exists a mechanism beyond random diffusive motion for enhancing the association rate. An interesting proposal has been put forth that hydrodynamic forces can help pull proteins of complimentary shape together as they approach each other in solution (Brune and Kim, 1994). Another way in which the reaction rate can be increased is through the action of long-range electrostatic forces, which can maneuver the two proteins into a configuration favorable for binding, a phenomenon known as electrostatic steering (Davis et al., 1991b). Evidence of this effect was found in the cytochrome *c*-antibody experiments (Raman et al., 1992), in which the reaction rates decreased with increasing ionic strength. Such a feature raises the possibility that the association rate can be altered by point mutations that change the long-range steering forces. This means that antibodies can be engineered with either increased or decreased affinities for a given antigen through rational alterations of their electrostatic charge distributions.

The purpose of this study is to model electrostatic steering through Brownian dynamics simulations for a specific antibody-antigen complex and thus simulate in a more realistic manner the rates of encounter. We extend a previous study of ours (Kozack and Subramaniam, 1993) in two important ways. First we implement a recently developed algorithm (Holst, 1993; Holst et al., 1994a, b) for solving the full nonlinear Poisson-Boltzmann equation for the electrostatic field generated by a protein rather than employing a linearized approximate form. This enables us to model the effects of electrolytic ions in the surrounding solvent more accurately. Second, and more importantly, we employ a model that includes the orientational aspects of antibody-antigen association, instead of modeling the antigen as a simple charged sphere. Whereas our earlier work focused on relative reaction rates induced by point mutations, the model system used here gives absolute reaction rates that are similar to those observed for antibody-antigen complexes. In this regard, the computations described here are the first simulations of antibody-protein association that include realistic electrostatic steering fields. It should be pointed out that modeling of the substrate in greater detail has been carried out in cytochrome association reactions (Northrup et al.,

Received for publication 22 August and in final form 6 December 1994.

Address reprint requests to Dr. Shankar Subramaniam, Department of Physiology and Biophysics, Beckman Institute for Advanced Science and Technology, University of Illinois at Urbana-Champaign, Urbana, IL 61801. Tel.: 217-244-4489; Fax: 217-244-2909; E-mail: shankar@uiuc.edu.

0006-3495/95/03/807/08 $2.00

1987, 1993). Calculations with such detailed models are being explored in the association of the antibody-antigen complex.

As before, the system chosen for study is the complex between the monoclonal antibody HyHEL-5 and hen egg lysozyme. A 2.8-Å resolution crystal structure of the complex is available (Sheriff et al., 1987), and this system has long been studied as a model for antigen-antibody interactions. Electrostatic forces are of considerable importance in this system. The lysozyme itself has a large positive charge of +8e, and the stability of the system is mediated by three salt bridges involving residues Glu-H35 and Glu-H50 from the antibody and Arg-45 and Arg-68 of the lysozyme. Thermodynamic measurements show that the association enthalpy for the proteins is large and negative (Hibbits, et al., 1994). In addition, work with both natural (Smith-Gill et al., 1982) and designed (Lavoie et al., 1989) lysozyme mutants indicates that even conservative mutations of the abovementioned Arg residues can have a dramatic impact on the binding affinity of the two proteins. On the theoretical side, both free-energy calculations (Slagle et al., in press) and the Brownian dynamics studies cited above (Kozack and Subramaniam, 1993) have demonstrated the significant role played by charged residues in the formation of the complex.

An outline of our study is as follows. The crystallographic atomic coordinates of the Fv portion of HyHEL-5 were used to generate a charge distribution, which was in turn inserted into the nonlinear Poisson-Boltzmann equation to determine its electrostatic steering field. The lysozyme, which was modeled as an asymmetric dumbbell of two charged spheres, underwent Brownian motion in the field of the antibody. This representation is computationally simple, yet sufficiently detailed to capture the specific orientational nature of antibody-antigen docking. Because the reaction rate was obtained from an average over a large number of independent diffusive trajectories, the simulations were especially suited for massively parallel architectures, and issues related to this topic are briefly discussed. The enhancement of the association rate from electrostatic steering was investigated for the wild-type system and the effect of using the full nonlinear Poisson-Boltzmann equation for the electrostatic portion of the calculation was considered. Simulations for various solvent viscosities and ionic strengths were performed, and the results were compared with the 2B5-cytochrome c data. The effects of mutations are modeled both by varying the charge distribution of the model lysozyme and by making alterations of charged and uncharged residues on the antibody. This demonstrates how changes in the electrostatic properties of the systems are reflected in the reaction rate and allows us to address questions relevant to the design of more efficient antibodies.

MATERIALS AND METHODS

Brownian dynamics simulations

Brownian dynamics is a well established technique for modeling diffusion-controlled biomolecular reactions (Allison et al., 1988; Davis et al., 1991b; Getzoff et al., 1992; Northrup, 1994) and, in contrast with more commonly used molecular dynamics simulations, allows one to probe time scales of experimental interest. The simplification that makes this possible is the treatment of the solvent as a continuum both in terms of its electrostatic properties and its effect on the relative motion of the proteins. The electrostatic steering field obeys the nonlinear Poisson-Boltzmann equation (Sharp, 1994) for the potential ϕ, which for a 1:1 electrolyte is

$$-\nabla \cdot \epsilon \nabla u + \epsilon \kappa^2 \sinh u = \frac{e\rho}{kT} \tag{1}$$

with the "dimensionless" potential u defined as

$$u = \frac{e\phi}{kT}, \tag{2}$$

where e is the elementary unit of charge and kT is the Boltzmann factor. The right side of Eq. 1 is linear in ρ, the charge density of the protein, and contains all of the crystallographic information. The second term on the left side of the equation is nonzero only in the region outside the protein and gives the modification of the potential by the solvent and the ionic medium. The quantity ϵ is the dielectric constant and κ is the inverse Debye length, which is proportional to the square root of the ionic strength I. The remaining gradient term in the Poisson-Boltzmann equation reflects its origin in Gauss' Law of Electrostatics.

Once the electrostatic potential has been obtained, its influence on Brownian motion is determined from an algorithm developed by Ermak and McCammon (1978), which is a discrete version of the Langevin equation. For a composite structure consisting of N particles, the displacement vector $\Delta \mathbf{r}$ has $3N$ degrees of freedom and is given by

$$\Delta \mathbf{r} = (kT)^{-1} D \mathbf{F} \Delta t + \mathbf{R}, \tag{3}$$

where Δt is the time step, D is the $3N \times 3N$ diffusion tensor, $\mathbf{F}$ is the force vector, and $\mathbf{R}$ is a $3N$-dimensional random vector satisfying certain statistical constraints. More generally, the above equation includes an additional term that depends on the spatial derivatives of D; however, this term identically vanishes for the types of hydrodynamic interactions assumed here. Typically, a Brownian dynamics simulation is initiated with the two reacting molecules separated by a distance b, beyond which the long-range electrostatic forces are spherically symmetrical. Then Eq. 3 is employed to generate a trajectory that is terminated when either a predetermined reaction condition is satisfied, or the intermolecular separation becomes greater than a second distance q, which is larger than b. Because of the appearance of the random force term, which partly represents the interaction of the proteins with the surrounding solvent, each trajectory is not fully deterministic, and thus many trajectories are run to obtain a reaction probability β. The experimentally measurable association rate k is then given by Northrup et al. (1984)

$$k = \frac{k_s(b)\beta}{1 - (1 - \beta)k_s(b)/k_s(q)}, \tag{4}$$

where $k_s(a)$ is the analytical result for the diffusion rates of a point particle to spheres of radius a which can be written as

$$k_s(a) = 4\pi D \left[\int_a^\infty \frac{\exp(U(r)/kT)}{r^2} \, dr \right]^{-1}, \tag{5}$$

where $U(r)$ denotes the longrange potential.

Model system

Below we describe the application of Brownian dynamics methods to the HyHEL-5-lysozyme complex with emphasis placed on how the present model differs from our earlier simulations of the same system. As was done previously, only the Fv fragment of the antibody is considered in the calculations. The atomic coordinates are taken from the x-ray structure and the shape of the protein is defined by assigning optimized parameters for liquid simulations radii (Jorgensen and Tirado-Rives, 1988) to each heavy atom.

The charge distribution is built up from 38 sites assigned to the Asp, Glu, Arg, and Lys residues and the N-termini, yielding an overall net charge of 0. The electrostatic potential around the protein is found by solving the full nonlinear Poisson-Boltzmann equation using the multigrid damped inexact Newton algorithm (Holst et al., 1994a, b). In the earlier study, we used a linearized approximation to Eq. 1. The differences between the linear and nonlinear models are explored in a subsequent section of the paper. To implement the multigrid-Newton algorithm, a finite-difference formulation of the Poisson-Boltzmann equation (Warwicker and Watson, 1982) is made on a cubic grid measuring 127 nodes on a side at 1 Å resolution. As was done previously, the grid is centered at the point where the diagonal moments of the electric quadrupole tensor vanish and the boundary condition on the outer faces is generated by assuming that each charge contributes to the potential as if it were an independent Debye-Hückel sphere of radius 2 Å. The electrostatic calculations were performed on a Convex 3880 with the resulting potential grids being transferred to other machines for the purpose of running Brownian trajectories.

The lysozyme, which undergoes diffusive motion in the force field of the antibody, is represented as an asymmetrical dumbbell consisting of two spheres. A rough superposition of this model is displayed in Fig. 1 over a stick representation of the actual Fv-lysozyme complex. The smaller sphere, which approximates the two salt link-forming Arg residues, has a radius of 4.0 Å and a charge of +2e. The larger sphere, which models the remaining bulk of the protein, is assigned a radius of 20.0 Å and a charge of +6e. The distance between the centers of the spheres is equal to 24 Å, or the sum of their radii. Except for one case indicated below, it is assumed that there are no hydrodynamic interactions between the spheres. The lysozyme is kept rigid during the trajectories by applying a line of centers technique (Luty et al., 1993), in which a constraining correction is applied along the vector between the spheres after each time step. In our previous simulations only the smaller sphere was used to represent the lysozyme, whereas the present model is more realistic and allows for a description of the strict orientational constraints in protein-protein docking. As mentioned above, this means that reasonable absolute values for the association rate can be obtained.

The initial antibody-lysozyme separation b and the termination distance q are taken to be 80 and 500 Å, respectively. The time step is variable depending on the relative separation with a minimum value of 0.5 ps. The reaction condition, defined in terms of the smaller lysozyme sphere and the δ carbon of Glu-H50, is met when the centers of these two atoms are within 6.5 Å of each other. This distance, which was chosen to accurately reflect protein-protein reaction rates, differs from the 8.5 Å that was used in the earlier simulations to give high reaction probabilities and hence better statistics. Because of the comparatively low reaction rate, many more trajectories are computed than in the single-sphere model to get acceptable statistical errors. At least 300,000 trajectories were run to get each data point that is presented; in most cases at least 500,000 trajectories were sampled, and in a few examples a million or more trajectories were sampled. This portion of the calculation was done either on an SGI Challenge machine at the National Center for Supercomputing Applications, in single-processor mode or as a massively-parallel problem on the CM-5 from Thinking Machines Corporation (Cambridge, MA).

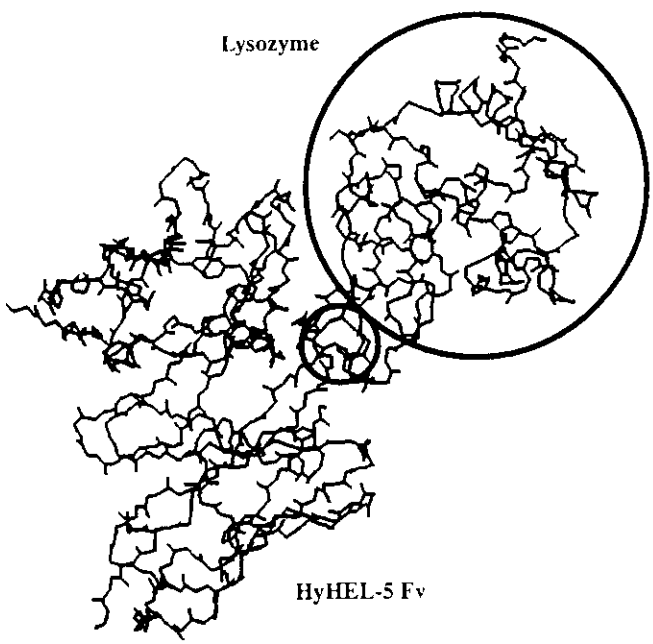

FIGURE 1 The two-sphere model of the lysozyme approximately superposed over a stick representation of the crystal structure for the Fv-lysozyme complex.

Computational issues

The UHBD software package (Davis et al., 1991a) provided the basis for our computations, although several key modifications of the code were made. One was implemented to enable the use of diffusing substrates that contain spheres of different sizes as in the asymmetric dumbbell model of the lysozyme. This was necessary to account correctly for simple collisions between antibody and antigen. A more extensive change involved the insertion of the multigrid-based Newton method for solving the nonlinear Poisson-Boltzmann, which has already been described in detail (Holst et al., 1994a). A final major modification required a reworking of the program for use on the CM-5. Other workers (Bagheri et al., 1993) have discussed the issue of parallelism with UHBD for machines with up to 10 processors. Below we concern ourselves with the deployment of the hundreds of processing nodes that are available on the CM-5.

Only the Brownian dynamics portion of the calculation has been run on the CM-5. Because this part of the code involves the running of many independent trajectories, it easily lends itself to parallelization on a large scale, and we have essentially followed a procedure similar to that for the more coarse-grained parallel machines (Bagheri et al., 1993). The basic outline of our program can be summarized in four steps. The electrostatic potential, which is efficiently calculated on a vector machine (Holst, 1993) such as the Convex and then transferred to the scalable disk array or even the front end disk of the CM-5, is first broadcast to all of the processors. Then a simple arithmetic expression based on the processor address number is used to locally modify the seed for the random number generator, which yields the stochastic force term in Eq. 4. As has been shown (Bagheri et al., 1993), this prescription leads to an independent set of the random numbers for each processor. In the third step, each of the nodes, which number m, runs a fixed number of trajectories N_t. Because each trajectory is made up of a variable number of time steps, there are differences in the work done by each node; these have been demonstrated to be small (Bagheri et al., 1993), and our experience is indeed in agreement with this. Finally, when all of the processors are done, the results from the total of mN_t trajectories are collected to find the reaction probability, which is then used to determine the rate constant.

It is shown in Fig. 2, for a series of runs with 32 processors, that the CPU time consumed in the Brownian dynamics simulations grows linearly with the total number of trajectories. The curve extrapolates to a nonzero value for zero trajectories due to overhead time required for reading in the force-field grid and tabulating the results of the run. We have also looked at the CPU time for eight different sets of random number seeds at 10 and 150 trajectories per processor and found the maximum deviation from the average to be <15% in each case. Presented in Fig. 3 is the CPU time required for running a fixed number of total trajectories with varying numbers of processors. As expected, this time decreases sharply with the number of processors. However, the speedup, defined as the CPU time for a 32-processor run divided by the CPU time for an m-processor run, scales less than linearly with m and ranges from 1.8 when the number of nodes is doubled from 32 to 64 to 6.2 for a 16-fold increase of processors. This is due to the increased importance of overhead time as the number of trajectories per processor decreases. It should be noted that the total number of trajectories has been chosen to specifically emphasize this feature, and one can obtain better speedups by simply running more trajectories. However, this exercise shows how the efficiency of the calculation is limited by the

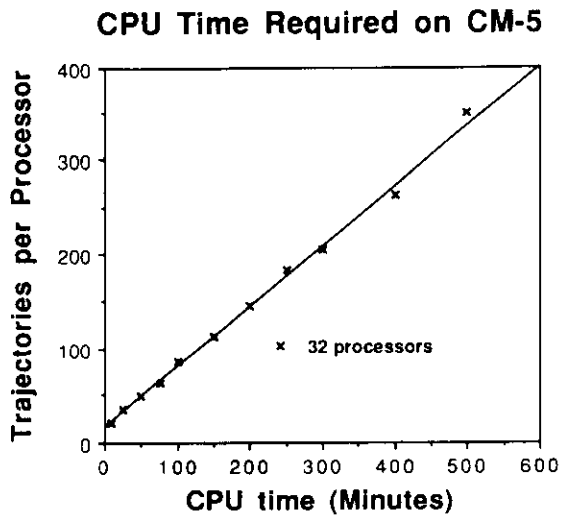

FIGURE 2 The CPU time required to run a variable number of trajectories on 32 processors of the CM-5. The y axis indicates the number of trajectories per processing node, and the straight line represents a least-squares linear fit to the data. The overhead time necessary to set up the problem and collect the results has been included.

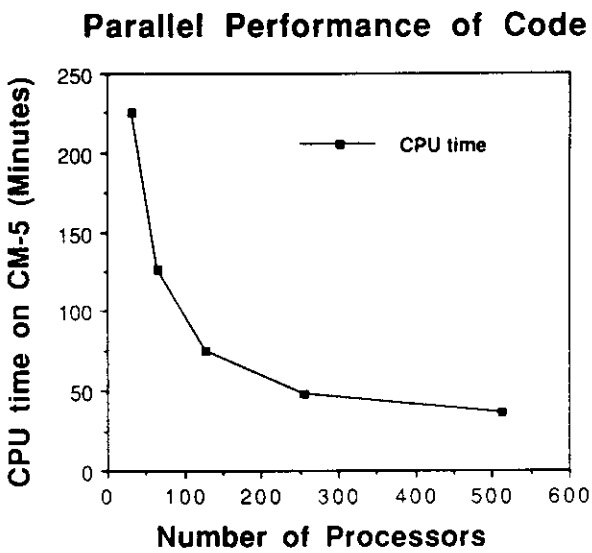

FIGURE 3 The CPU time required to run a total 10,240 trajectories of various numbers of processors on the CM-5. Each square represents actual timings, and the lines connecting the points are only for clarity. The overhead time necessary to set up the problem and collect the results has been included.

non-parallelizable portions of the program. This difficulty can be minimized with an efficient parallel implementation of a Poisson-Boltzmann solver, as this can eliminate the input/output step of reading in the potential grid.

RESULTS

Wild-type system

Simulations were performed for the wild-type system with electrostatic potentials calculated at ionic strengths of 5, 50, and 150 mM corresponding to Debye lengths of 43, 14, and 8 Å, respectively. The results are collected in Table 1 for computations in which both the full nonlinear and the linearized Poisson-Boltzmann equations are used to obtain the steering field. Measurements for the 2B5-cytochrome *c* association rates (Raman et al., 1992) are also shown. As noted above, the reaction probabilities in the model computations are small and thus the statistical error inherent in the simulation is relatively large, on the order of 10%. The experimental data points have been estimated from a graph and are therefore listed to one significant figure. The "no steering" values are found experimentally by using an extremely high ionic strength and numerically by simply turning off the electrostatic steering force.

TABLE 1 Antibody-antigen association rates

Ionic Strength	Experiment	Nonlinear	Linear
5 mM	1×10^6	8.6×10^6	4.8×10^7
50 mM	6×10^5	2.4×10^6	7.3×10^6
150 mM	4×10^5	1.7×10^6	2.4×10^6
No steering	3×10^5	8.0×10^5	8.0×10^5

Comparison of calculated and observed antibody-antigen association rates in units of $M^{-1} s^{-1}$. The first column is the experimental data for the 2B5-cytochrome *c* system cited in the text, the second column is the simulation for the model HyHEL-5-lysozyme system where the nonlinear Poisson-Boltzmann equation has been used to calculate the steering field, and the third column is the same as the second except that the linearized approximation to the Poisson-Boltzmann equation is used. The "no steering" row indicates that electrostatic fields are not employed in the computations, and for the experiment means that an ionic strength of 1000 mM was used. The experimental results, given to one significant figure, were estimated from a graph, and the error in the simulated rates is on the order of 10%.

The computed reaction rate decreases with ionic strength, indicative of favorable electrostatic steering. The rates for the nonlinear calculation are roughly the same magnitude as, although a bit higher than, the corresponding experimental results. The variation in the rate with respect to ionic strength is greater for the simulated antibody-lysozyme system. These discrepancies could be due to specific features of the different systems, approximations implied in the modeling, or perhaps a combination of both. It is also seen in Table 1 that the difference between the nonlinear and linear calculations is quite considerable at 5 mM, but decreases as the ionic strength drops to 50 and then to 150 mM. This agrees with expectations that the linearized approximation of the Poisson-Boltzmann equation improves with increasing salt concentration. These results also match those of previous studies in which it is found that the linearized equation tends to exaggerate the effects of electrostatic steering (Allison et al., 1989; Holst et al., 1994a). Finally, the results from the linear calculations are further from the observations than the nonlinear calculations. Hereafter, all of the reaction rates presented in this paper are determined by using the full nonlinear Poisson-Boltzmann equation.

Because the experimental results on the cytochrome *c*-antibody complex (Raman et al., 1992) and the D1.3-lysozyme system (J. Foote, personal communication) include studies of the viscosity dependence of the association rate, we have considered the effect of varying the viscosity in our

simulations. The effect on the reaction rate can be written as

$$k_0/k = A + B\eta_{rel}, \quad (6)$$

where A and B are constants, k_0 is the reaction rate when the solvent is water, k is the reaction rate in the viscous medium, and η_{rel} is the ratio of the viscosity to that of water. The above-cited empirical results agree well with Eq. 6 when $A = 0$ and $B = 1$, which are values that would be expected for a diffusion-controlled reaction (Kramers, 1940). In Fig. 4 are the rates for the wild-type system at 5 mM ionic strength where the ratio of the viscosity to that of water η_{rel} ranges from 1.0 to 2.2. The error bars are estimated by assuming that the fractional error is equal to the square root of the number of trajectories that result in a reaction, a procedure followed for all the graphs in this paper. A least-squares fit to the function k_0/η_{rel} is also shown in Fig. 4 and can be seen to reproduce the trend of the data.

The aim of this investigation is to examine electrostatic steering in antibody-antigen docking from realistic fields; thus, no attempt has been made to calculate any steering forces due to hydrodynamic interactions between the proteins. A simple estimate that the hydrodynamic forces can be much stronger has been based on an electrostatic force between two dipolar proteins (Brune and Kim, 1994). However, from Brownian dynamics simulations it is generally found that the local field around the active site is what determines the amount of electrostatic steering relevant to the reaction rate. For example, bovine superoxide dismutase and its substrate have net charges of the same sign (Sines et al., 1990), and in the present case the antibody is electrically neutral, yet both systems exhibit substantial favorable electrostatic steering. As far as hydrodynamic interactions internal to a protein are concerned, we feel that our model lysozyme is too elementary to justify their detailed consideration. We did perform one simulation, without electrostatic forces, in which an Oseen tensor (Dickinson, 1985) is employed to describe hydrodynamic interactions between the two lysozyme spheres. This resulted in a rate constant that was larger only by about a factor of 2 over the case in which no hydrodynamic interactions were employed.

Lysozyme mutants

One of the most important applications of Brownian dynamics simulations is the assessment of the effect of mutations on the reaction rate. Even though the model lysozyme is quite simple, we can still examine how the association rate depends on its charge distribution. In Fig. 5 are the results of simulations where the charge has been altered on the smaller lysozyme sphere, which is meant to model the two Arg residues that form salt bridges in the antibody-antigen complex. The changes are mainly manifest at 5 mM ionic strength, where the rate is [2/3] of the wild-type value for a reduction of one charge unit and 1/5 of wild-type for a reduction of two charge units. At the higher ionic strengths, the rates are within roughly a factor of 2 of the wild-type results. It is interesting to note that, within the statistical error, there is little or no change in the rate constant in going from 50 to 150 mM and at these molarities, there is no noticeable difference when the sphere contains zero or one unit of charge. Experimental results on natural and artificial mutants on the other hand have shown that antibody-lysozyme affinity is extremely sensitive to mutations of the Arg residues (Smith-Gill et al., 1982; Lavoie et al., 1987). Thus far, neither this study nor previous ones (Kozack and Subramaniam, 1993; Slagle et al., 1994) based on continuum electrostatic models have been able to reproduce this behavior. It is clear that more theoretical work, especially with atomic-level models, needs to be done to gain an understanding of this phenomenon.

As expected, the reaction rates are much less dependent on the charge on the larger lysozyme sphere, which is farther

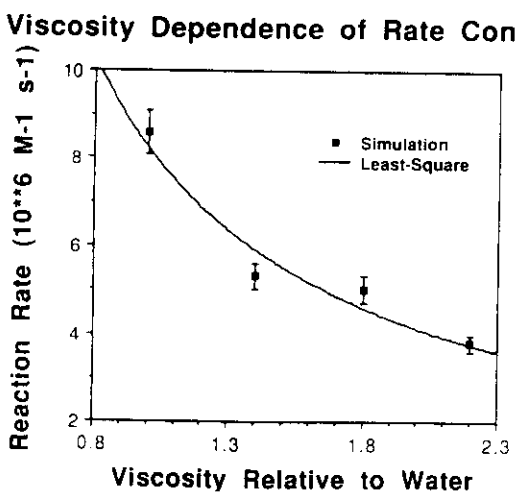

FIGURE 4 The rate constant for the wild-type model antibody-lysozyme system as a function of the solvent viscosity divided by the viscosity of water. The solid line is a least-squares fit to the function K/η where η is the viscosity.

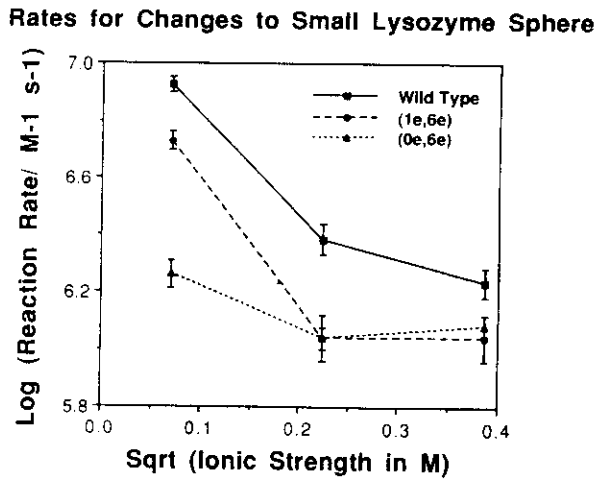

FIGURE 5 Reaction rates as a function of ionic strength for model systems in which the charge on the smaller lysozyme sphere is altered. The notation identifying the charges on each sphere is in order of (smaller, larger) so that (2e,6e) represents the wild-type system. The lines connecting the data points are for the sake of clarity.

from the reaction site. The results are given in Fig. 6. Even when the charge is neutralized from +6e, the rate decreases by only about a factor of 3 at 5 mM and even less so at higher salt concentrations. When the charge on this sphere is reduced by two units, the effect on the reaction rate is comparatively smaller and is virtually identical to the wild-type rates at 50 and 150 mM. This merely reflects what has been stated earlier, that local interactions near the binding site take precedence over the total charge of the molecule in determining the efficiency of electrostatic steering.

Antibody mutants

Since the model for the antibody is much more detailed, we can consider the effects of specific point mutations on antibody-antigen association. We have investigated a few representative cases that have had the largest impact in the single-sphere model. For mutations that decrease the reaction rate, these are the neutralizations of the Glu-H35 and the Glu-H50 residues, which form the salt links with the Arg-45 and Arg-68 residues of the lysozyme. The reaction rates are compared with those of the wild-type system in Fig. 7. The largest decrease is a factor of 5 for Glu-H50 at 5 mM ionic strength; otherwise the rates are within a factor of 2 from the wild-type complex. The relative rates, defined as the ratio of the reaction rate for the mutant system to that of the wild-type, are predicted remarkably well by the single-sphere lysozyme model at 5 mM. At higher salt concentration, the single-sphere model overestimates the effects of the mutations, although the corresponding relative rates have the same magnitude.

For mutations of HyHEL-5 that enhance the reaction rate, results are shown in Fig. 8 for Asn-to-Asp mutations at positions H59 and H100. The relative rates decrease with increasing ionic strength, which is contrary to the nonmonotonic behavior that was observed for the single-sphere model. The effect of the Asn-H100 mutation has disappeared at 150 mM, whereas the simpler model predicts a factor of 2 increase. Again the single-sphere model gives reasonable magnitudes for the relative rates, although it somewhat underestimates the low ionic strength rates. In particular, there is almost a fourfold increase for the Asn-H59 mutation at 5 mM, whereas the single-sphere model gave only a factor of 1.4 enhancements.

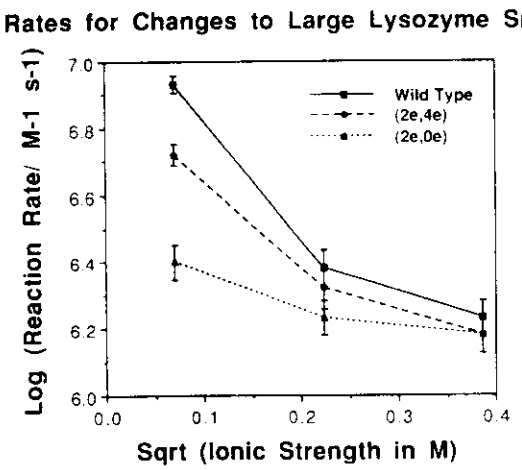

FIGURE 6 Reaction rates as a function of ionic strength for model systems in which the charge on the larger lysozyme sphere is altered. The notation identifying the charges on each sphere is in order of (smaller,larger) so that (2e,6e) represents the wild-type system. The lines connecting the data points are for the sake of clarity.

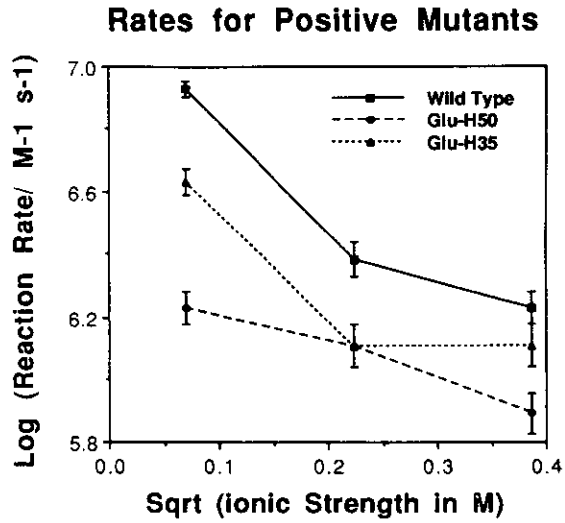

FIGURE 7 Reaction rates as a function of ionic strength for positive antibody mutants that decrease the amount of electrostatic steering. The lines connecting the data points are for the sake of clarity.

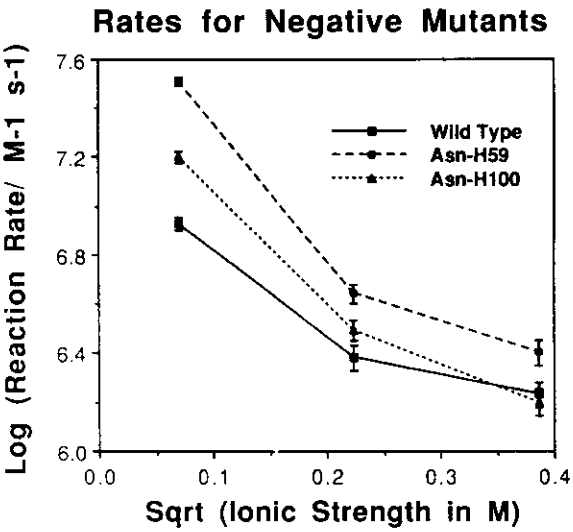

FIGURE 8 Reaction rates as a function of ionic strength for negative antibody mutants that increase the amount of electrostatic steering. The lines connecting the data points are for the sake of clarity.

DISCUSSION

For all of the mutations we have considered, both to the lysozyme and to the antibody, the observed reaction rates have been confined to the same order of magnitude as in the

wild-type system. This is in line with conclusions obtained in simulations of superoxide dismutase, where a structureless ion diffuses to an enzyme-active site (Sines et al., 1990, 1992). The changes found here are largest at lower ionic strength, at which the steering fields penetrate further out into the solvent. At the physiological ionic strength of 150 mM, the mutations yield rates that are all roughly within a factor of 2 of wild-type. The decreased importance of electrostatic steering at this salt concentration is also evident in the fact that the wild-type rate is only about twice the simulated reaction rate for the case in which no electrostatic interactions are included. The single-sphere model we previously considered, which also used the linearized Poisson-Boltzmann equation, yielded relative rates of the same magnitude as the more complicated model, although there were some notable differences, especially concerning the ionic strength dependence of the relative rates.

Our model was motivated by the desire to have a system that is relatively simple from a computational viewpoint, yet still includes orientational effects and realistic steering fields such that reasonable protein-protein association rates are obtained. Compared with our previous treatment, the electrostatics portion has been improved by using the multigrid-Newton method to solve the full nonlinear Poisson-Boltzmann equation. Given that the algorithm has been shown to scale very favorably with problem size (Holst, 1993; Holst et al., 1994a), a next step would be to solve this equation for the full Fab domain of the HyHEL-5 antibody, rather than just its Fv fragment. Although it is unlikely that this will noticeably change the steering fields because the additional charges are far from the binding site, the extra portion of the protein may possibly induce some observable steric effects. It is also possible to construct a more detailed model of the lysozyme to the point where specific mutations on the antigen can be studied. The resulting computational effort, which would probably require large amounts of CPU time on a massively parallel supercomputer, can be implemented in the manner described above. We also note that the way in which the simulation is now done, wherein the antibody is fixed and rigid, treats the proteins in an asymmetric fashion; this feature ought to be removed or at least tested, perhaps by performing a "reverse" calculation in which the antibody undergoes diffusional motion in the field of the lysozyme. In addition a symmetric calculation with both the antibody and antigen moving, with the evolution of the trajectories in a coordinate system fixed at the antibody, is feasible but computationally expensive.

There are also various physical effects that have not been considered within the framework of these Brownian dynamics studies. It would certainly be useful to perform an investigation of the intermolecular hydrodynamic interactions (Brune and Kim, 1994), with realistic molecular shapes, between antibody and antigen for an actual comparison with the electrostatic steering. It has also been suggested, through analytical solutions of the diffusion equation, that short-range van der Waals forces may be important in keeping two proteins together as they reach the optimum docking configuration (Chou and Zhou, 1982). Finally, atomic-level models can be employed to validate the results from calculations based on continuum approximations. For example, it appears increasingly likely that such models are necessary to explain the extraordinary sensitivity of the HyHEL-5-lysozyme binding affinity on mutations involving the Arg-45 and Arg-68 residues of the lysozyme.

An enormous advantage of Brownian dynamics simulations is the computation of protein-protein reaction rates that can be measured in the laboratory. As demonstrated here and elsewhere, the technique is particularly powerful for probing the effects of various mutations in a given system (Getzoff et al., 1992). The results presented here concerning the antibody mutants can be experimentally tested by performing experiments similar to those already done on the 2B5-cytochrome *c* complex and on altered systems prepared through site-directed mutagenesis. This synthesis of computer modeling using modern parallel and vector architectures and continually improving algorithms together with a growing body of experimental data and an increasing number of x-ray crystal structures can eventually provide the means for understanding protein-protein interactions and the molecular basis of immune response.

We thank J. A. McCammon for providing us with a copy of the UHBD code. This work was supported in part by National Institutes of Health grant R01 GM46535 (subcontract from Texas A & M), and National Science Foundation grant ASC 89-02829. We are grateful to the National Center for Supercomputing Applications and the Pittsburgh Supercomputing Center for allocations of computational resources.

REFERENCES

Allison, S. A., R. J. Bacquet, and J. A. McCammon. 1988. Simulation of the diffusion-controlled reaction between superoxide and superoxide dismutase. II. Detailed models. *Biopolymers.* 27:251–269.

Allison, S. A., J. J. Sines, and A. Wierzbicki. 1989. Solutions of the full Poisson-Boltzmann equation with application to diffusion-controlled reactions. *J. Phys. Chem.* 93:5819–5823.

Bagheri, B., A. Ilin, and R. Scott. 1993. Parallelizing UHBD. University of Houston report.

Brune, D., and S. Kim. 1994. Hydrodynamic steering effects in protein association. *Proc. Natl. Acad. Sci. USA.* 91:2930–2934.

Chou, K. C., and G. P. Zhou. 1982. Role of protein outside active site on the diffusion-controlled reaction of enzyme. *J. Am. Chem. Soc.* 104:1409–1413.

Creighton, T. E. 1982. Proteins: Structures and Molecular Properties. Freeman, New York.

Davis, M. E., J. D. Madura, B. A. Luty, and J. A. McCammon. 1991a. Electrostatics and diffusion of molecules in solution: Simulations with the University of Houston Brownian Dynamics program. *Comp. Phys. Comm.* 62:187–197.

Davis, M. E., J. D. Madura, J. Sines, B. A. Luty, S. A. Allison, and J. A. McCammon. 1991b. Diffusion-controlled enzymatic reactions. *Methods Enzymol.* 202:473–497.

Dickinson, E. 1985. Brownian dynamics with hydrodynamic interactions: the application to protein diffusional problems. *Chem. Soc. Rev.* 14:421–455.

Ermak, D. L., and J. A. McCammon. 1978. Brownian dynamics with hydrodynamic interactions. *J. Chem. Phys.* 69:1352–1360.

Getzoff, E. D., C. L. Fisher, H. E. Page, M. S. Viezzoli, L. Banci, and R. A. Hallewell. 1992. Faster superoxide dismutase mutants designed by enhancing electrostatic steering. *Nature.* 358:347–351.

Hibbits, K. A., D. S. Gill, and R. C. Willson. 1994. Isothermal titration calorimetric study of the association of hen egg lysozyme and the anti-lysozyme antibody HyHEL-5. *Biochemistry.* 33:3584–3590.

Holst, M. J. 1993. Multilevel methods for the Poisson-Boltzmann equation. Ph. D. thesis. Department of Computer Science, University of Illinois at Urbana-Champaign. 103–129.

Holst, M. J., R. E. Kozack, F. Saied, and S. Subramaniam. 1994a. Treatment of electrostatic effects in proteins: multigrid-based solution of the full nonlinear Poisson-Boltzmann equation. *Proteins.* 18:231–245.

Holst, M. J., R. E. Kozack, F. Saied, and S. Subramaniam. 1994b. Protein electrostatics: rapid multigrid-based Newton algorithm for solution of the full nonlinear Poisson-Boltzmann equation. *J. Biomol. Struct. Dyn.* 11: 1437–1445.

Jorgensen, W. L., and J. Tirado-Rives. 1988. The OPLS (optimized potentials for liquid simulations) potential functions for crystals of cyclic peptides and crambin. *J. Am. Chem. Soc.* 110:1657–1669.

Kozack, R. E., and S. Subramaniam. 1993. Brownian dynamics simulations of molecular recognition in an antibody-antigen system. *Protein Sci.* 2:915–926.

Kramers, H. A. 1940. *Physica (Amsterdam).* 7:284–304.

Lavoie, T. B., L. N. W. Kam-Morgan, A. B. Hartman, C. P. Mallett, S. Sheriff, D. G. Saroff, C. R. Mainhart, P. A. Hamel, J. F. Kirsch, A. C.Wilson, and S. J. Smith-Gill. 1989. Structure-function relationships in high-affinity antibodies to lysozyme. *In* The Immune Response to Structurally Defined Proteins: The Lysozyme Model. S. J. Smith-Gill and E. E. Secarz, editors. Adenine Press, New York.

Luty, B. A., R. C. Wade, J. D. Madura, M. E. Davis, J. M. Briggs, and J. A. McCammon. 1993. Brownian dynamics simulations of diffusional encounters between triose phosphate isomerase and glyceraldehyde phosphate: electrostatic steering of glyceraldehyde phosphate. *J. Phys. Chem.* 97:233–237.

Northrup, S. H. 1994. Hydrodynamic motions of large molecules. *Curr. Opin. Struct. Biol.* 4:269–274.

Northrup, S. H., S. A. Allison, and J. A. McCammon. 1984. Brownian dynamics simulation of diffusion-controlled biomolecular reactions. *J. Chem. Phys.* 80:1517–1524.

Northrup, S. H., J. O. Boles, and J. C. Reynolds. 1987. Electrostatic effects in the Brownian dynamics of association and orientation in heme proteins. *J. Phys. Chem.* 91:5991–5997.

Northrup, S. H., and H. P. Erickson. 1992. Kinetics of protein-protein association explained by Brownian dynamics computer simulation. *Proc. Natl. Acad. Sci. USA.* 89:3338–3342.

Northrup, S. H., K. A. Thomasson, C. M. Miller, P. D. Barker, L. D. Eltis, J. G. Guillemette, S. C. Inglis, and A. G. Mauk. 1993. Effects of charged amino acid mutations on the bimolecular kinetics of the reduction of yeast iso-I-ferricytochrome *c* by bovine ferrocytochrome b5. *Biochemistry.* 32: 6613–6623.

Raman, C. S., R. Jemmerson, B. T. Nall, and M. J. Allen. 1992. Diffusion-limited rates for monoclonal antibody binding to cytochrome *c*. *Biochemistry.* 31:10370–10379.

Sharp, K. A. 1994. Electrostatic interactions in macromolecules. *Curr. Opin. Struct. Biol.* 4:234–239.

Sheriff, S., E. W. Silverton, E. A. Padlan, G. H. Cohen, S. J. Smith-Gill, B. C. Finzel, and D. R. Davies. 1987. Three-dimensional structure of antibody-antigen complex. *Proc. Natl. Acad. Sci. USA.* 84: 8075–8079.

Sines, J. J., S. A. Allison, and J. A. McCammon. 1990. Point-charge distributions and electrostatic steering in enzyme-substrate encounter: Brownian dynamics of modified copper-zinc superoxide dismutases. *Biochemistry.* 29:9403–9412.

Sines, J. J., J. A. McCammon, and S. A. Allison. 1992. Kinetic effects of multiple charge modifications in enzyme-substrate reactions: Brownian dynamics simulations of Cu,Zn superoxide dismutase. *J. Comp. Chem.* 13:66–69.

Slagle, S. P., R. E. Kozack, and S. Subramaniam. 1994. Role of electrostatics in antibody-antigen association: anti-hen egg lysozyme/lysozyme complex (HyHEL-5/HEL). *J. Biomol. Struct. Dyn.* 12:439–456.

Smith-Gill, S. J., A. C. Wilson, M. Porter, E. M. Prager, R. J. Feldmann, and C. R. Mainhart. 1982. Mapping the antigenic epitope for a monoclonal antibody against lysozyme. *J. Immunol.* 128:314–322.

Warwicker, J., and H. C. Watson. 1982. Calculation of the electric potential in the active site cleft due to α-helix dipoles. *J. Mol. Biol.* 157:671–679.

Protein Science (1993), *2*, 915-926. Cambridge University Press. Printed in the USA.

Brownian dynamics simulations of molecular recognition in an antibody-antigen system

RICHARD E. KOZACK AND SHANKAR SUBRAMANIAM

National Center for Supercomputing Applications, Department of Physiology and Biophysics, and Beckman Institute for Advanced Science and Technology, University of Illinois at Urbana-Champaign, Urbana, Illinois 61801

(RECEIVED December 22, 1992; REVISED MANUSCRIPT RECEIVED February 17, 1993)

Abstract

The crystal structure for an antibody-antigen system, that of the anti-hen egg lysozyme monoclonal antibody HyHEL-5 complexed to lysozyme, is used as the starting point for computer simulations of diffusional encounters between the two proteins. The investigation consists of two parts: first, the linearized Poisson-Boltzmann equation is solved to determine the long-range electrostatic forces between antibody and antigen, and then, the relative motion as influenced by these forces is modeled within Brownian motion theory. The effects of various point mutations on the calculated reaction rate are considered. It is found that charged residues close to the binding site exert the greatest influence in steering the proteins into a configuration favorable for their binding, while more distant mutations are qualitatively described by the Smoluchowski model for the mutual diffusion of two uniformly charged spheres. The antibody residues involved in forming salt links with the lysozyme, Glu-H35 and Glu-H50, appear to be particularly important in electrostatic steering, as neutralization of both of them yields reaction rates that are two to three orders of magnitude below those of wild-type rates. The relative rates obtained from the simulations can be tested through kinetic measurements on mutant protein complexes. Kinetically efficient partners can also be designed and constructed through directed mutagenesis.

Keywords: antibody-antigen complex; Brownian dynamics simulations; diffusion-controlled reactions; electrostatic steering; molecular recognition; Poisson-Boltzmann equation

Molecular recognition in the immune system is extraordinarily specific. Advances in protein crystallography, hybridoma technology, molecular biology, and simulation methodology enable their synergistic use to obtain detailed insight into the antibody-antigen molecular recognition process (Davies et al., 1990). From stopped-flow spectrophotometric measurements of the rate of association and viscosity dependence of the reaction, it has been shown that the association of the monoclonal antibody 2B5 with cytochrome *c* is diffusion controlled (Raman et al., 1992). Also, a theoretical investigation of a model system by Northrup and Erickson (1992) has demonstrated the ability of computer simulations to reproduce the magnitude of the reaction rate expected for protein-protein encounters. These results suggest the application of Brownian dynamics methods for studying the specificity of antibody binding, and in particular for obtaining relative rates of association for wild-type and mutant complexes.

It is our purpose to model the phenomenon of molecular recognition in the immune system, in which an antibody interacts through long-range electrostatic forces with an antigen as it undergoes diffusional motion and steers into a configuration favorable for binding. Molecular recognition is especially suitable for computational study as it can be based on well-established physical models, and one can also, with presently available algorithms and resources, probe time scales of experimental interest. The results presented here can be directly correlated with kinetic experiments, help provide a deeper understanding of the forces that are responsible for recognition, and have implications for design and engineering of antibodies that have enhanced specificity.

The particular system under investigation consists of the monoclonal antibody HyHEL-5 and hen egg lysozyme. A crystal structure of this complex has been obtained to 2.8 Å resolution (Kinemage 1; Sheriff et al., 1987), and experimental results are available for the relative binding

Reprint requests to: Shankar Subramaniam, Beckman Institute, University of Illinois at Urbana-Champaign, 405 N. Mathews Avenue, Urbana, Illinois 61801.

affinities of similar lysozymes from other avian species to HyHEL-5 (Smith-Gill et al., 1982). Work involving designed mutants of these proteins is also underway (Willson, pers. comm.). Aside from this large amount of empirical information, the HyHEL-5–lysozyme system possesses some physical features that make it desirable for an investigation of molecular recognition. The lysozyme has a net total charge of +7e, and the number of contacts in the complex is minimal, being dominated by three salt bridges in a well-defined geometry. The residues involved in these links are Glu-H35 and Glu-H50, which both lie within a groove of the antibody, and Arg-45 and Arg-68 on the lysozyme. An experiment by Smith-Gill et al. (1982) showed that the binding affinity of HyHEL-5 is several orders of magnitude smaller for bobwhite quail lysozyme as compared to hen egg lysozyme. The quail enzyme has Arg-68 replaced with Lys, another positively charged residue. Also, in two directed mutant proteins, one with Arg-68 replaced by Lys and the other with Arg-45 replacing Lys, the I_{50} of the complex was found to be 10,000-fold and 750-fold, respectively, smaller compared to the recombinant native HEL protein (Lavoie et al., 1989). The change in the length of the positively charged side chains alters the local electric fields near the groove, and it might therefore be anticipated that electrostatics plays an important role in the formation of the complex.

Results

Brownian dynamics simulations

The modeling of molecular recognition consists of two parts: first, the long-range electrostatic forces between antibody and antigen are calculated, and then the relative motion of the two proteins as influenced by these forces is simulated. The techniques used for carrying out the relevant computations have been extensively developed and applied by McCammon and co-workers (Davis et al., 1990) and are collectively referred to as Brownian dynamics. The first part is accomplished through a numerical solution of the linearized Poisson-Boltzmann equation:

$$-\nabla\cdot\epsilon\nabla\phi + \epsilon\kappa^2\phi = \rho, \tag{1}$$

where ϵ is the dielectric constant, κ is the inverse Debye length, and ϕ is the electrostatic potential (Gilson & Honig, 1987; Davis & McCammon, 1989). In the above expression, the charge density ρ is determined for the protein configuration obtained from the crystal structure coordinates. The diffusional motion is propagated in discrete time steps, Δt according to the Langevin equation-based algorithm of Ermak and McCammon (1978):

$$\Delta\mathbf{r} = \frac{D}{kT}\mathbf{F}(t)\Delta t + \mathbf{R}(t), \tag{2}$$

where $\Delta\mathbf{r}$ is the change in relative position, kT is the Boltzmann factor, D is the relative diffusion constant, $\mathbf{F}(t)$ gives the electrostatic force obtained from the solution for ϕ, and $\mathbf{R}(t)$ is a random vector satisfying certain statistical constraints. Equation 2 is used to generate a series of trajectories, beginning with an intermolecular separation distance of b and terminating when either a predetermined reaction condition based on interatomic distances is satisfied or when the distance between molecules is equal to q. The determination of the b and q parameters is discussed below. The probability that a trajectory yields a successful reaction, β, can then be used to compute a reaction rate k given by (Northrup et al., 1984):

$$k = \frac{k_s(b)\beta}{1 - (1-\beta)k_s(b)/k_s(q)}, \tag{3}$$

where $k_s(a)$ is the analytical result for the reaction rate for diffusion to a sphere of radius a in a spherically symmetric potential $U(r)$, which obeys the expression

$$k_s(a) = 4\pi D\left\{\int_a^\infty \frac{\exp[U(r)/kT]}{r^2}\,dr\right\}^{-1}. \tag{4}$$

The goal of the present study is to run simulations for a large number of mutants of the HyHEL-5–lysozyme system. This will help to provide understanding on general aspects of antigen recognition, as well as guiding experimentalists as to which residues are important in electrostatic steering. The coordinates of over 4,000 atoms are provided in the crystal structure of the antibody–antigen complex. Although entire protein–protein systems have been simulated through Brownian dynamics (Northrup et al., 1988; Nambi et al., 1991), and work is underway toward that end to obtain reliable absolute reaction rates for the entire antibody–antigen complex, it is not possible to investigate such a wide variety of mutants with presently available computer resources. We therefore consider a model system that is simple enough to allow for extensive investigation of different mutations, yet still contains the essential aspects of the molecular recognition.

The antibody is represented by one of its Fv fragments (residues H1–116 from the heavy chain and L1–105 of the light chain), with coordinates taken from the crystal structure data (Kinemage 1). This portion, which forms an independent domain composed of a light chain and a heavy chain, encompasses the entire active site of the protein and moreover contains all of the complementarity-determining regions of the antibody, which are responsible for its specificity (Kinemage 2). Although it is the case that the rest of the Fab segment of the molecule given in the crystal structure contains charged residues that can affect the electrostatic steering, these are distant from the binding site, and it will be shown that they contribute to

the physics in a predictable way. Experimental results also indicate that the association behavior of Fv fragments from the monoclonal antibody D1.3 with the lysozyme is extremely similar to that of the entire Fab portion (Poljak, pers. comm.). The electrostatic potential is generated by assigning appropriate point charges to the N-termini and each of the charged residues. The fragment thus has a total of 38 charge sites and is electrically neutral. In a similar study on the diffusion of oxygen ions toward superoxide dismutase (Sines et al., 1990), it has been shown that this prescription of charge assignment gave similar results as more sophisticated models in which each atom was assigned a fractional charge. The time required to calculate the electrostatic field increases by a factor of about three to five depending on the ionic strength if an all-atom model is used for the charge distribution, with most of the extra time spent in generating the boundary conditions, as described below.

From an examination of the crystal structure of the complex (Sheriff et al., 1987), it is seen that the contact surface of the lysozyme with the Fv fragment is relatively flat with the exception of the two side chains from Arg-45 and Arg-68, which fit in the binding groove of the antibody (Kinemage 2). The lysozyme itself is represented as a spherical positive charge that simulates the effect of these residues as they form salt bridges with the antibody. This simple picture of the antigen makes it feasible to test a large number of antibody mutants, providing a more complete global picture of electrostatic steering. The lysozyme, which acts a test charge in the external field of the antibody, is assigned an exclusion radius of 4 Å. For larger values of this parameter, the sphere has difficulty in getting into the binding groove of the antibody, whereas for smaller values, it tends to "stick" near regions of large opposite charge, greatly increasing the time required to run a set of trajectories. This phenomenon has also been observed in diffusional motion simulations by Allison et al. (1988). We have run simulations with the lysozyme charge set at +1e, +3e, and +5e. With the charge set at larger magnitudes, the lysozyme would again stick to portions of the Fv fragment.

The interior of the protein, from which ions are excluded, is assumed to have a dielectric constant of 2. The electrolyte is taken to have a dielectric constant of 78 and an ionic concentration varying from 5 to 350 mM. All calculations are performed for a temperature of 300 K. The relative diffusion constant is determined within hydrodynamic theory (slip boundary conditions) by assigning hydrodynamic radii of 30 Å to the antibody and 4 Å to the sphere and is found to be 0.0695 $Å^2$/ps. The reaction condition is defined in terms of the salt links that are formed in the complex (Kinemages 1, 2), and we will assume that a reaction occurs when the center of the lysozyme is within 8.5 Å of the center of the CD atom in Glu-H50. At this distance, the model lysozyme is in van der Waals' contact with the OE atom of the Glu-H50. The other residue involved in forming salt links with the lysozyme, Glu-H35, is not included in the reaction condition because it lies deeper within the binding groove, and hence the sphere will always encounter Glu-H50 first. This criterion is accurate to the extent that it mimics the contact occurring at the residue level and is representative of the electrostatic steering of the full lysozyme. The Glu-H50 residue is also conserved in a large number of Fv fragments (Kabat et al., 1991), indicating that this study may be relevant for a variety of antibody–antigen systems.

The present system, as already noted, provides a practical means for performing a comprehensive study of the importance of various antibody residues in the efficient electrostatic steering of the antigen. The model parameters involving excluded volumes, diffusion constants, and reaction criteria have been adjusted to yield appreciable reaction probabilities, therefore decreasing the number of trajectories that must be run in order to achieve reliable statistics. Thus, the absolute reaction rates that we obtain are much higher than those expected for diffusion-controlled protein–protein reactions, being on the order of 10^{8-9} M^{-1} s^{-1} for physiological ionic strengths. Although these rates could be lowered by changing the above model parameters, it is our purpose to assess the degree of change in reaction rate induced by a given mutation. For this reason, the emphasis in this study will be on *relative* rates of reaction for mutants in comparison with wild-type diffusion.

Wild-type diffusion

Both aspects of the calculation, the electrostatics portion and the Brownian motion, were performed with the program UHBD, developed by Davis et al. (1990). Shown in Figure 1 is a visual representation of the energy of the ly-

Fig. 1. Binding of the lysozyme within the electrostatic field of the Fv fragment. The red areas indicate attraction of the positively charged lysozyme, and the blue areas show repulsion.

sozyme within the electrostatic field of the wild-type Fv fragment. The reaction site is located within the attractive bulge at the center of the picture, demonstrative of favorable electrostatic steering. This area is flanked by two lobes that indicate repulsive interactions. We have observed that the relative sizes of the bulge and lobes are noticeably affected by point mutations. As an example, Figure 2A gives the electrostatic energy when the negative charge of the Glu-H50 is reversed. For comparison, the wild-type potential for the same molecular orientation is shown in Figure 2B. The field is calculated at an ionic concentration of 150 mM. Drastic changes in the vicinity of the binding site are observed, while the field at more remote points remains largely unaltered. The binding pocket, which is near the bottom of the central red region as seen in Figure 1, is less attractive, indicative of a detrimental effect on electrostatic steering.

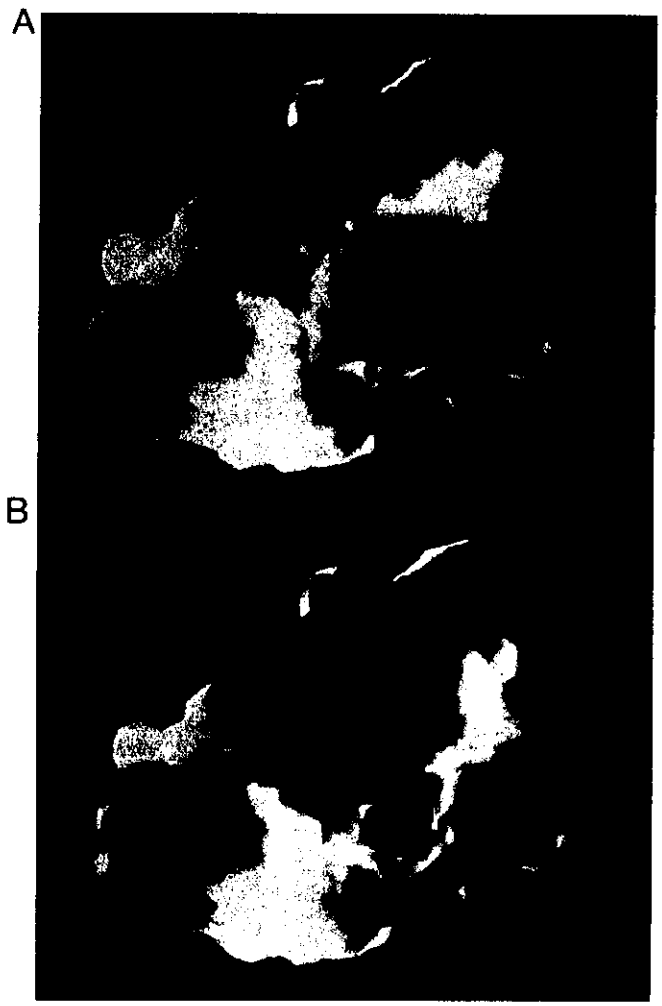

Fig. 2. Visual representation of the electrostatic potential of the Fv fragment when the charge on Glu-H50 is reversed (**A**) and unchanged (**B**). The field is calculated for an ionic strength of 150 mM. The red areas indicate attraction of the lysozyme, and the blue areas show repulsion. The binding region is located at the bottom of the central red area of B, as can be seen by comparing the field map with that of Figure 1.

A histogram of the position of the diffusing sphere can be compiled during the evolution of the trajectories, which represents, in effect, a numerical solution of the Smoluchowski equation (see, for example, the review by Calef & Deutch [1983])

$$kT\nabla^2 C + \nabla C \cdot \nabla U + C\nabla^2 U = 0 \qquad (5)$$

for the steady-state distribution C of a particle undergoing Brownian motion in the presence of an external force-field U. In Figure 3A a slice through three-dimensional space of the logarithm of the distribution for diffusion under the influence of the wild-type potential is displayed. For comparison, a diagram of the negatively charged residues of the antibody fragment in the same orientation as in Figure 3A is shown in Figure 3B. The picture indicates that the diffusing particle tends to random walk until it is "captured" by a region of attractive potential, rather than follow a directed path to the binding site. The concentration clearly shows a maximum within the groove containing the residue Glu-H50. However, also visible is a secondary maximum near the negative-charge cluster defined by the residues L17, L78, L80, L81, and L103 of the antibody (Kinemage 1). This raises the question of whether such areas can act as decoy sites, inhibiting the molecular recognition of an antigen. A weaker hot-spot is also discernible, signaling the presence of local attraction caused by another group of three residues. The noisy character of the plot at larger distances is due to the statistical nature of the simulation.

In order to assess the effect of the total charge of the lysozyme on the molecular recognition between antibody and antigen, we ran simulations for the diffusion of three different charges in the field of the wild-type Fv fragment. The reaction rates relative to that for an uncharged lysozyme are plotted in Figure 4. The enhancement is as much as 65-fold, depending on the values of the charge and ionic strength. The reaction rates give a clear indication of the importance of electrostatic steering in molecular recognition by the antibody, despite the fact that its net charge is zero. As expected, the absolute rates decrease with decreasing charge and increasing ionic strength, although the rate of change with respect to salt concentration is not identical for all values of the charge. As noted by Sines et al. (1990) in a previous study on biomolecular diffusion, this suggests that forces of different length scales contribute to the overall steering effect.

Point mutations of the Fv fragment

As we have adopted a more sophisticated model of the antibody than for the lysozyme it is possible to perform a more thorough study of the effects of site-directed mutations in the Fv fragment on the reaction rate. In order

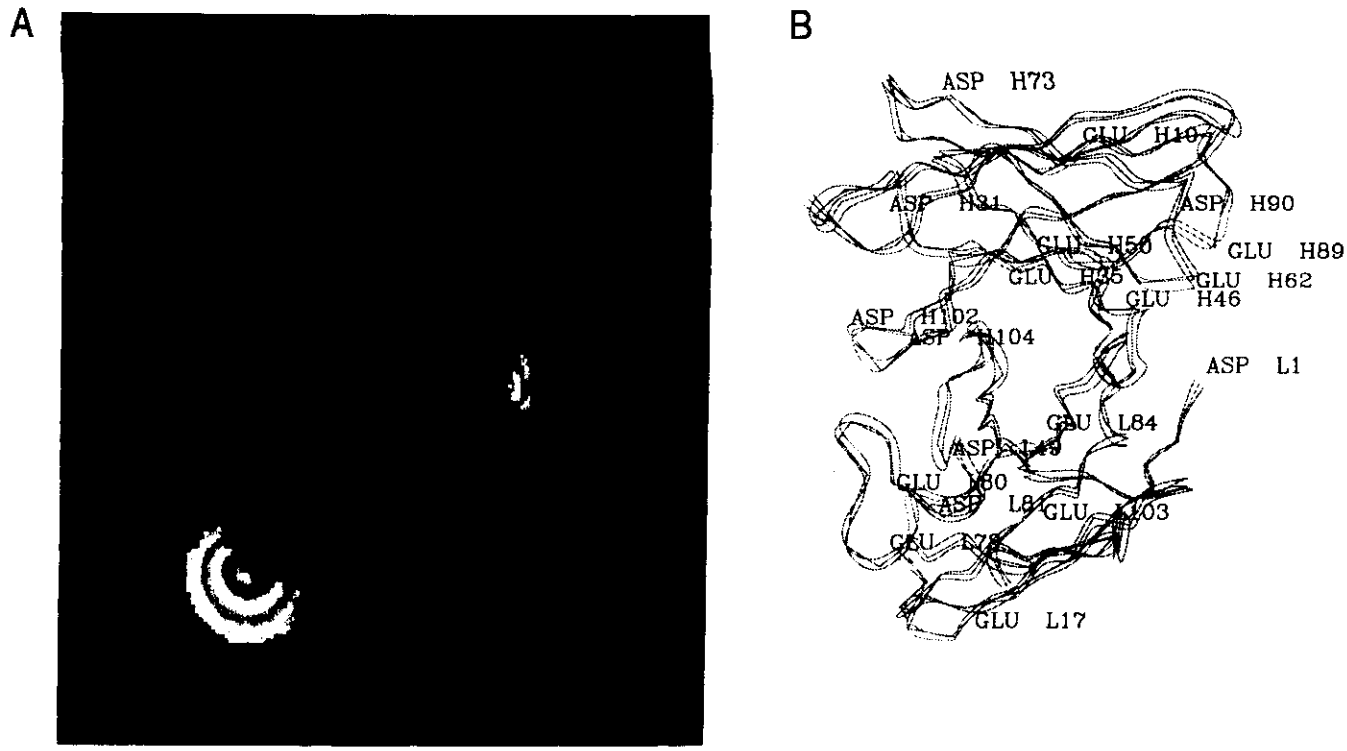

Fig. 3. A: The banded gray-scale representation of the logarithm of the steady-state concentration of the lysozyme around the Fv fragment. The antibody is oriented as in **B**, which also gives the locations of the Glu and Asp residues. The central void is the excluded volume. The white sliver near the center of the picture is the maximum within the binding groove of the antibody. The large white area in the lower left-hand corner is due to local attraction by the charged-residue cluster L17, L78, L80, L81, and L103, a region discernible as a red spot in the electrostatic map of Figure 1.

to obtain a global picture of the fields relevant to molecular recognition, each of the residues Asp, Glu, Asn, and Gln were systematically "mutated" to Asn, Gln, Asp, and Glu, respectively. The location of these residues on an α-carbon trace of the Fv fragment is shown in Figure 5A and B and Kinemage 1. These mutants were constructed by either adding or subtracting a charge from the appropriate site. From the figures, one can see that the above residues are distributed roughly uniformly over the protein, and proceeding in this manner allows us to look at mutations that both constructively and adversely affect the reaction rate. More importantly, our results can be used to predict the particular mutations from the above class that should have the greatest impact on the reaction rate in laboratory experiments. In the results to be displayed below, the lysozyme charge is fixed at +5e, although we have also done simulations with the charge set at +3e and +1e. In each case, the mutants that exert the largest effect during the diffusional motion are the same, and the reason why the +5e results are discussed is that the reaction probability is greater, hence leading to superior statistics.

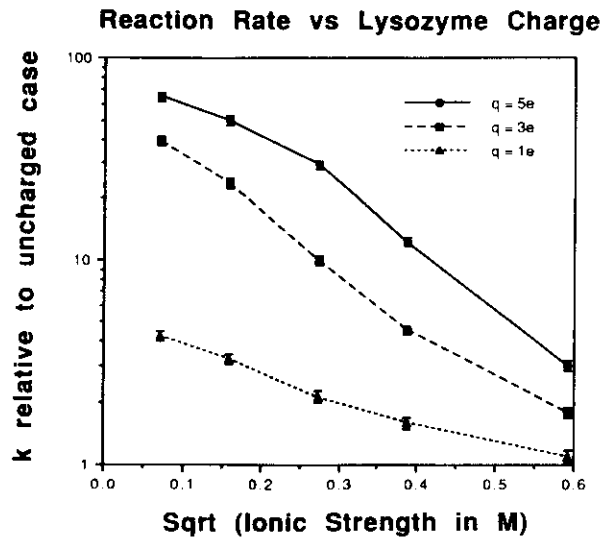

Fig. 4. Reaction rate for the lysozyme with the wild-type antibody as a function of enzyme charge. Rates are given relative to the case where the lysozyme charge is equal to zero.

The primary factor that determines the effect of a given mutation is its distance from the reaction site, with those within about 20 Å having the greatest effect. (This relationship between distance and effect on molecular recognition [Sines et al., 1990; Getzoff et al., 1992] was also found in superoxide dismutase.) Outside of this radius, the reaction rates relative to the wild type are qualitatively similar to those predicted by the Smoluchowski model

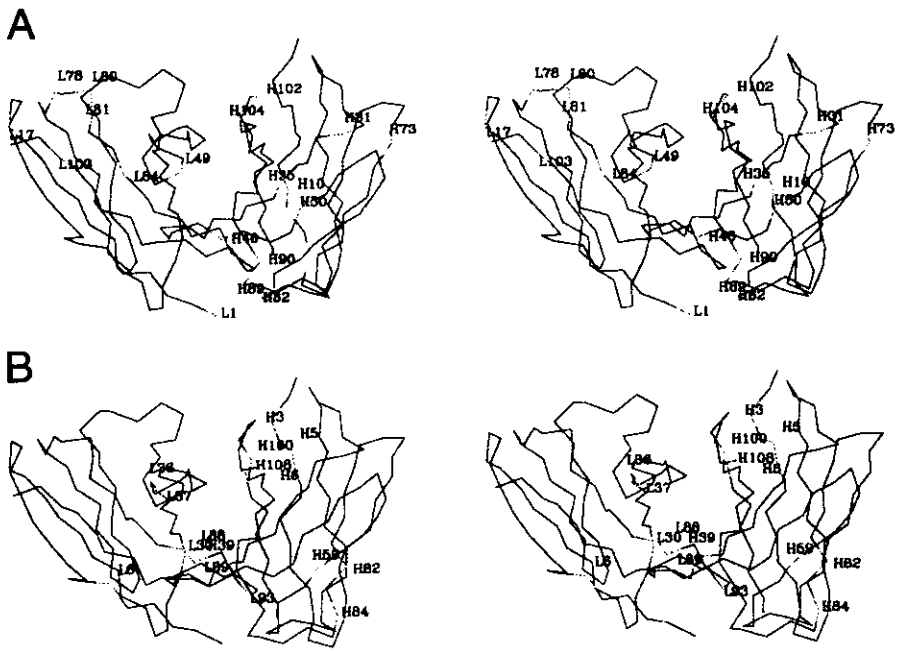

Fig. 5. Stereographic views depicting locations of all of the residues at which point mutations were made. **A:** The Glu and Asp residues, from which a negative charge was subtracted. **B:** The Gln and Asn residues, to which negative charges were added.

(Northrup & Hynes, 1979) for the mutual diffusion of two uniformly charged spheres similar in size to our proteins. In Tables 1 and 2, the reaction rates relative to the wild-type case at 150 mM ionic strength are listed for all of the point mutants that we have investigated. Table 1 depicts the negatively charged mutants that tend to increase the reaction rate over the wild-type rates while Table 2 gives the positively charged mutants that result in lower reaction rates. The relationship between distance and relative rate can clearly be seen in the tables. However, we note that distance from the binding site does not by itself determine the effectiveness of a given mutation. Evidently, electrostatic screening of charge sites by both the protein and the electrolyte also play a role in the molecular recognition process.

Table 1. *Reaction rates for negatively charged mutants*[a]

Mutant	Distance (Å)	Rate
H59:Asn → Asp	5.12	1.91 ± 0.07
L88:Gln → Glu	10.3	1.51 ± 0.06
H100:Asn → Asp	10.9	1.99 ± 0.07
L93:Asn → Asp	11.1	1.22 ± 0.05
L89:Gln → Glu	12.9	1.37 ± 0.06
L30:Asn → Asp	15.5	1.60 ± 0.06
H3:Gln → Glu	18.4	0.94 ± 0.04
H82:Gln → Glu	18.8	1.01 ± 0.05
H84:Asn → Asp	19.0	1.09 ± 0.05
H39:Gln → Glu	19.2	1.10 ± 0.05
H108:Gln → Glu	20.1	1.01 ± 0.05
L37:Gln → Glu	20.2	1.02 ± 0.05
H6:Gln → Glu	21.3	1.01 ± 0.05
H5:Gln → Glu	22.3	1.02 ± 0.05
L36:Gln → Glu	23.6	0.99 ± 0.05

[a] Effects of mutations in which a negative charge is added to the antibody. Distances are from the charge site to the δ-carbon of the Glu-H50 reaction site. Rates given relative to wild-type rates at 150 mM and the errors are statistical.

Table 2. *Reaction rates for positively charged mutants*[a]

Mutant	Distance (Å)	Rate
H50:Glu → Gln	0.00	0.19 ± 0.02
H35:Glu → Gln	4.66	0.34 ± 0.03
H104:Asp → Asn	14.1	0.80 ± 0.04
H31:Asp → Asn	14.1	0.61 ± 0.04
H62:Glu → Gln	14.6	0.93 ± 0.04
H46:Glu → Gln	14.7	1.01 ± 0.05
L49:Asp → Asn	15.5	0.48 ± 0.03
L1:Asp → Asn	16.2	0.88 ± 0.04
H102:Asp → Asn	16.8	0.60 ± 0.04
H73:Asp → Asn	19.7	0.98 ± 0.05
H90:Asp → Asn	20.3	0.96 ± 0.04
H89:Glu → Gln	22.8	0.94 ± 0.04
L84:Glu → Gln	23.5	1.03 ± 0.05
H10:Glu → Gln	23.6	1.03 ± 0.05
L81:Asp → Asn	29.8	0.99 ± 0.05
L80:Glu → Gln	32.1	0.96 ± 0.04
L103:Glu → Gln	33.1	1.00 ± 0.05
L78:Glu → Gln	33.5	1.04 ± 0.05
L17:Glu → Gln	37.6	1.07 ± 0.05

[a] Effects of mutations in which a negative charge is removed from the antibody. Distances are from the charge site to the δ-carbon of the Glu-H50 reaction site. Rates given relative to wild-type rates at 150 mM and the errors are statistical.

The mutations that give a relative rate close to one at physiological ionic strength in Tables 1 and 2 are those that tend to exhibit Smoluchowski properties. This can best be appreciated by studying the relative rates as a function of salt concentration. Two examples, the mutations of Gln-H6 and Glu-L78, are graphed in Figure 6A and B, respectively. For comparison, the relative rates of the Smoluchowski model in which a neutral sphere is increased or decreased by one charge unit are displayed. For the purposes of the plots, the radii of the two spheres were assumed to be 30 Å and 4 Å. It is clear that a better "fit" could be obtained by adjusting the sphere radii. The purpose of the figures, though, is merely to illustrate the qualitative effects of the mutations; they are small at 5 mM (roughly 20% for a lysozyme charge of +5e) and decrease to virtually zero at physiological concentrations.

Within the group that is not described by Smoluchowski theory, the relative reaction rates tend to be larger and exhibit somewhat "nonintuitive" behavior in that they are often larger for higher ionic strengths and lower charges. An explanation of this phenomenon might be as follows. The total potential of the mutated antibody is given by $\phi + \delta\phi$, where ϕ is the wild-type potential, and $\delta\phi$ is the change due to the mutation. (For a point mutation, $\delta\phi$ is simply a monopole field, modified by screening effects.) If ϕ is already an efficient steering field, then a beneficial mutation as represented by $\delta\phi$ will have a small effect. However, if the steering effects of ϕ are relatively weak, then $\delta\phi$ can act as a "beacon" field, giving a greater enhancement of the rate over the wild type. For detrimental mutations, the same argument can be used, reversing the roles of mutant and wild type.

For negatively charged mutants, the largest effects were found at the Asn residues L30, H100, and H59, whose charge sites were 16.7, 10.9, and 5.1 Å, respectively, from the reaction site (Kinemage 1). In some cases, the rate is increased by about a factor of two over the wild-type simulations. The reaction rates relative to wild type for the above mutants are plotted in Figure 7, and it can be seen that the rates are identical for lower salt concentration, indicative of the dominance of long-range effects, and diverge from each other as the ionic strength increases. Interestingly, the largest effects are observed near physiological conditions. Also notable is the change compared to wild type for the Asn-H59 mutation at the highest ionic strength, 350 mM. This phenomenon persists for a lyso-

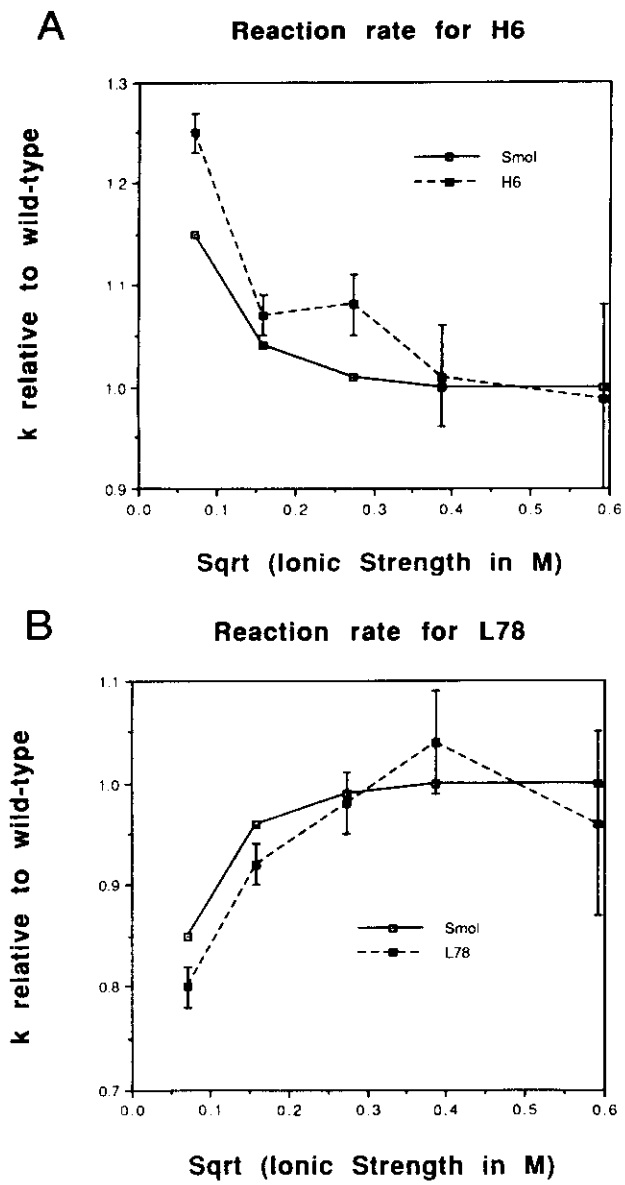

Fig. 6. Reaction rates relative to wild-type for the lysozyme with the Fv mutants Gln-H6 (**A**) and Glu-L78 (**B**). For comparison, the rates as obtained from a Smoluchowski model are also plotted.

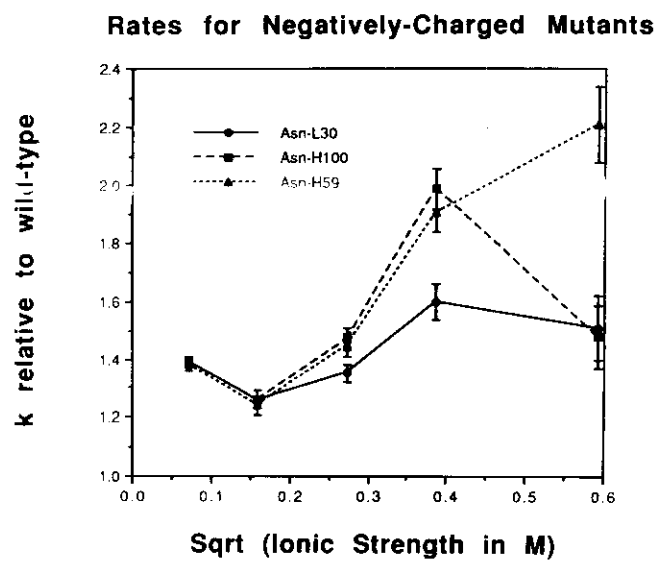

Fig. 7. Reaction rates relative to wild-type for the lysozyme with the Fv mutants obtained by adding a negative charge to Asn-L30, Asn-H59, and Asn-H100.

zyme charge of +3e and is illustrative of the sometimes nonintuitive behavior of the relative rates as discussed above. As stated above, proximity to the reaction site only partly determines the steering effect of a given residue. As an example, addition of a charge at the Asn-L93 residue, which is only 11.1 Å from the Glu-H50 site, yields a smaller relative rate than any of the above changes, although it still exhibits non-Smoluchowskian behavior. The reaction rates for this mutation and that representing the addition of a charge at the Gln-L88 site are shown in Figure 8.

In mutants that carry a net positive charge, the largest effect on reaction rate occurs, as one might expect, when the Glu-H50 residue is neutralized with as much as a 10-fold decrease compared to wild-type rates occurring. Among other mutations, those that give the largest effects are Glu-H35 and Asp-H31 (Kinemage 1). In the full antibody–antigen system, some of the above residues are in contact with the lysozyme, and in such cases the above simulations should be augmented by free-energy calculations in order to calculate the experimental reaction rate. However, this result indicates the importance of steering effects, which should be included in any theoretical prediction of reaction rates. The rates that have been obtained for some of the above mutants are displayed in Figure 9. The ionic strength dependence of the relative rates tends to be smoother than for the negative mutants, except at higher salt concentration where the relative rates are approaching unity. In Figure 10 are plotted relative rates for mutations corresponding to the Asp-L49 and Asp-H104 sites. Again, the relative rates approach one at the highest ionic strengths, although not as quickly as would be expected within the Smoluchowski model.

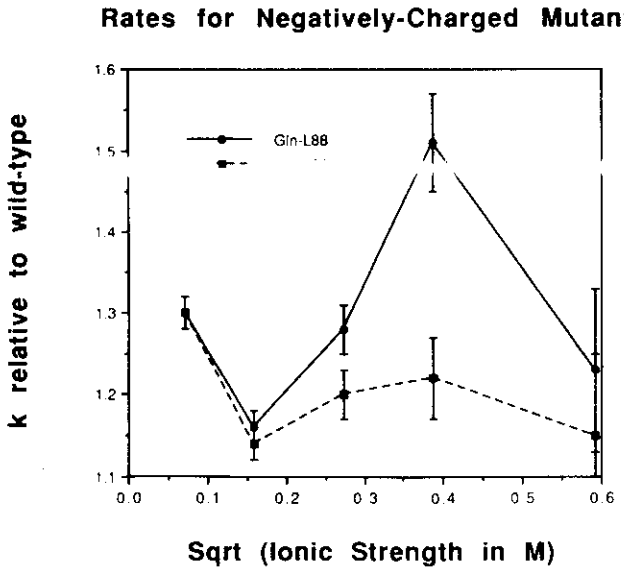

Fig. 8. Reaction rates relative to wild type for the lysozyme with the Fv mutants obtained by adding a negative charge to Gln-L88 and Gln-L93.

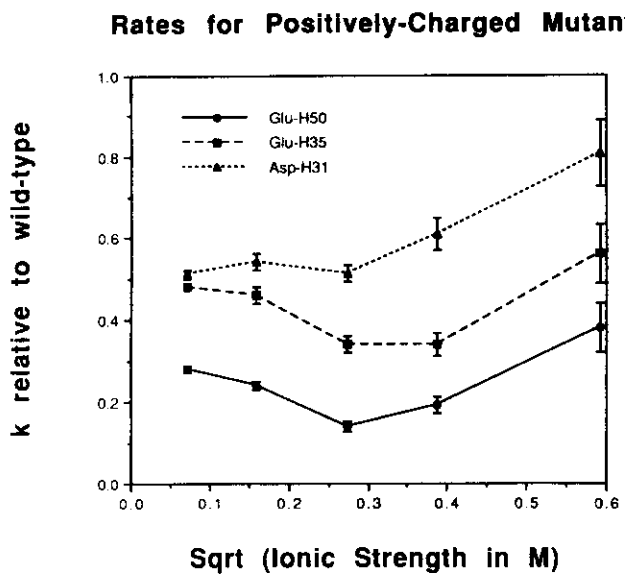

Fig. 9. Reaction rates relative to wild type for the lysozyme with the Fv mutants obtained by removing a negative charge from Asp-H31, Glu-H35, and Glu-H50.

Double mutations

In addition to the more than 30 point mutations discussed in the previous section, we have also considered a limited number of antibody mutants in which two charge sites were altered. In several cases the results of the modifications are well predicted by the multiplicative rule deduced by Sines et al. (1992). In other words, the relative rate for the double mutation is given by the product of the corresponding single-mutation relative rates. In fact, in each instance where at least one of the mutations is of the Smoluchowski-type, the results agree, within statistical error, with the multiplicative model. However, for double mutations that involve two changes of the residues found to be important above in the electrostatic steering, deviations from multiplicative rates are observed. This nonmultiplicative behavior for residues near the active site is also found in the investigation of Sines et al. (1992).

For all of the mutants that we have tested, the one that yields the largest enhancement over the wild-type reaction rate is the double mutation in which charges are placed at the Asn-H59 and Asn-H100 sites. Although the relative rates are not quite as large as those predicted by the multiplicative model, they still represent a nearly threefold increase over the wild-type rates at higher ionic strengths. The results for this mutant are given in Figure 11. For contrast, rates for the double mutant involving the Asn-H100 and Gln-H108 residues are also plotted in the figure. The Gln-H108 mutation alone gives Smoluchowski-like results, and it can be noted that there is very little enhancement of the single Asn-H100 rate at the high ionic strengths, as predicted by the multiplicative model.

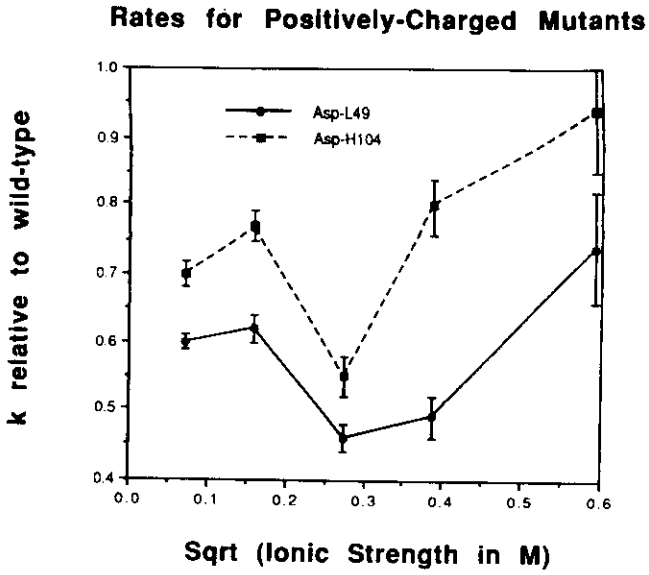

Fig. 10. Reaction rates relative to wild type for the lysozyme with the Fv mutants obtained by removing a negative charge from Asp-L49 and Asp-H104.

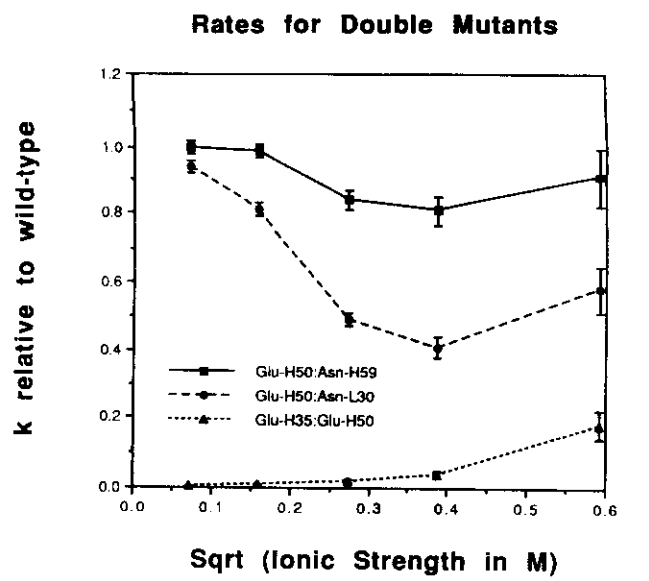

Fig. 12. Reaction rates relative to wild type for the lysozyme with the Fv mutants obtained by modifying the residue pairs Asn-H59:Glu-H50 and Asn-L30:Glu-H5.

We have also run simulations for several double mutations, displayed in Figure 12, involving the neutralization of the crucial Glu-H50 residue. When this is done in conjunction with the addition of a negative charge at the Asn-H59 site, it is seen that the extra charge acts almost as a "surrogate" for recognition of the lysozyme, since the reaction rate is never less than 80% of the wild-type value. A similar kind of mutant, with the Asn-L30 residue replacing the Asn-H59 residue, is less efficient at electrostatic steering, although it still produces increased reaction rates over the single Glu-H50 mutant. Most interesting of the double mutants that we have observed is the one created by removing the charges from both Glu-H35 and Glu-H50, which for all ionic strengths yields reaction rates that are lower than in the uncharged lysozyme case. Therefore, this mutant actively directs the antigen *away* from the binding site. This is also the only case where the absolute rates do not decrease monotonically with decreasing charge and increasing ionic concentration. For the lower ionic strengths, the reaction rate is reduced by two to three orders of magnitude. It is well known, of course, that these residues are important in the binding of the lysozyme because they form part of the salt bridges associated with the complex; however, these simulations suggest that these residues are also very important in the diffusion-controlled step of the reaction.

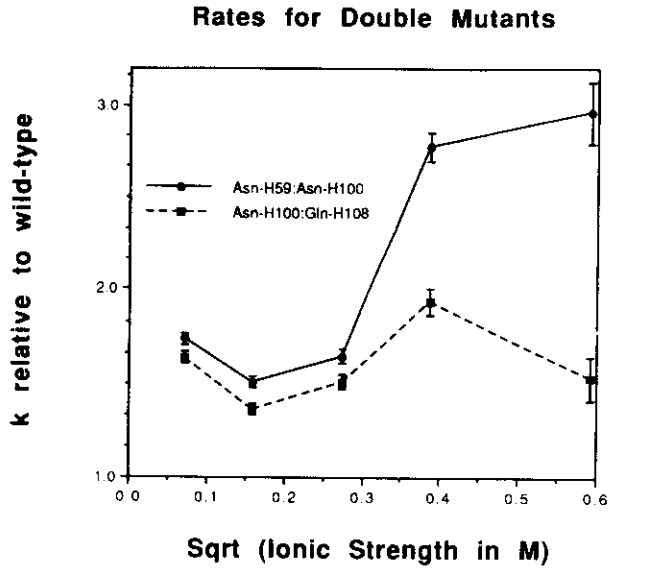

Fig. 11. Reaction rates relative to wild type for the lysozyme with the Fv mutants obtained by modifying the residue pairs Asn-H59:Asn-H100 and Asn-H100:Gln-H108.

We have also employed double mutations to more closely examine the large "hot-spot" in the lysozyme concentration, visible in Figure 3. It is apparent there that the diffusing sphere tends to spend a comparatively large time near a cluster a five negatively charged residues on the antibody, and it was speculated that this might act as a decoy site. However, single point mutations of these residues gave results that were quite consistent with Smoluchowski-like behavior. We also attempted two double mutations in which one of these residues was neutralized in concert with the addition of a charge to a distant neutral residue. One of these two mutants yielded mildly enhanced reaction rates at low ionic strengths with the effect disappearing at physiological strength. This slight change

is most likely due to the subtraction of a dipole field that points away from the reaction site, as it has been shown in a model system that such an arrangement leads to unfavorable electrostatic steering (Northrup et al., 1986). Nevertheless, it is still possible that decoy sites might be important in other antibodies or receptor molecules.

Other mutants

The fact that only mutations within a certain radius of the binding site have a drastic effect on the reaction rate suggests that there exists a "minimal set" of charges that reproduces the electrostatic steering present in the system. In fact, if all charges, positive and negative, more than 20.3 Å distant from the Glu-H50 site are turned off, the result is a slight (from 0 to 20%) enhancement of the native reaction rate at most ionic strengths and lysozyme charges. This reduced set consists of only 20 of the 38 charges on the full Fv fragment. As the radius of the exclusion sphere is increased to 28 Å, encompassing 28 charges of the protein, the reaction rates become very close to the full-protein values. We have computed multipole moments for the two sets of charges described above and compared them with those of the full set, but no similarities were found. This suggests that the key component in molecular recognition is the local character of the field around the reaction site, rather than any global properties of the charge distribution. (We note, however, that the total charge on the antibody still exerts a long-range influence as evidenced by the Smoluchowski-like behavior of distant mutations.) We also note that exclusion spheres with radii less than 20 Å tended to give reduced reaction rates. For example, just including the four closest charges to the binding site (Glu-H35, Glu-H50, Arg-L45, and Arg-L92) yielded reaction rates that were lower by an order of magnitude from those for the wild-type Fv fragment.

As a final simulation, we consider the above-mentioned mutation found in the quail lysozyme in which Arg-68 is replaced by a Lys residue (Smith-Gill et al., 1982). As noted earlier, this change, which shortens the side chain, increases the distance of the positive charge from the negatively charged glutamate residues with which it forms salt links. Because of our simplified scheme for the lysozyme, we have instead performed a similar alteration by moving the negative charge on Glu-H50 from the δ-carbon to the γ-carbon. This decreases the length of the negatively charged side chain from the antibody and mimics a Glu to Asp mutation. For a lysozyme of charge +5e, this gave identical rates to the wild type at 5 mM, but at higher strengths the relative rates decreased monotonically to a value of 0.75 at physiological salt concentration. This behavior is qualitatively similar to that found in the double mutation involving Glu-H50 and Asn-H59, although in the present instance there is a larger adverse effect on the rate. A similar mutation, in which the charge on the Glu-H35 residue is moved, produced a much smaller effect. The relative rates for both of these cases are displayed in Figure 13. Although the results indicate that these mutations can have some effect on electrostatic steering, they also point to the need for free-energy simulations in order to fully understand the large effects associated with them.

Discussion

In this study, we have demonstrated the viability of applying currently available computational methods to the problem of immune recognition. By employing a simplified model for a well-characterized antibody–lysozyme complex, we have been able to calculate relative reaction rates for a wide variety of antibody mutants. This approach has allowed us to map the effect of a given mutation based on its location on the antibody. The charges that are most important in the molecular recognition of lysozyme by HyHEL-5 are in general those closest to the binding site, which has been defined in terms of a residue that is conserved in other antibodies. Effects arising from the mutation of more distant residues are qualitatively described by the Smoluchowski model. As noted above, these studies should be supplemented with calculations such as free-energy simulations in order to fully account for short-range forces and structural effects. In turn though, because the residues most significant in binding interactions between two proteins are also often likely to be important in electrostatic steering, such considerations should be included in any molecular dynamics study.

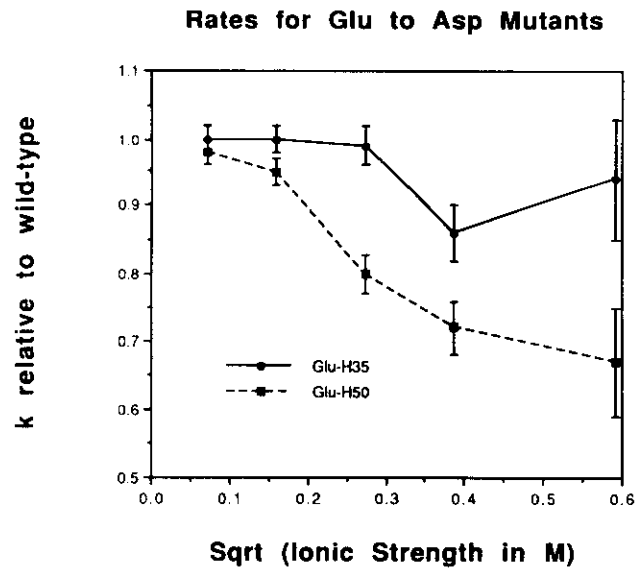

Fig. 13. Reaction rates relative to wild type for the lysozyme with the Fv mutants obtained by moving the charges on the Glu-H35 and Glu-H50, representing Glu to Asp mutations.

We are currently planning, with the help of parallel computers, to implement a more detailed representation of the antigen-antibody system, including a model for the lysozyme that would include orientational effects. In this way, the absolute rate constants that would be obtained from the simulations could be directly compared with laboratory results. Once this has been achieved it should be feasible to utilize the X-ray crystal structures of the other two monoclonal antibodies that have been complexed with lysozyme in order to make comparative investigations. We are also investigating multilevel methods (Holst & Saied, 1993) as a means of solving the full nonlinear Poisson-Boltzmann equation (Holst et al., in prep.). Work is additionally under way to perform both molecular dynamics studies and electrostatic binding calculations of the wild-type HyHEL-5-lysozyme system and various mutants. It appears that Brownian dynamics studies of molecular recognition, in concert with free-energy simulations, and along with information obtained from crystallographic and site-directed mutagenesis experiments can be a powerful tool for providing insight into the rich variety of immune response.

Materials and methods

Electrostatic calculations

The linearized Poisson-Boltzmann equation was solved by discretizing it on a 120^3 grid with 1 Å spacing. For the wild-type case and several mutants, trajectories were run with various grid volumes and spacings to ensure that the above choices yield accurate results. For all mutants, the center of the mesh was placed at the point where the diagonal moments of the quadrupole tensor (Buckingham's definition) vanish for the wild-type case. The atomic radii are taken from the OPLS values (Jorgensen & Tirado-Rives, 1988). In the residue-based charge model, the atomic charge sites are Asp-CG, Glu-CD, Lys-NZ, and Arg-CZ. All histidine residues are assumed to be neutral. The Fv fragment contains two N-termini that are assigned positive charges. At the outer edges of the grid, the boundary conditions were determined by assuming that each charge contributes to the potential as if it were an independent Debye-Hückel sphere of radius 2 Å. It was found that this prescription yielded better convergence for the potential as a function of grid volume than one in which the entire protein was assumed to be a Debye-Hückel sphere. These computations were run on a Cray Y-MP. The UHBD program proved to be highly vectorizable for this task and less than 5 CPU min were required to generate each solution grid.

Diffusional motion

Each trajectory is initiated by placing the lysozyme on a random point of an inner sphere centered on the antibody and is continued until either the reaction condition is satisfied or the diffusing particle crosses the surface of an outer sphere. Throughout the trajectory, the antibody is held rigid and fixed in space. When the lysozyme was sufficiently distant from the Fv fragment that it was beyond the electrostatic grid, an extrapolation of the boundary conditions described above was used to determine the force. As described in the text, the experimentally measurable reaction rate is obtained using the reaction probability and the analytically calculated rates for diffusion to the inner and outer sphere. The radius of the inner sphere is set at 65 Å, and the radius of the outer sphere is taken to be 500 Å. These parameters are determined by gradually increasing each of them until a stable result for the reaction rate is obtained. A variable time step is used depending on the distance of the sphere from the antibody with a minimum value of 10 ps. If a time step results in a collision of the sphere with the protein, it is simply repeated using a new random force. A total of 10,000 trajectories were run for each mutant and at each ionic strength. In order to reduce the statistical error in the relative rates, 100,000 trajectories are used with each charge and ionic strength for wild-type diffusion. The trajectories were run on various SGI workstations, and a set of 10,000 required 2-3 CPU hours.

Acknowledgments

We thank D.R. Davies for providing crystal coordinates for the HyHEL-5-lysozyme complex. We are also grateful to J.A. McCammon for releasing a copy of the program UHBD to us. The figures were generated using the program c3d, written by Chris Culberson of Monsanto Research. This work was supported in part by NIH grant RO1 GM46535 (subcontract from Texas A&M) and by a grant from FMC Corporation. We thank the National Center for Supercomputing Applications for providing computational resources.

References

Allison, S.A., Bacquet, R.J., & McCammon, J.A. (1988). Simulation of the diffusion-controlled reaction between superoxide and superoxide dismutase. II. Detailed models. *Biopolymers 27*, 251-269.

Calef, D.F. & Deutch, J.M. (1983). Diffusion-controlled reactions. *Annu. Rev. Phys. Chem. 34*, 493-523.

Davies, D.R., Padlan, E.A., & Sheriff, S. (1990). Antibody-antigen complexes. *Annu. Rev. Biochem. 59*, 439-473.

Davis, M.E., Madura, J.D., Luty, B.A., & McCammon, J.A. (1990). Electrostatics and diffusion of molecules in solution – Simulations with the University of Houston Brownian dynamics program. *Comp. Phys. Commun. 62*, 187-197.

Davis, M.E. & McCammon, J.A. (1989). Solving the finite difference linearized Poisson-Boltzmann equation: A comparison of relaxation and conjugate gradient methods. *J. Comp. Chem. 10*, 386-391.

Ermak, D.L. & McCammon, J.A. (1978). Brownian dynamics with hydrodynamic interactions. *J. Chem. Phys. 69*, 1352-1360.

Getzoff, E.D., Fisher, C.L., Parge, H.E., Viezzoli, M.S., Banci, L., & Hallewell, R.A. (1992). Faster superoxide dismutase mutants designed by enhancing electrostatic steering. *Nature 358*, 347-351.

Gilson, M. & Honig, B. (1987). Calculation of electrostatic potentials in an enzyme active site. *Nature 330*, 84-86.

Holst, M., Kozack, R.E., Saied, F., & Subramaniam, S. (In prep.). Protein electrostatics: Rapid multilevel solution of the full non-linear Poisson-Boltzmann equation.

Holst, M. & Saied, F. (1993). Multigrid solution of the Poisson-Boltzmann equation. *J. Comp. Chem. 14*, 105-113.

Jorgensen, W.L. & Tirado-Rives, J. (1988). The OPLS [optimized potentials for liquid simulations] potential functions for crystals of cyclic peptides and crambin. *J. Am. Chem. Soc. 110*, 1657-1669.

Kabat, E.A., Wu, T.T., Perry, H.M., Gottesman, K.S., & Foeller, C. (1991). *Sequences of Proteins of Immunological Interest*, 5th Ed. National Institutes of Health, U.S. Department of Health and Human Services, U.S. Government Printing Office, Washington, D.C.

Lavoie, T.B., Kam-Morgan, L.N.W., Hartman, A.B., Mallett, C.P., Sheriff, S., Saroff, D.G., Mainhart, C.R., Hamel, P.A., Kirsch, J.F., Wilson, A.C., & Smith-Gill, S.J. (1989). Structure-function relationships in high-affinity antibodies to lysozyme. In *The Immune Response to Structurally Defined Proteins: The Lysozyme Model* (Smith-Gill, S.J. & Sercarz, E.E., Eds.). Adenine Press, New York.

Nambi, P., Wierzbicki, A., & Allison, S.A. (1991). Molecular interaction between bovine pancreatic trypsin inhibitor molecules probed by Brownian dynamics simulation. *J. Phys. Chem. 95*, 9595-9600.

Northrup, S.H., Allison, S.A., & McCammon, J.A. (1984). Brownian dynamics simulation of diffusion-influenced biomolecular reactions. *J. Chem. Phys. 80*, 1517-1524.

Northrup, S.H., Boles, J.O., & Reynolds, J.C.L. (1988). Brownian dynamics of cytochrome *c* and cytochrome *c* peroxidase association. *Science 241*, 67-70.

Northrup, S.H. & Erickson, H.P. (1992). Kinetics of protein-protein association explained by Brownian dynamics computer simulation. *Proc. Natl. Acad. Sci. USA 89*, 3338-3342.

Northrup, S.H. & Hynes, J.T. (1979). Short range caging effects for reactions in solution. I. Reaction rate constants and short range caging picture. *J. Chem. Phys. 71*, 871-883.

Northrup, S.H., Smith, J.D., Boles, J.O., & Reynolds, J.C.L. (1986). The effect of dipole moment on diffusion controlled biomolecular reaction rates. *J. Chem. Phys. 84*, 5536-5544.

Raman, C.S., Jemmerson, R., Nall, B.T., & Allen, M.J. (1992). Diffusion-limited rates for monoclonal antibody binding to cytochrome *c*. *Biochemistry 31*, 10370-10379.

Sheriff, S., Silverton, E.W., Padlan, E.A., Cohen, G.H., Smith-Gill, S.J., Finzel, B.C., & Davies, D.R. (1987). Three-dimensional structure of antibody-antigen complex. *Proc. Natl. Acad. Sci. USA 84*, 8075-8079.

Sines, J.J., Allison, S.A., & McCammon, J.A. (1990). Point-charge distributions and electrostatic steering in enzyme-substrate encounter: Brownian dynamics of modified copper-zinc superoxide dismutases. *Biochemistry 29*, 9403-9412.

Sines, J.J., McCammon, J.A., & Allison, S.A. (1992). Kinetic effects of multiple charge modifications in enzyme-substrate reactions: Brownian dynamics simulations of Cu,Zn superoxide dismutase. *J. Comp. Chem. 13*, 66-69.

Smith-Gill, S.J., Wilson, A.C., Potter, M., Prager, E.M., Feldmann, R.J., & Mainhart, C.R. (1982). Mapping the antigenic epitope for a monoclonal antibody against lysozyme. *J. Immunol. 128*, 314-322.

Numerical Solution of the Nonlinear Poisson–Boltzmann Equation for a Membrane–Electrolyte System

Kimberly E. Forsten,[†] Richard E. Kozack,[‡] Douglas A. Lauffenburger,[†] and Shankar Subramaniam*[,‡]

Department of Chemical Engineering and Center for Biophysics and Computational Biology, Department of Physiology and Biophysics, Beckman Institute for Advanced Science and Technology, National Center for Supercomputing Applications, University of Illinois at Urbana–Champaign, Urbana, Illinois 61801

Received: December 22, 1993; In Final Form: March 21, 1994[•]

Two features that characterize the complex nature of a membrane–electrolyte system are the change in dielectric at the lipid–solvent interface and the periodicity of the charge-embedded membrane. The former can be treated within a continuum model, and the planar nature of the membrane can be accounted for through the enforcement of periodic boundary conditions. Here we describe a numerical technique, based on a finite-difference formulation, for solving the full nonlinear Poisson–Boltzmann equation which incorporates the above features of a membrane–electrolyte system. This method is used to calculate the electrostatic potential for a model membrane containing a rectangular array of charges at a variety of lattice spacings and ionic strengths. At sufficiently large distances from the membrane, the results are in good agreement with the Gouy–Chapman theory, which is based on the assumption of a uniform charge density in an infinite plane. Electrostatic potentials are also obtained in the interior of the membrane for the model system. In addition, this method is used to find the potential for a case where a set of dipoles is embedded in a membrane. This procedure can be applied to the investigation of the electrostatic properties of lipid–bound proteins and in other cases where Gouy–Chapman theory is inadequate.

I. Introduction

The electrostatic potential in the vicinity of the interface between a lipid membrane and an ionic solution has long been of interest in the biological sciences.[1-3] With currently available computer resources, a detailed molecular dynamics simulation of such a system is intractable. One alternative approach, involving techniques from statistical mechanics together with simplified intermolecular interactions, has been pursued in regard to this problem.[4,5] Continuum electrostatics provides yet a simpler framework for modeling the membrane–electrolyte interface and has been remarkably useful for interpreting empirical observations.[3,6] In this method, the potential is obtained from a solution of the Poisson–Boltzmann equation, a three-dimensional nonlinear partial differential equation.

If it is assumed that the charge on the membrane is evenly smeared over an infinite plane, then the Poisson–Boltzmann equation can be solved analytically, an approach known as Gouy–Chapman theory. Although the Gouy–Chapman model has been successful in describing various experimental results,[3,6] questions remain as to its validity, one reason being that the charges on a membrane are discretely, rather than continuously, distributed.[7-9] In addition, the theory predicts the potential to be identically zero when the membrane contains uncharged polar head groups. In this case though, while the average potential in the aqueous phase is zero, the local potential near the head group region is not. Phenomena such as the acid–base properties of interface residues in membrane proteins and the insertion of signal peptides into membranes are strongly influenced by the local electrostatic environment, and hence it is inappropriate to use the Gouy–Chapman model. Furthermore, the assumption of a planar charge density is not likely to be accurate for membrane-bound proteins. Much analytic work has been done in extending the range of the Poisson–Boltzmann treatment to cover more realistic charge distributions.[10-15] These have mostly dealt with the linearized version of the theory, although Sauvé and Ohki[13] have considered an approximate treatment of the full nonlinear equation.

This paper describes and utilizes an alternative method in which a continuum description is adopted, but the full nonlinear Poisson–Boltzmann equation is solved instead by numerical techniques. This is accomplished by recasting the equation on a discrete grid through finite differences, as is often done in studies of protein electrostatics.[16-18] As in Gouy–Chapman theory, the membrane is assumed to be infinite in extent, in this case through the implementation of periodic boundary conditions. Since these calculations do not depend on the assumption of a continuous charge density, the results can be used to test this aspect of the Gouy–Chapman model. Moreover, our method, which does not necessitate a linear approximation, can be used to describe more general situations involving complex membrane charge distributions and membrane-bound proteins. Furthermore, it is sufficiently flexible such that the potential inside the membrane can also be computed.

The structure of the paper as is follows. In section II, the Gouy-Chapman theory is briefly reviewed. This is followed in section III by an exposition of the numerical procedure used to solve the nonlinear Poisson–Boltzmann equation. In section IV, the method is employed to investigate the electrostatic potential due to an infinite array of charges at a variety of lattice spacings and ionic strengths for comparison with Gouy–Chapman theory. In section V, the transmembrane potential is obtained for a model lipid bilayer. The electrostatic properties of a polar, but uncharged, model membrane are also examined. Possible directions for further study are discussed in section VI. Finally, a summary of the results is presented in section VII.

II. Gouy–Chapman Theory

Gouy–Chapman theory is based on a continuum model for the membrane–electrolyte system.[19] The solvent is assumed to be a dielectric medium containing an ionic charge density which is given by a Boltzmann distribution. For the sake of definiteness, the rest of the paper will be confined to the case of a 1:1 electrolyte, although both the Gouy–Chapman model and the numerical approach described below can easily be modified to describe any type of ionic solution. For example, an extension of the Gouy–Chapman theory to the case of mixed electrolytes has been discussed by Grahame.[20] With this restriction in mind, the full

* To whom correspondence should be addressed.
† Department of Chemical Engineering.
‡ Center for Biophysics and Computational Biology.
• Abstract published in *Advance ACS Abstracts,* April 15, 1994.

0022-3654/94/2098-5580$04.50/0

nonlinear Poisson–Boltzmann equation is

$$-\nabla\cdot(\epsilon\nabla u) + \epsilon\kappa^2 \sinh u = 4\pi e\rho/kT \qquad (2.1)$$

where ϵ is the dielectric constant, e is the elementary unit of charge, and kT is Boltzmann's constant times the temperature. In the above equation, ρ is the fixed charge density and κ is the inverse Debye–Hückel length which satisfies $\kappa^2 = 8\pi Ie^2/\epsilon kT$, where I is the ionic concentration. A dimensionless potential u related to the true electrostatic potential ϕ by

$$u = e\phi/kT \qquad (2.2)$$

has also been defined.

There are several key assumptions in Gouy–Chapman theory which enable an analytic solution of eq 2.1. One is that the interface between membrane and electrolyte can be described as an infinite plane separating two regions, each with a different dielectric constant. This plane, which defines the surface of the membrane, is postulated to contain a constant charge density σ, with units of charge per area. The potential in the solvent, which is dependent only on the distance z from the membrane surface, can then be shown to be given by

$$u = 4 \tanh^{-1}[\exp(-\kappa z) \tanh(u_0/4)] \qquad (2.3)$$

where u_0, the potential at the dielectric discontinuity, obeys the relation

$$u_0 = 2 \sinh^{-1}\left(\frac{2\pi e\sigma}{\epsilon\kappa kT}\right) \qquad (2.4)$$

In the linearized version of the theory, obtained in the limit that u_0 is much less than one, the potential at the membrane surface is proportional to the charge density and decays exponentially as one moves into the solvent. The validity of the assumptions behind the Gouy–Chapman model, particularly that concerning the use of a constant planar charge density, has been extensively discussed in the literature.[7-9] However, as noted above, the continuum approach has proved successful in describing a number of experiments.[3,6] It therefore seems useful to extend the model in order to describe a wider variety of phenomena by employing numerical algorithms to solve the Poisson–Boltzmann equation for a membrane-like geometry. This is the goal of the present study.

III. Numerical Method

Numerical solutions of the Poisson–Boltzmann equation have been previously utilized for research in protein electrostatics.[17,18] A computational study of eq 2.1 has also been performed, under the assumption of cylindrical symmetry, by Cai and Jordan[21] to model an ion channel embedded in a membrane. Within a first-order finite-differencing scheme, the nonlinear Poisson–Boltzmann equation can be given in terms of quantities defined at a set of discrete grid points as[16-18]

$$\begin{aligned} 4\pi q(i,j,k)/h = {} & \epsilon(i-1/2,j,k)[\phi(i,j,k) - \phi(i-1,j,k)] + \\ & \epsilon(i+1/2,j,k)[\phi(i,j,k) - \phi(i+1,j,k)] + \\ & \epsilon(i,j-1/2,k)[\phi(i,j,k) - \phi(i,j-1,k)] + \\ & \epsilon(i,j+1/2,k)[\phi(i,j,k) - \phi(i,j+1,k)] + \\ & \epsilon(i,j,k-1/2)[\phi(i,j,k) - \phi(i,j,k-1)] + \\ & \epsilon(i,j,k+1/2)[\phi(i,j,k) - \phi(i,j,k+1)] + \\ & (kT/e)\epsilon\kappa^2 h^2 \sinh u(i,j,k) \end{aligned} \qquad (3.1)$$

where i, j, and k represent indices in the x, y, and z directions and q is the value of the fixed charge at a grid point. The above equation, which is given in three-dimensional form, contrasts with the Gouy–Chapman model in which the potential is dependent on only one variable. The matrix form of eq 3.1 is

$$f = A\phi + N(\phi) \qquad (3.2)$$

where $N(\phi)$, the nonlinear portion corresponding to the hyperbolic sine term, is diagonal and A is a banded matrix in that only the diagonal elements and those representing the six nearest-neighboring grid points have nonzero values. This equation has previously been solved and applied to soluble proteins by Holst *et al.*[22] using a multigrid-based Newton iterative method. Below we describe a procedure for applying the Poisson–Boltzmann equation to membrane-like geometries which employs an alternative numerical algorithm.

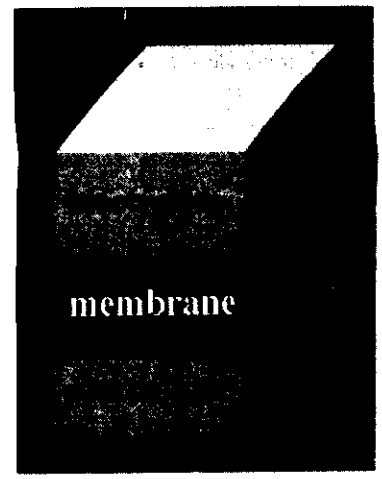

Figure 1. Geometry used for the numerical solution of the Poisson–Boltzmann equation. The potential is set equal to zero at the top and bottom faces of the box, and periodic boundary conditions are enforced at the other faces.

The Poisson–Boltzmann equation is solved within the box, or cell, depicted in Figure 1. The membrane portion, from which ions are excluded, is sandwiched between two regions of electrolyte with identical ionic strengths. As emphasized in the figure, the two electrolyte sections need not be of the same size. Ordinarily, one would have to choose extremely large dimensions along the plane of the membrane in order to accurately simulate a macroscopic lipid–electrolyte system. This is circumvented here through the enforcement of periodic boundary conditions. That is, the potential on each face of the cell that is perpendicular to the membrane surface is set equal to the potential on the opposite face. At the remaining two faces of the box, the potential is taken to be identically zero, since all of the fixed charges are confined near the membrane region.

The discretized form of the Poisson–Boltzmann equation is set up with a suitably modified version of the UHBD program,[23] which was originally designed for protein electrostatics. Because of the imposition of periodic boundary conditions, grid points on opposite ends of the cell are now regarded as nearest neighbors, and it is therefore necessary to account for the alteration of the matrix band structure.[24] The solution of the nonlinear equation (3.1) is obtained in two stages. First, the linearized version of the equation, which follows simply from replacing sinh u by u and, written symbolically as

$$f = \hat{A}\phi_{\text{lin}} \qquad (3.3)$$

is solved using the successive overrelaxation method,[25,26] which has been shown to be an efficient algorithm for solving the Poisson–Boltzmann equation in studies of protein electrostatics.[27] This iterative scheme is given by

$$\phi_{\text{lin}}^{i+1} = \phi_{\text{lin}}^{i} - \omega\hat{L}^{-1}(\hat{A}\phi_{\text{lin}}^{i} - f) \qquad (3.4)$$

where $\hat{L}$ is the lower triangular part of $\hat{A}$ plus its main diagonal and ω is a relaxation parameter chosen to accelerate the

convergence of the algorithm. The linearized potential ϕ_{lin} is then used as an initial guess for an iteration involving the full nonlinear equation. The nonlinear overrelaxation method is employed, which has the form[25,27]

$$\phi^{i+1} = \phi^i - \omega(L + N'(\phi^i))^{-1}(A\phi^i + N(\phi^i) - f) \quad (3.5)$$

where L is the lower triangular part of A plus its diagonal, $N'(\phi^i)$ is the derivative of N evaluated at ϕ^i, and ω again acts as a relaxation parameter. The solution is deemed to be converged when the value of ϕ at each and every grid point changes by less than 1% from one iteration to the next. In our calculations the choice of $\omega = 1.2$ for both eqs 3.4 and 3.5 is sufficient to yield a solution within a reasonable amount of computer time. No attempt has been made to optimize this parameter, and it is possible that with different values of ω much more rapid convergence of the iteration might be achieved.

IV. Electrolyte Potential

In this section, we apply the numerical techniques described above to a model membrane and compare the results with Gouy–Chapman theory. The geometry of Figure 1 is used, with a single charge of $-e$ placed 2 Å below the top of the membrane surface and centered in the box with respect to the other two coordinates. The use of the periodic boundary conditions implies that this setup is equivalent to an infinite rectangular array of discrete charges with a constant lattice spacing. This model system very much resembles one studied by Nelson and McQuarrie[12] in an analytical investigation of the linearized Poisson–Boltzmann equation. The calculations done below are performed with lattice spacings of 8, 16, and 24 Å, giving charge densities of 1/64, 1/256, and 1/576 Å^{-2} in units of e. In the electrolyte, three ionic strengths, 10, 25, and 150 mM, are considered, corresponding to Debye lengths of 30, 19, and 8 Å. Inside the membrane, the ionic strength is zero for all calculations. The dielectric constants are chosen as 2 and 78 for the lipid and solvent, respectively. The spacing between grid points is 1 Å. In all cases, the distance from the bottom of the box to the bottom of the membrane is taken to be 40 Å, and the thickness of the membrane is 40 Å. For an ionic strength of 150 mM, the distance from the top of the membrane to the top of the cell is 60 Å. For the lower ionic strengths this distance is equal to 100 Å, which is necessary to account for the slower decay of the potential due to the larger Debye length.

In this type of calculation, numerical inaccuracies arise from both the discretization of the Poisson–Boltzmann equation and the truncation of the domain of solution to a finite region of space. The truncation errors occur because the boundary condition that ϕ be equal to zero on the top and bottom faces is strictly true only in the limit of infinitely large distance from the membrane. The effect of this approximation has been tested by performing calculations where the top layer of electrolyte is extended by as much as 40 Å and the bottom layer by 20 Å, and in all instances, the potential is unchanged for the results to be presented here (up to 30 Å from the membrane) to within 1%, the convergence criterion of the iterative solution. Another possible specification of this boundary condition, which exploits the analytical Gouy–Chapman solution, is discussed in a later section. The errors due to discretization originate with the finite-difference formulation of the Poisson–Boltzmann equation. The extent of these errors were checked by obtaining solutions with smaller grid spacings, in some cases as low as 0.66 Å. A graph of the numerical solution in the solvent region as a function of grid spacing is shown in Figure 2. The curves for the grid spacings of 0.8 and 1.0 Å are indistinguishable on the scale of the plot. At large distances from the charge, the potential is stable to within less than 3% as a function of grid spacing, both interior and exterior to the membrane. About 2–4 Å from the charge, the instability is slightly larger, being on the order of 5% in both the lipid and electrolyte. At closer distances, the potential is less well determined. This behavior is reflected in the plots of Figure 2. In general, the uncertainties owing to discretization are larger than those arising from truncation. These calculations, though, are still sufficiently accurate such that a meaningful quantitative comparison with Gouy–Chapman theory can be made.

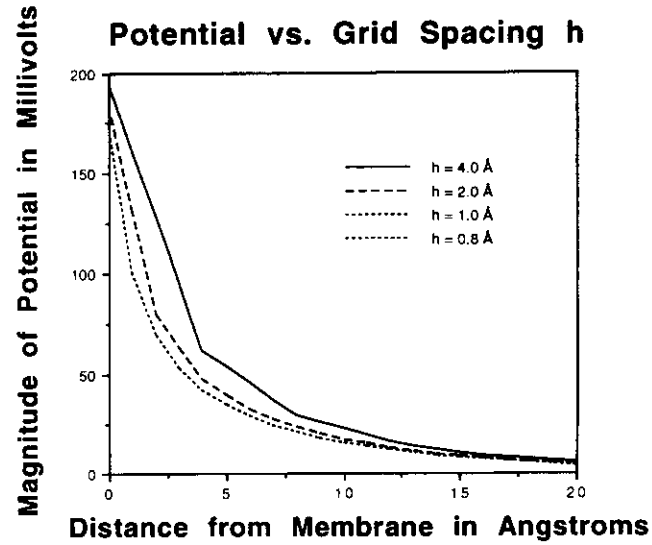

Figure 2. Plots of the magnitude of the potential in the electrolyte as a function of grid spacing h at an ionic strength of 150 mM and a charge density of 1/256 Å^{-2}. The solid curve is for $h = 4.0$ Å, the dashed curve is for $h = 2.0$ Å, and the dotted curve represents both $h = 1.0$ Å and $h = 0.8$ Å, which are indistinguishable on the scale of the graph.

TABLE 1: Planarity of Potentials[a]

charge density, e·Å^{-2}	ionic strength 150 mM	25 mM	10 mM
1/64	7	3	2
1/256	10	7	6
1/576	20	12	11

[a] Distances (in Å) from the membrane surface beyond which the potential deviates by less than 5% from its average value in a plane parallel to the membrane.

One feature of the Gouy–Chapman model is that the potential, as given by eq 2.3, is planar, in that it is constant in any plane parallel to the membrane surface. We can test this aspect of the numerical solutions by finding the average potential $\bar{\phi}(z)$ at a distance z from the membrane surface with the expression

$$\bar{\phi}(z) = \sum_{i,j} \phi(i,j,K) \quad (4.1)$$

where the directions defined by i and j are parallel to the membrane and the sum runs over all grid points, with fixed K, that are a distance z from the membrane. The deviation of $\phi(i,j,K)$ from this average value, defined as the absolute value of the difference between $\phi(i,j,K)$ and $\bar{\phi}(z)$ divided by $\bar{\phi}(z)$, provides a measure of the variation of the potential in the K plane. In Table 1, the distances at which the maximum deviation from $\bar{\phi}(z)$ becomes less than 5% are presented for all of the charge densities and ionic concentrations at which we have performed calculations. It is seen that this distance is as small as 2 Å for $\sigma = 1/64$ Å^{-2} and $I = 10$ mM and as large as 20 Å at $\sigma = 1/576$ Å^{-2} and $I = 150$ mM. This distance increases with both increasing ionic concentration and decreasing charge density, but in all cases, the potential becomes totally planar, up to the accuracy of the solution, within 30 Å of the membrane.

In addition to the planarity, the magnitude of the electrostatic potential can also be checked against Gouy–Chapman theory. At distances beyond those given in Table 1, our solution agrees with

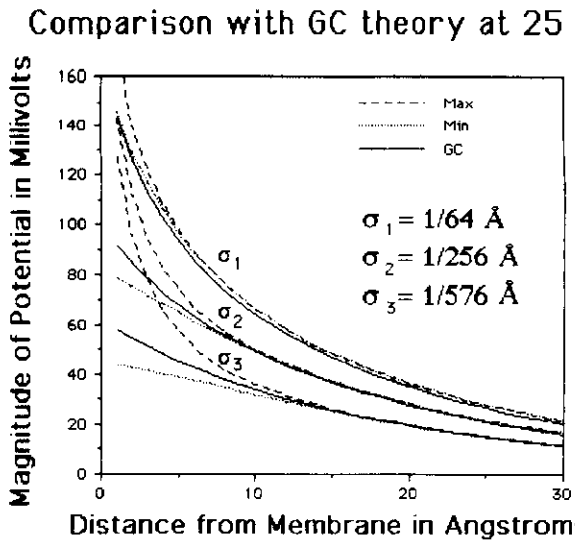

Figure 3. Plots of the magnitude of the potential as a function of the distance from the membrane at an ionic strength of 25 mM at three charge densities. The solid curve is the Gouy–Chapman result, the dashed curve is the numerical solution on a line perpendicular to the membrane and passing through the charge, and the dotted curve is the numerical solution on a line perpendicular to the membrane but far from the charge such that the potential is near its minimum value.

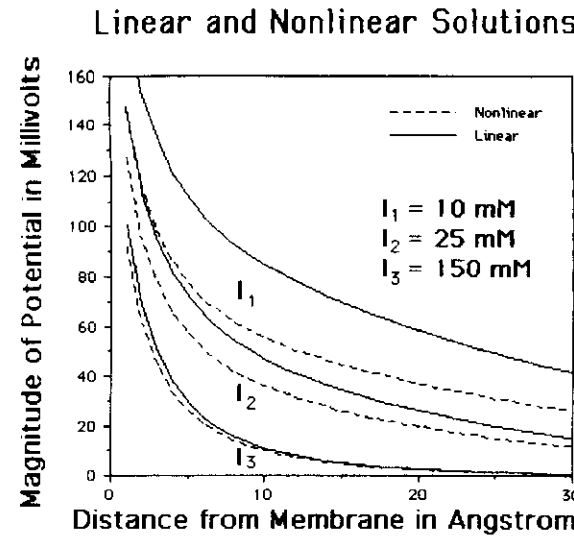

Figure 4. Comparison of the numerical solutions of the linearized and nonlinear Poisson–Boltzmann equations at a charge density of $1/576$ Å^{-2} for three ionic strengths. The potential is given on a line perpendicular to the membrane and passing through the charge. The solid curve gives the linearized solution, and the dashed curve represents the nonlinear potential.

the Gouy–Chapman prediction to within the calculational error, except when $\sigma = 1/64$ Å^{-2} and $I = 150$ mM, where the difference between the two methods is about 7%. This larger discrepancy is likely due to the specific features of our model lipid system, since the smaller lattice spacing gives rise to larger potentials which in turn tends to emphasize the precise placement of the charges with respect to the membrane–electrolyte interface. The predictive value of the Gouy–Chapman model is also useful in regions in where the potential is nonplanar; the average potential $\bar{\phi}(z)$, as given by eq 4.1, agrees with the Gouy–Chapman result to within the calculational error at both $\sigma = 1/256$ Å^{-2} and $1/576$ Å^{-2} even at $z = 0$, the membrane surface, a conclusion also reached by Sauvé and Ohki.[13] For $\sigma = 1/64$ Å^{-2}, this difference is again slightly larger being 3% at $I = 10$ mM, 10% at $I = 25$ mM, and 14% at $I = 150$ mM for $z = 0$. These differences between the average potential and the Gouy–Chapman value become smaller as one moves away from the membrane and into the electrolyte region.

In Figure 3, the numerical solution is graphed along with the Gouy–Chapman potential at $I = 25$ mM for three charge densities. The plot shows the potential in the region of electrolyte which is closest to the charged surface. For the sake of convenience, from here on we only discuss the *magnitude* of the electrostatic potential, which is always positive, even though the actual potential itself is always negative. Two curves are given for the numerical case. One represents the solution on a line passing through the charge but perpendicular to the membrane. The other gives the potential on a line again perpendicular to the membrane, but far away from the charge, where the potential is near its minimum value at a given length from the membrane surface. It is seen that while all three plots, for a fixed lattice spacing, are equal at large distances, they diverge from each other as z gets closer to zero. The maximum value of the potential deviates much more from the Gouy–Chapman on theory than the minimum value does. This is true for all lattice spacings and at all ionic strengths. At the membrane–electrolyte interface, the deviation of the minimum from the Gouy–Chapman potential ranges from 9 to 50%, while the maximum value may be as much as a factor of 2 greater than the Gouy–Chapman value. These deviations grow as the charge density decreases and as the ionic concentration gets larger.

We finally wish to consider the validity of the linearized approximation to the Poisson–Boltzmann equation, which is often employed in analytical work. The plots in Figure 4 show numerical solutions along a line passing through the charge and perpendicular to the membrane for the linearized and full nonlinear Poisson–Boltzmann equations at a charge density of $\sigma = 1/576$ Å^{-2}. If the Gouy–Chapman model is used to predict the value of the dimensionless potential in eq 2.4, then u_0 equals 3.2, 2.4, and 1.2 for ionic strengths of 10, 25, and 150 mM, respectively. Strictly speaking, the condition for the linearized equation to hold is that u_0 be much less than unity, although in practice this approximation has been found to have a wider range of validity due to absence of quadratic terms in eq 2.1.[19] This criterion, however, has only been derived within the assumption of constant planar charge density and may not be relevant for the discrete charge distributions studied numerically here, which tend to yield much larger potentials in the neighborhood of the charge. Both the linear and nonlinear methods give similar potentials at $I = 150$ mM, but the linearized equation gets worse at lower salt concentrations where the potential is larger, as might be anticipated. In fact, the linear solution at 25 mM near the membrane is quite close to nonlinear potential at 10 mM. This is only coincidental, but it does point to the need for a consideration of the nonlinear Poisson–Boltzmann equation in many cases, even at relatively low charge density.

V. Membrane Potential

Because of the way the problem is set up, the present numerical technique can also be used to determine the effect of the membrane surface charge on the potential in the interior of the lipid. This is demonstrated in this section, again for a simple model system. The geometry of Figure 1 is employed with both the bottom and top layers of electrolyte measuring 60 Å from the membrane surface to the end of the box. The membrane is 40 Å thick. In contrast with the previous calculations, *two* negative charges of magnitude e are placed in the cell, one 2 Å below the top of the membrane and the other 2 Å above the bottom of the lipid region. Both charges are centered with respect to the directions parallel to the membrane surface. The cell measures 18×18 Å^2 in these coordinates, implying an average charge density of $1/324$ Å^{-2} near both membrane surfaces, and a single ionic strength of 150 mM is investigated, giving a Debye length that is roughly equal to the lattice spacing. These parameters are also close to a typical density for a charged biomembrane and the ionic concentration at physiological conditions. Periodic boundary conditions are

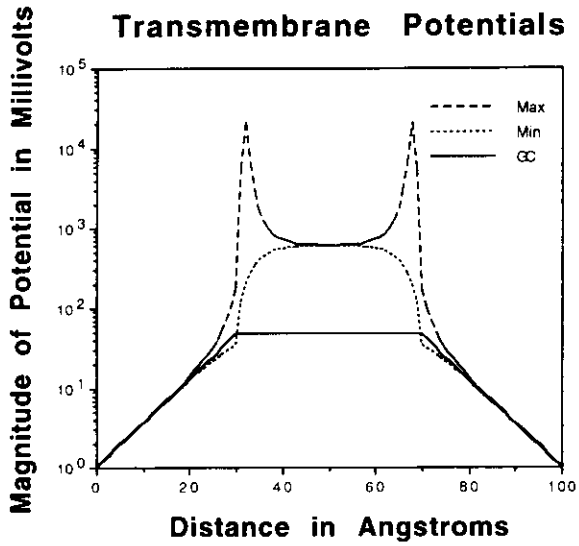

Figure 5. Plots of the magnitude of the potential as a function of the distance from the membrane at an ionic strength of 150 mM and a charge density of 1/324 Å^{-2} at both membrane surfaces. The solid curve is the Gouy–Chapman result, the dashed curve is the numerical solution on a line perpendicular to the membrane and passing through the charges, and the dotted curve is the numerical solution on a line perpendicular to the membrane but far from the charges such that the potential is near its minimum value.

again enforced, and a grid spacing of 1 Å is employed. The dielectric constants are assigned as in the preceding section. Since this problem has a geometry which is symmetric about the midplane of the membrane, it can actually be solved using only half of the grid with alternate boundary conditions.[28] However, the present approach, which is applicable to more general situations, can also easily handle the problem with currently available computational resources.

Plots of the electrostatic potential are shown in Figure 5 along with the predictions of Gouy–Chapman theory. The potentials are shown on a line passing through both charges and on a second line perpendicular to the membrane, but far from the charges such that the potential is near its minimum value at a given distance from the membrane surface. The charge on one side of the membrane has little effect on the potential in the electrolyte on the opposite side, as noted in previous studies,[29] and thus in the solvent the agreement with the Gouy–Chapman model is similar to that discussed in the previous section.

Our numerical approach can also be employed to find the electrostatic potential in the interior of the membrane. However, we caution that, since the charges are buried in the membrane unscreened by ions, the results obtained in this section may be particularly dependent on the details of the system. It is likely that a successful comparison with experiment will require an atomic-level model of the lipid and a better account of the variation of the dielectric constant across the interface.[30] The latter is especially important for calculating potentials in the head group region where fluorescence probe and capacitance measurements show the dielectric to be intermediate between that of the solvent and the membrane. Such situations have been dealt with successfully in statistical mechanical treatments of the swelling of clays,[31] and within the finite difference approach, one can also include the effects of a spatially varying dielectric constant. The purpose of the calculations to be presented below is to illustrate how the transmembrane potential might be influenced by the presence of concentrated, rather than smeared, charges. A manifestation of this is apparent in Figure 5, where the potential approaches a constant value of about 610 mV deep inside the membrane, an order of magnitude higher than the Gouy–Chapman value.

The transmembrane potential can be further investigated by visualization as in Figure 6a, which is a color contour representation of the electrostatic potential in a plane containing the charges and at right angles to the membrane surface. In order to clearly display the several orders of magnitude over which the potential spans, a logarithmic plot is used, and several cells have been duplicated to stress the periodic nature of the solution. The approach of the potential to planarity is discernible above and below the membrane. We can also examine the potential in a plane parallel to the membrane surface. In Figure 6b, a linear, rather than logarithmic, contour plot of the potential 10 Å deep into the membrane is presented. Again, several cells are shown to illustrate the periodicity. The maximum values are collinear with the charges, and the minima also form a rectangular lattice which exactly interpenetrates that of the maxima. In addition, there are saddle points where the lines connecting neighboring maxima intersect with the corresponding lines which connect the minima. The magnitude of the potential from trough to peak goes from 554 to 713 mV. In the midplane of the membrane, between the two layers of charge, the potential undergoes less variation, ranging between 606 and 615 mV. At the membrane–electrolyte interface the potential has a minimum at 34 mV and a maximum at 172 mV, bracketing the Gouy–Chapman value. Again, we emphasize that these results reflect the specific

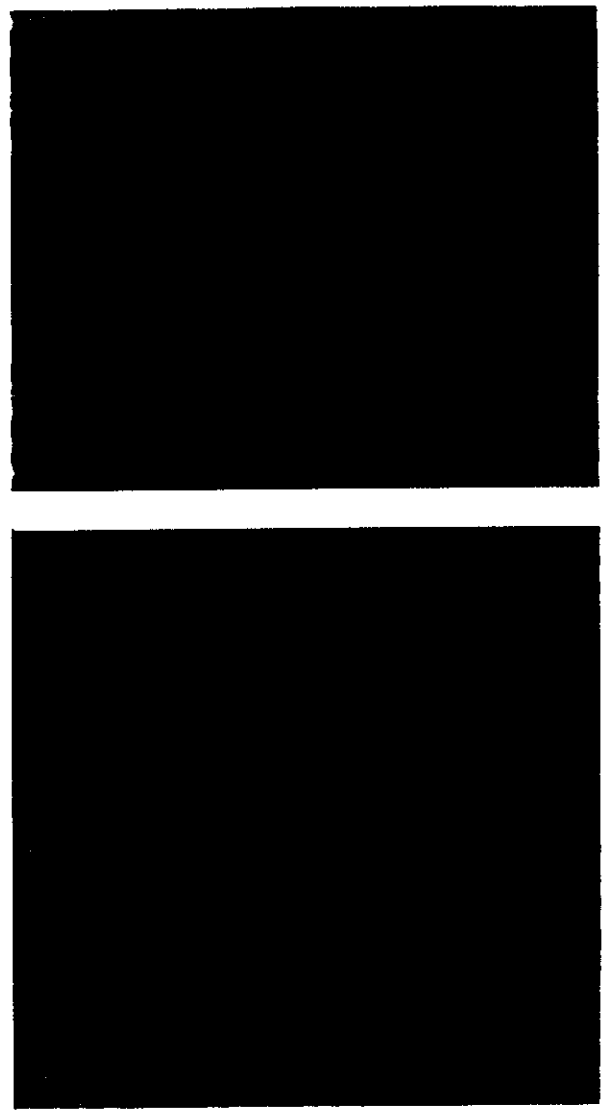

Figure 6. Color contour plot of the (a, top) logarithm of the transmembrane potential in a plane containing the charges and perpendicular to the membrane and (b, bottom) the magnitude of the transmembrane potential in a plane parallel to the membrane and 10 Å below its surface. Regions where the magnitude of the potential is larger are in red and orange, and areas where the potential is smaller are in blue and green.

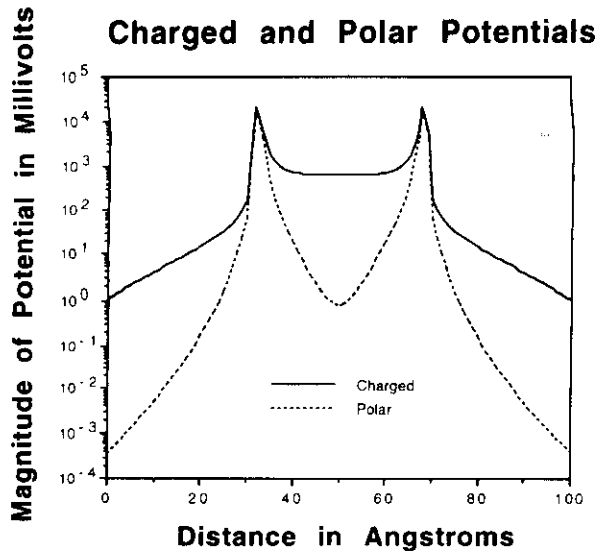

Figure 7. Plots of the magnitude of the potential for a charged and polar membrane at an ionic strength of 150 mM and a charge or dipole density of 1/324 Å^{-2} at both membrane surfaces. The solid curve represents the charged model, and the dotted curve is for the polar system. The potentials are given on a line perpendicular to the membrane and passing through two charges.

characteristics of the model system, but serve to demonstrate the stability of the numerical method for obtaining transmembrane potentials.

As mentioned in the Introduction, the numerical method described herein can be applied to more general situations than those covered by Gouy–Chapman theory. We have therefore performed a limited number of calculations involving rectangular lattices of dipoles. In these computations, two unit charges of opposite sign, each lying 2 Å below the membrane, are placed 2 Å apart along one of the axes of the cell and parallel to the interface. Although electrically neutral, this charge distribution has a net dipole moment along the membrane surface. As the resulting potential is relatively weak, the solutions obtained from both the linearized and nonlinear Poisson–Boltzmann equation are virtually indistinguishable from each other, even when there is as much as one dipole per 64 Å^2 and the ionic strength is as low as 10 mM. This suggests that there are physical systems where analytic treatments of the linearized Poisson–Boltzmann equation may be especially useful. Because of the alternating charges, the nonplanarity of the potential persists much further out into the solvent than for the charged lipid case.

In Figure 7, the potential for this dipolar model is plotted using all of the parameters given in this section, where the cell is 18 × 18 × 160 Å^3 and the ionic strength is 150 mM. Two dipoles are placed in the box, one at each interface, with charges of the same sign directly above one another. The magnitude of the potential on a line passing through one set of charges and perpendicular to the membrane is shown along with the corresponding result for the charged membrane which has been previously discussed in this section. As expected, the dipole potential is much weaker, except near the charge. It is also seen that the rate of the decay in both the electrolyte and the lipid is greater in the dipole case. Naturally, all of the above conclusions depend both on the dipole orientation and its position with respect to the membrane–electrolyte boundary.

VI. Discussion

We have deliberately chosen simple models for the lipid–electrolyte system in order to establish the viability of our numerical approach and to bring out some of the basic features of membrane electrostatics. The next step would be to implement a more realistic description of the lipid by using atomic coordinates from either crystallographic data[32] or computer simulations.[33,34] The excess charge in biomembranes tends to reside on head groups which protrude out into the solvent, and in some instances, these head groups are polar but uncharged.[35] This situation cannot be handled within Gouy–Chapman theory but is amenable to the techniques outlined here. It is also possible to obtain the electrostatic potential in the neighborhood of a membrane-bound protein with these methods. The program can additionally be modified to handle different electrolytes on each side of the membrane, as is often the case experimentally, and pore-forming proteins can also be represented in a computation.

The size of the region needed to accurately solve the nonlinear Poisson–Boltzmann equation can be substantially reduced by using the Gouy–Chapman potential to set boundary conditions at the top and bottom of the cell. Although we know of no proof that this procedure is rigorous in the nonlinear case, the philosophy is similar to that adopted in protein electrostatics where approximate boundary conditions allow one to truncate the grid to a tractable size.[17] Moreover, our calculations indicate that the numerical solution agrees very well with the Gouy–Chapman model at large enough distances from the membrane. In fact, the present study can be regarded as a justification for the prescription of such a boundary condition. The use of smaller grid volumes will enable the use of smaller grid spacings. This therefore means that the lipid region can be modeled in finer detail. We also note that larger problems may be more efficiently handled through the use of multigrid-based methods[22,36] or on massively parallel architectures.

There are a number of possible applications of these methods. One is to the adsorption of charged molecules on membrane surfaces, as discrete-charge effects are thought to play a role in this process.[37] The diffusion of ligands to membrane-bound receptors, which has been studied through Brownian dynamics,[38,39] can be influenced through electrostatic steering by the membrane field, and this phenomenon may be better understood with the help of more accurate potentials. Other areas of investigation might concern the transport of ions across membranes and the insertion of peptides or proteins into lipid bilayers. The Poisson–Boltzmann equation has also been used to explain empirical observations involving membrane-like geometries obtained with the surface-force apparatus and the atomic force microscope.[40]

VII. Conclusion

We have performed numerical calculations in which the full nonlinear Poisson–Boltzmann equation has been solved for model membrane–electrolyte systems through the imposition of periodic boundary conditions. This procedure avoids the smeared charge assumption of the Gouy–Chapman theory and can be adapted to describe a greater variety of physical situations. For an infinite rectangular array of membrane charges, the numerical solution agrees well with the Gouy–Chapman model at a sufficiently large distance from the membrane. Closer to the membrane, the average potential at a fixed distance from the surface is well-predicted by Gouy–Chapman theory. The distance from the membrane at which the potential becomes planar decreases both as the lattice spacing decreases and as the Debye length gets larger. Our method can also be used to determine the interior lipid potential, which is found to reflect the geometry of the charge distribution. As another example of the power of this procedure, computations have been presented for the case where there is a lattice of uncharged dipoles near the lipid–solvent interface. The Gouy–Chapman theory can be used to fix the boundary conditions on the potential, further reducing the effort required for solution of the problem. This approach, which can be extended to increasingly complicated systems, provides a versatile technique for modeling membrane electrostatics.

Acknowledgment. We thank M. Holst, F. Saied, and M. D'Mello for useful discussions. We are grateful to J. A.

McCammon for providing us with a copy of the UHBD code. This work was supported in part by NSF Grant MCB 92-19619, a grant from FMC Corp., grants from the NSF Biotechnology Program, and a grant from the National Center for Supercomputing Applications (NCSA). We also thank the NCSA for allocations of computational resources.

References and Notes

(1) McLaughlin, S. *Curr. Top. Membr. Transp.* **1977**, *9*, 71.
(2) Barber, J. *Biochim. Biophys. Acta* **1980**, *594*, 253.
(3) McLaughlin, S. *Annu. Rev. Biophys. Biophys. Chem.* **1989**, *18*, 113.
(4) Carnie, S. L.; Torrie, G. M. *Adv. Chem. Phys.* **1984**, *81*, 141.
(5) Feller, S. E.; McQuarrie, D. A. *J. Phys. Chem.* **1992**, *96*, 3454.
(6) McLaughlin, S. In *Physical Chemistry of Transmembrane Ion Motions*; Spach, G., Ed.; Elsevier: Amsterdam, 1983; pp 69–75.
(7) Haynes, D. H. *J. Membr. Biol.* **1974**, *17*, 341.
(8) Anderson, O. S.; Feldberg, S.; Nakadomari, H.; Levy, S.; McLaughlin, S. *Biophys. J.* **1978**, *21*, 35.
(9) Tsien, R. Y.; Hladky, S. B. *Biophys. J.* **1982**, *39*, 49.
(10) Stillinger, F. *J. Chem. Phys.* **1961**, *35*, 1584.
(11) Cole, K. S. *Biophys. J.* **1969**, *9*, 465.
(12) Nelson, A. P.; McQuarrie, D. A. *J. Theor. Biol.* **1975**, *55*, 13.
(13) Sauvé, R.; Ohki, S. *J. Theor. Biol.* **1979**, *81*, 157.
(14) Stigter, D.; Dill, K. A. *Langmuir* **1986**, *2*, 791.
(15) Arakelian, B.; Walther, D.; Donath, E. *Colloid. Polym. Sci.* **1993**, *270*, 268.
(16) Warwicker, J.; Watson, H. C. *J. Mol. Biol.* **1982**, *157*, 671.
(17) Sharp, K. A.; Honig, B. *Annu. Rev. Biophys. Biophys. Chem.* **1990**, *19*, 301.
(18) Davis, M. E.; McCammon, J. A. *Chem. Rev.* **1990**, *90*, 509.
(19) Verwey, E. J. W.; Overbeek, J. T. G. *Theory of Stability of Hydrophobic Colloids*; Elesvier: Amsterdam, 1948.
(20) Grahame, D. C. *J. Chem. Phys.* **1953**, *21*, 1054.
(21) Cai, M.; Jordan, P. C. *Biophys. J.* **1990**, *57*, 883.
(22) Holst, M.; Kozack, R. E.; Saied, F.; Subramaniam, S. *Proteins* **1994**, *18*, 231.
(23) Davis, M. E.; Madura, J. D.; Luty, B. A.; McCammon, J. A. *Comput. Phys. Commun.* **1991**, *62*, 187.
(24) Meijernik, J. A.; van der Horst, H. A. *J. Comput. Phys.* **1981**, *44*, 134.
(25) Ames, W. *Numerical Methods for Partial Differential Equations*, 2nd ed.; Academic Press: New York, 1977.
(26) Hockney, R. W.; Eastwood, J. W. *Computer Simulation Using Particles*; Adam Hilger: New York, 1988.
(27) Nicholls, A.; Honig, B. *J. Comput. Chem.* **1991**, *12*, 435.
(28) D'Mello, M. Private communication.
(29) Chandler, W. K.; Hodgkin, A. L.; Meves, H. *J. Physiol. (London)* **1965**, *180*, 821.
(30) Curry, J. E.; McQuarrie, D. A. *J. Colloid Interface Sci.* **1992**, *154*, 289.
(31) Curry, J. E.; McQuarrie, D. A. *Langmuir* **1992**, *3*, 1026.
(32) Hauser, H. *Biochim. Biophys. Acta* **1984**, *772*, 37.
(33) Chiu, S.-W.; Gulukota, K.; Jakobsson, E. In *Membrane Proteins: Structures, Interactions and Models*; Pullman, A., Jortner, J., Pullman, B., Eds.; Kluwer: Boston, 1992; pp 315–338.
(34) Berendsen, H. J. C.; Egberts, B.; Marrink, S.-J.; Ahlstrom, P. In *Membrane Proteins: Structures, Interactions and Models*, Pullman, A., Jortner, J., Pullman, B., Eds.; Kluwer: Boston, 1992; pp 457–470.
(35) Gennis, R. B. *Biomembranes. Molecular Structure and Function*; Springer-Verlag: New York, 1989.
(36) Oberoi, H.; Allewell, N. M. *Biophys. J.* **1993**, *65*, 48.
(37) Winiski, A. P.; McLaughlin, A. C.; McDaniel, R. V.; Eisenberg, M.; McLaughlin, S. *Biochemistry* **1986**, *25*, 8206.
(38) Forsten, K. E.; Lauffenburger, D. A. *J. Comput. Mol. Cell Biol.*, in press.
(39) Linderman, J. J.; Mahama, P. A.; Forsten, K. E.; Lauffenburger, D. A. *Adv. Chem. Eng.*, in press.
(40) Tsao, Y.-H.; Evans, D. F.; Wennerström, H. *Science* **1993**, *262*, 547.

CHAPTER I. MULTIPLE-SITE TITRATION THEORY AND ELECTROSTATIC METHODS

The calculation of protein titration curves is a problem with two main parts. The titration curve is merely the number of protons bound to the protein as a function of pH. A protein in equilibrium with a solution of a given pH will always have the same macroscopic protonation state. This measurable protonation state, however, is made up of a constantly fluctuating ensemble of microscopic states; a distribution of protonation states with different numbers of protons bound are possible at each pH, and for any number of protons that are bound, there are numerous configurations in which they can be bound to the titrating sites of an individual protein molecule. Calculation of the pH-dependent behavior of proteins depends on an understanding of the electrostatic interactions that control the protonation behavior of individual titrating sites in the protein; the first problem is thus that of correctly calculating the effect of electrostatic interactions between each titrating site in the protein with the background of partial charges and dipoles in the protein and with other titrating sites. The second problem is the determination of average protonation states for each site from the ensemble of possible ionization states; due to current limitations on available computing time and memory, alternatives to exact enumeration of 2^M ionization states are required in calculations involving proteins with more than about 25 titrating sites.

Early Approaches to the Calculation of pKa Values in Proteins

Prior to the development of numerical methods for solving the Poisson equation and modifications of that equation, analytic electrostatic potential calculations based on Coulomb's law were carried out on models of protein molecules. The earliest theoretical model for calculating the effects of interaction between titrating sites in proteins relied on several grossly simplifying assumptions. (Linderstrom-Lang, 1924) This model assumed the protein to be a spherical object impenetrable to solvent; all titratable groups to be independent of each other except for electrostatic interactions; all titratable groups of a particular kind to be intrinsically identical; and all charges to occupy with equal probability any position on the surface of the protein sphere. The possible protein ions, with various integral total charges, were not individually represented but treated as a single kind of ion with a continually variable charge. These assumptions had the advantage of allowing an analytical solution to the multiple-site titration problem; however, the accuracy of such a

solution is limited to rough prediction of global properties. Local properties, such as the behavior of particular titrating sites, catalytic behavior, redox potentials and the like, were beyond the scope of these methods.

The result of the above assumptions was the titration curve of a protein as a superposition of the curves for individual types of groups, the fraction of dissociated groups of a particular type being given by:

$$pH - \log\frac{\alpha}{1-\alpha} = pK_{int} - \frac{1}{2.303kT}\frac{\delta W}{\delta Z}$$

where pKa_{int} is the intrinsic pKa of a type of group--the pKa of the group not in solution, but in a hypothetical discharged protein. pKa_{int} was a useful quantity in these calculations, and the discharged protein a useful reference state. Use of an empirical pKa_{int} could be said to account for effects which were not explicitly included in the model, so that only Coulombic interactions between charged residues in the low dielectric region need be explicitly considered. **W** is the work of adding the protein charges to the molecule. Considering all of the charges to be smeared evenly over the surface of the protein sphere allows positive and negative charges to cancel, as they occupy the same space, leaving only the average net charge $\overline{Z}$ to be considered. In terms of $\overline{Z}$:

$$\mathbf{W} = \frac{\overline{Z}^2\varepsilon^2}{2D}\left(\frac{1}{b} - \frac{k}{1 + ka}\right)$$

Where b is the radius of the low-dielectric protein sphere, a is the depth of the ion exclusion layer, κ is the Debye-Huckel parameter proportional to the square root of the ionic strength, ε is the protonic charge and D the solvent dielectric constant. Given this expression for **W**, the first expression becomes:

$$pH - \log\frac{\alpha}{1-\alpha} = pK_{int} - 0.868\,\frac{\overline{Z}\varepsilon^2}{2DkT}\left(\frac{1}{b} - \frac{k}{1 + ka}\right)$$

pKa Calculations with Discrete Titrating Sites

Anticipating the need for a solution to the problem of multiple titrating sites that more realistically represented the protein molecule, in which titrating entities can not be assumed to be identical and evenly distributed but are fixed in particular

environments, Tanford and Kirkwood (1957) proposed a theory of multiple titrating sites that included discrete charges at arbitrary points on the surface of the solute, and considered the ensemble of individual ionization states explicitly. The model of the protein used was a spherical cavity of dielectric D_i with point charges m embedded in it. Titratable groups in proteins were assumed to exist in only two states, an acidic form and a basic form, only one of which was charged for any individual group. Each of the m points was assigned a charge of 0 or +1 for basic groups and 0 or -1 for acidic groups. The resulting expression for the work of charging the protein was:

$$\mathbf{W}_{ij} = \frac{\varepsilon^2 z_i z_j}{2b}(A_{ij} - B_{ij}) - \frac{\varepsilon^2 z_i z_j}{2a} C_{ij}$$

where ε is the electronic charge, z_i and z_j are the charges at sites i and j in units of ε, and A_{ij}, B_{ij} and C_{ij} are complex functions:* A_{ij} represents the work of charging the site in an infinite medium with dielectric constant the same as the protein interior; B_{ij} modifies this factor appropriately due to the boundary between the dielectric phases; and C_{ij} represents the effect of mobile ions on the work of charging.

While the method of calculation of electrostatic energies was still inexact, the theoretical approach to calculation of multiple-site titration presented by Tanford and Kirkwood is still used in most modern algorithms for pKa calculation. Though Tanford and Kirkwood provided a theoretical framework for solving the problem of multiple titrating sites, their model was extremely limited. Knowledge of the

---

* The A_{ij}, B_{ij} and C_{ij} terms are fully expressed as follows:

$$A_{ij} = b/D_i r_{ij}$$

$$B_{ij} = \frac{1}{D_i}\sum_{n=0}^{\infty} \frac{(n+1)(D - D_i)}{(n+1)D + nD_i} \rho_{ij}^n P_n(\cos\Theta_{ij})$$

$$C = \frac{1}{D}\left\{\frac{x}{1+x} + \sum_{n=1}^{\infty} \frac{2n+1}{2n-1}\left[\frac{D}{(n+1)D+nD_i}\right]^2 \times \frac{x^2 \sigma_{ij}^n P_n(\cos\Theta_{ij})}{\frac{K_{n+1}(x)}{K_{n-1}(x)} + \frac{n(D-D_i)}{(n+1)D+nD_i}\left(\frac{b}{a}\right)^{2n+1}\frac{x^2}{4n^2-1}}\right\}$$

$$x = \kappa\alpha; \quad \rho_{ij} = r_i r_j / b^2; \quad \sigma_{ij} = r_i r_j / a^2; \quad K_n(x) = \sum_{s=0}^{\infty} \frac{2^s n!(2n-s)!}{s!(2n)!(n-s)!} x^2$$

$P_n(\cos\Theta_{ij})$ represents Legendre polynomials and r_i, r_j, r_{ij}, and Θ_{ij} distances and angles describing the relationship between the locations of the two sites.

internal architecture of proteins was minimal when the model was developed. As a result, titrating groups are assumed to be found only at the protein surface; all acidic titrating groups are considered equal as are all basic groups, and individual sites are not distinguishable from other sites of the same type. The protein is considered as a uniform low-dielectric body, neglecting by necessity the effects of the partial charges of particular atoms on the electrostatic field of the protein. The calculation of pKa shifts is referred to the hypothetical discharged state, necessitating the use of experimentally adjusted 'intrinsic' pKa values as starting points for the prediction of pKa shifts. Knowledge of protein structure at atomic resolution, and development of numerical methods for calculating electrostatic energies has provided better 'input' for the basic calculation described below, and allowed calculation of shifts of solution pKa values of model compounds rather than of experimentally determined or estimated intrinsic pKa values. Algorithms for guided sampling of ionization states has reduced the problem of enumeration of states to more manageable dimensions. The theory of multiple titrating sites, however, remains essentially the same.

The multiple-site titration problem is essentially a problem of ligand binding with multiple interacting ligands. A hypothetical neutral protein, to come to equilibrium with a solution of arbitrary pH, must of necessity undergo a spontaneous ionization process. The difference in free energy between the two states can be termed the ionization energy. Analysis of the equilibrium between the neutral state and the ionized states at different pH values provides a description of the macroscopic titration behavior of the protein. Gilson (1993) applied the binding polynomial treatment of multiple ligand binding derived by Schellman (1975) to develop an expression for the difference in free energy between the neutral state and arbitrary ionized states; this work is the basis of the method used for pKa calculations reported and proposed in the following chapters. While this ionization polynomial method is an expansion on the original Tanford-Kirkwood theory tailored to the use of modern continuum electrostatic methods, it is similar in essence and thus will be used to illustrate the multiple titrating site theory.

For a solution of a protein at concentration P having M titratable sites (1,2...i...M), each ionization state of the protein, α, can be described by a vector with components $x_\alpha(i)m$, which is 0 for site i neutral and 1 for site i ionized. Each ionizable group can be considered to be fully neutral or fully ionized at any moment, but the protein fluctuates among the set of 2^M ionization forms α. The concentration of the neutral

protein (ionization state $\alpha = 0$) is P_0. Any ionization form a is found in concentration P_α, with fractional occupancy P_α/P; the fractional occupancy of the neutral protein is then:

$$f_0 = 1 - \sum_{\alpha \neq 0} f_\alpha$$

The net charge of ionization form α is:

$$q_\alpha = \sum_{i=1}^{M} x_\alpha(i) z(i)$$

And the mean number of protons which may bind to the neutral protein on going to equilibrium is:

$$q = \sum_{\alpha} f_\alpha q_\alpha$$

Equilibrium constants K_α for the formation of the ionization form α from the neutral protein may be written:

$$K_\alpha = \left(\frac{P_\alpha}{P_0[H^+]^{q_\alpha}}\right) = e^{-\beta(\mu_\alpha^0 - \mu_0^0 - q_\alpha \mu_{H^+}^0)}$$

where $\beta = 1/RT$, and the chemical potentials are those of the protein in ionization form α, the neutral protein, and the proton, respectively.

In order to calculate the energy of ionization from neutral to form a, the free energy of the system when all of the protein is in the neutral state must be calculated, as well as the free energy of the system at equilibrium with a solution of a given pH. The free energy for the state I, in which the protein is neutral and $P_0 = P$, the free energy of the system will be:

$$G_I = \mu_0^0 + RT \ln P_0 + q(\mu_{H^+}^0 + RT \ln [H^+]) + G_{fixed},$$

where G_{fixed} are the elements of the free energy that are not affected by ionization. The free energy for state II, in which the protein is in equilibrium with solution and the protein has taken on a distribution of ionization states α, the free energy is given by:

$$G_{II} = f_0(\mu_0^0 + RT\ln P_0) + \sum_{\alpha \neq 0} f_\alpha(\mu_\alpha^0 + RT\ln P_\alpha) + G_{fixed}$$

and, using the expressions for the fractional occupancy of ionization states above, the difference in energy between the two states can be expressed as:

$$G_{II} - G_I = RT\ln\frac{P_0}{P} + \sum_{\alpha \neq 0} f_\alpha[\mu_\alpha^0 + RT\ln\frac{P_\alpha}{P_0} - \mu_0^0 - q_\alpha(\mu_{H^+}^0 + RT \ln [H^+])].$$

The contents of the square brackets can be made to go to zero for each individual α, using the expression for the equilibrium constants α. In view of this, the expression for the ionization energy becomes:

$$G_{II} - G_I = G_{ion} = RT\ln(\frac{P_0}{P}) \equiv -RT\ln\Sigma$$

where Σ is a slightly modified binding polynomial which is defined here as the ionization polynomial, and given by:

$$\Sigma \equiv \frac{P}{P_0} = 1 + \sum_{\alpha \neq 0} K_\alpha[H^+]^{q_\alpha}.$$

G_{ion} represents the free energy of ionizing the protein; corresponding equilibria for acidic and basic groups in the protein are:

$$A_iH \underset{K_{ai}}{\Leftrightarrow} A_i^- + H^+ \qquad\qquad B_i + H^+ \underset{K_{ai}^{-1}}{\Leftrightarrow} B_iH^+$$

If the K_{ai} values are defined as equal to the Ka values of ionizable residues unperturbed by the protein environment,

$$K_\alpha = \prod_{i=1}^{M} K_{ai}^{-x_\alpha(i)z(i)}$$

In general, the pKa of a group will be perturbed by interactions with other titrating groups, as well as by desolvation and by interactions with charges and dipoles in the protein. In the work of Tanford and Kirkwood, and prior to the development of numerical methods for detailed calculation of protein electrostatics, these latter two effects were rolled into pKa_{int}, the pKa of the titrating group in the neutral protein, which was generally determined by experiment. Details of their explicit calculation

and of the calculation of energies interactions between titrating sites are given in later sections of this chapter. The extra free energy of a titrating group i when all other titrating sites are neutral with respect to the free energy of the unperturbed group (e.g. the solution pKa of an amino acid) is termed $\Delta\Delta G_i$; the extra free energy of ionizing the group i when group j is ionized is termed ΔG_{ij}. The expression for K_α becomes:

$$K_\alpha = e^{-\beta \sum_{i=1}^{M} x_\alpha(i)\,[\Delta\Delta G_i + \sum_{j>i}^{M} x_\alpha(j)\Delta G_{ij}]} \prod_{i=1}^{M} K_{ai}^{-x_\alpha(i)z(i)}$$

The summation in the exponent of e is $G_{elec,\alpha}$, the purely electrostatic energy of ionization state α. Defining, for notational convenience

$$A_i = K_{ai}^{-z(i)}[H^+]^{z(i)},$$

The free energy associated with ionization of the neutral protein to its form at equilibrium with a solution of given pH is then:

$$G_{ion} = -RT\ln\left(\sum_{\alpha=0}^{2^M-1} e^{-\beta G_{elec,\alpha}} \prod_{i}^{M} A_i^{x_\alpha(i)}\right).$$

Improvements in Electrostatic Methods:

Real progress in the calculation of protein pKa shifts required major improvements in the model of the protein used to calculate protein electrostatics; this came with the development of numerical methods for the solution of the Poisson-Boltzmann equation. Because proteins are, in electrostatic terms, large arrays of irregularly placed charged objects, accurate calculation of the electrostatic fields surrounding proteins and of electrostatic interaction energies affecting particular sites within proteins has only recently become a routine matter. The method to be used in this work is based upon solutions of a fundamental equation of classical electrostatics, Poisson's equation for the spatial variation of the electrostatic potential resulting from a given array of charges in a region of uniform dielectric constant (Sharp and Honig, 1990):

$$\nabla^2\Phi(r) = -4\pi\rho(r)$$

where ∇^2 is the LaPlacian operator for the second derivative with respect to the spatial coordinates, $\rho(r)$ is the charge density at a point r, and the permittivity of free space is zero. For a set of point charges the solution to the Poisson equation becomes Coulomb's law:

$$\Phi(r) = \sum_i \frac{q_i}{|r - r_i|}$$

where r_i is the position and q_i the magnitude of the point charge i. If all charges in the system can be represented explicitly, Coulomb's law can be applied rigorously, since all interactions can be considered to take place in free space. A protein in solution, however, is a very complex system--the protein is an irregular, essentially fixed set of charges, while its surroundings are a collection of mobile charges and dipoles, subject to reorientation and other types of motion. The computational power required to calculate the electrostatic potential rigorously for the protein along with a sufficiently large amount of solvent molecules and ions is lacking; therefore, the system of a protein in solution is represented as a low-dielectric region containing the array of protein charges surrounded by a high-dielectric region containing mobile ions. Coulomb's law is not valid when the dielectric varies through space, so it is convenient to solve modified versions of Poisson's equation. Mobile ions are described in terms of probability distributions rather than exact locations, and their electrostatic effects can be described statistically by the Poisson-Boltzmann (PB) equation:

$$\nabla^2\Phi(r) - \kappa^2\sinh[\Phi(r)] = -4\pi\rho(r)$$

in which κ is the Debye-Huckel parameter: $\kappa^2 = \frac{8\pi N e^2 I}{1000 D k T}$

where N is Avogadro's number, T the absolute temperature, e the protonic charge, I the ionic strength, and k Boltzmann's constant. In the general case, in which dielectric constant and charge density vary through space, the full nonlinear Poisson-Boltzmann equation must be solved:

$$\nabla \cdot [\varepsilon(r)\nabla\Phi(r)] - \bar{\kappa}^2(r)\sinh[\Phi(r)] = -4\pi\rho(r)$$

in which the Debye-Huckel parameter is modified by $\bar{\kappa} = D^{1/2}\kappa$; though algorithms which solve the nonlinear Poisson-Boltzmann equation are available, the method

used in this work is based upon solutions of the linearized PB equation, an approximation that is valid in regions of low charge density:

$$\nabla \cdot [\varepsilon(r)\nabla\Phi(r)] - \bar{\kappa}^2(r)\Phi(r) = -4\pi\rho(r)$$

These equations can be solved analytically only for idealized arrangements of charges in, for example, spherical or cylindrical low-dielectric regions. Such inadequate representations of protein structure were used in many early studies of protein electrostatics, including the Tanford-Kirkwood model for calculating protein titration curves, discussed below. However, the application of finite-difference (Davis et. al 1991) and other numerical methods to the problem has made possible reasonably accurate solutions of the linearized PB equation for native proteins.

Warwicker and Watson (1982) first reported a finite-difference solution to Poisson's equation; subsequently, finite-difference algorithms were also developed to solve the linearized and full nonlinear Poisson-Boltzmann equation. (Holst et. al. 1993, Oberoi & Allewell, 1993) In a finite difference Poisson-Boltzmann calculation, the protein is placed at the center of a three-dimensional grid of points *ijk*. Charge density ρ is partitioned to eight grid points that surround the actual location of each charge; the dielectric for each point is set based upon whether the point falls inside or outside the solvent-accessible surface of the protein, and smoothed in the boundary region using a function based upon what fraction of the grid line falls within the solvent phase. The potential at each point is initially set to zero. Φ_{ijk}, the potential at a given point, can then be expressed as a function of the potential at surrounding grid points:

$$\begin{aligned}\rho(i,j,k) * h^2 = {} & \varepsilon(i - \tfrac{1}{2},j,k)(\Phi(i,j,k)-\Phi(i - 1,j,k) \\ & + \varepsilon(i + \tfrac{1}{2},j,k)(\Phi(i,j,k)-\Phi(i + 1,j,k) \\ & + \varepsilon(i,j - \tfrac{1}{2},k)(\Phi(i,j,k)-\Phi(i,j - 1,k) \\ & + \varepsilon(i,j + \tfrac{1}{2},k)(\Phi(i,j,k)-\Phi(i,j + 1,k) \\ & + \varepsilon(i,j,k - \tfrac{1}{2})(\Phi(i,j,k)-\Phi(i,j,k - 1) \\ & + \varepsilon(i,j,k + \tfrac{1}{2})(\Phi(i,j,k)-\Phi(i,j,k + 1) \\ & + \varepsilon_s\kappa^2\Phi(i,j,k)h^2\end{aligned}$$

and the system of linear equations solved iteratively for the entire cubic grid. In the case of the FDPB solver UHBD used in this work, the iteration is carried out using a

preconditioned conjugate gradient (PCG) algorithm. Briefly, this algorithm views the system of equations as the system **Ax=b** in which the dielectric arrays are elements of the matrix **A**, the array of charge densities is the constant vector **b** and the potential the unknown vector **x**. The PCG method iterates until the maximum number of iterations set by the user is reached or until the norm of the residual falls below an acceptable level.

The accuracy of an FDPB calculation is dependent upon many parameters. Atomic partial charges for each atom, and the radii used in determining the dielectric boundary between protein and solvent, are taken from standard parameter sets used in other types of molecular modeling; the dielectric constant of the solvent phase is taken to be approximately 80--the macroscopic dielectric constant of water in a static electric field--while the protein dielectric has been variously determined to be between 2 and 4 and either of these values is used (Harvey, 1989).

The spacing of the grid is a very important parameter in finite-difference calculations. A grid much larger than an atomic radius leads to inaccuracies in ρ as more than one charge may be contained in one cubic grid unit; a grid size too small is computationally expensive as the arrays of ρ and ε become extremely large. A compromise between these two effects can be effected by focusing--first calculating the potential over the whole molecule using a large grid spacing, then using a smaller grid centered on a particular atom or group of atoms to improve accuracy in a region of interest.

FDPB-Based Calculation of Protein pKa Values

The first method to be reported in which pKa shifts were calculated using electrostatic potentials computed for proteins represented as arbitrary arrays of charges, was that of Bashford and Karplus (1990). Theirs was also the first method in which apparent pKa values were calculated directly from model-compound solution pKa values rather than from experimentally determined intrinsic pKa values, making it generally applicable to any protein for which atomic coordinates are available. Placing an ionizable group in a macromolecular environment modifies the energetics of its ionization. It is useful to consider a model compound R which is exactly analogous to a titrating site in the protein, and the thermodynamic cycles related to its protonation in the gas, solvent and protein phases:

$$
\begin{array}{ccc}
R_gH & \Rightarrow & R_g + H_g \\
\Downarrow & & \Downarrow \\
R_sH & \Rightarrow & R_s + H_s \\
 & \Delta G_s(RH,R) & \\
\Delta G_{s,p}(RH)\Downarrow & & \Downarrow\ \Delta G_{s,p}(R) \\
R_pH & \Rightarrow & R_p + H_s \\
 & \Delta G_p(RH,R) &
\end{array}
$$

Calculations can be restricted to the lower cycle if model compounds (e.g. isolated amino acids) having known solution pKa values are used, thereby avoiding the need for any data pertaining to gas-phase ionization of model compounds. When the ionizable group represented by R is 'moved' from the solution phase into a specific site in the protein, the energetics of its ionization are affected by three types of interactions: the Born, or desolvation energy, which amounts to an energy penalty for removing the compound from solvent; the energy of interaction of the group with the background of partial charges in the neutral protein; and the energy of interaction of the group with other ionized groups. Use of this thermodynamic cycle bypasses the need for experimentally determined values of pKa_{int} to 'seed' the pKa calculation.

In a protein with M ionizable groups, each of which is allowed to be either neutral or ionized, the protein has 2^M possible ionization states. This representation does not explicitly represent the two neutral forms of carboxylic acids and histidines, nor does it allow sites to assume anything other than their two most-probable ionization states. It is possible to adapt the method to include multiple neutral forms without making added computational demands, but the problem would become unmanageably large were more than two ionization states allowed for each titrating site. Each ionization state of the protein, α, can be described by a vector with components $x_\alpha(i)$m, which is 0 for site i neutral and 1 for site i ionized. The simplifying assumption is made that ionization does not cause a change in the conformation of the residue in which the titrating site is located, and that ionization involves only addition of a unit positive charge to a single atom in the titrating residue.

To model the ionization equilibria of the protein, $G_{elec,\alpha}$, the extra free energy of ionizing the protein to each ionization form α relative to the energy of ionizing the

same groups in solution, must be calculated. Framing the problem as one of ionization from neutrality rather than of formal protonation or deprotonation reduces the complexity of the calculation, by allowing acidic and basic sites to be treated similarly. The relevant thermodynamic cycle in this case is

$$\begin{array}{ccc} R_{sol,neu} & \Rightarrow & R_{sol,ion} \\ & \Delta G_{neu,ion}(R_{sol}) & \\ \Delta G_{sol,prot}(R_{neu}) \Downarrow & & \Downarrow \Delta G_{sol,prot}(R_{ion}) \\ R_{prot,neu} & \Rightarrow & R_{prot,ion} \\ & \Delta G_{neu,ion}(R_{prot}) & \end{array} .$$

Two FDPB calculations are required for each titrating site, as well as a calculation of the electrostatic potential of the protein molecule in the discharged state. The first potential calculation is for the titrating site isolated from the protein. The titrating site is modeled by an amino acid residue excised from the PDB file and having identical coordinates to the site in the protein; ionization is modeled as addition of a unit charge to the charge of the atom in the site which becomes protonated or deprotonated or, in cases where two equivalent protonation sites are present, to an atom directly above the branch point. The second potential calculation is for the titrating site within the protein.

Considering a protein with two titrating sites *i* and *j*, and N protein charges, of which 1-->m belong to site *i*, m-->n belong to site *j*, and n-->N belong to the non-ionizable groups in the protein, the electrostatic energy of group *i* neutral in solution is

$$G_{sol,neu} = \frac{1}{2} \sum_{a=1}^{m} \sum_{b=1}^{m} q_a q_b \Phi_{ab}$$

where Φ_{ab} is the potential at charge *b* due to a unit charge at site *a* . Φ_{ab} is equal to Φ_{ba} by reciprocity; Φ_{aa}, the infinite Coulombic self-potential (the energy of compressing a finite charge into a point, which is not relevant in a solvation free energy calculation) becomes a finite term in the FDPB calculation dependent on lattice spacing, orientation of the protein to the lattice and the dielectric constant. This term vanishes if the titrating site is in the same orientation with respect to the finite-difference grid in both FDPB calculations as described above.

The electrostatic energy of the group *i* ionized in solution is

$$G_{sol,ion}(i) = \tfrac{1}{2}(q_1 + z_i)^2\Phi_{11} + (q_1 + z_i)\sum_{a=2}^{m} q_a\Phi_{1a} + \tfrac{1}{2}\sum_{a=2}^{m}\sum_{b=2}^{m} q_aq_b\Phi_{ab}.$$

Thus the electrostatic energy change when the group i ionizes in solution can be expressed as

$$\Delta G_{sol}(i) = \tfrac{1}{2}z_i^2\Phi_{11} + z_i\sum_{a=1}^{m} q_a\Phi_{1a}$$

Values of Φ_{1a} are obtained from a FDPB calculation with a unit charge at the site of ionization of the isolated titrating group. The total electrostatic energy of the protein when groups i and j are both neutral is

$$G_{prot,neu}(i) = \tfrac{1}{2}q_1^2\Psi_{11} + \tfrac{1}{2}q_{m+1}^2\Psi_{m+1,m+1} + q_1q_{m+1}\Psi_{1,m+1} + q_1\left(\sum_{a=2}^{m} q_a\Psi_{1a} + \sum_{a=m+2}^{n} q_a\Psi_{1a} + \sum_{a=n+1}^{N} q_a\Psi_{1a}\right)$$
$$+ q_{m+1}\left(\sum_{a=m+2}^{n} q_a\Psi_{m+1,a} + \sum_{a=2}^{m} q_a\Psi_{m+1,a} + \sum_{a=n+1}^{N} q_a\Psi_{m+1,a}\right) + G_{fixed}$$

Ψ is analogous to Φ in the equations for solution potentials, but the values of Ψ_{1a} for site i are computed for the group in the context of the neutral protein structure rather than in isolation. G_{fixed} is a sum of all energy components which do not change when a charge is added to atom 1 or m+1. To calculate the total electrostatic energy of the protein in ionization state a, $x_\alpha(i)z_i$ is added to q_1 and $x_\alpha(j)z_j$ added to q_{m+1}. The difference in electrostatic energy between the arbitrarily ionized protein and the neutral protein reduces to

$$\Delta G_{prot,\alpha} = \tfrac{1}{2}x_\alpha(i)z_i^2\Psi_{11} + \tfrac{1}{2}x_\alpha(j)z_j^2\Psi_{m+1,m+1} + (x_\alpha(i)z_i)(x_\alpha(j)z_j)\Psi_{1,m+1}$$
$$+ x_\alpha(i)z_i\left(\sum_{a=1}^{m} q_a\Psi_{1a} + \sum_{a=m+1}^{n} q_a\Psi_{1a} + \sum_{a=n+1}^{N} q_a\Psi_{1a}\right)$$
$$+ x_\alpha(j)z_j\left(\sum_{a=1}^{m} q_a\Psi_{m+1,a} + \sum_{a=m+1}^{n} q_a\Psi_{m+1,a} + \sum_{a=n+1}^{N} q_a\Psi_{m+1,a}\right)$$

so, the difference in the electrostatic energy of ionization when i is transferred from the solution to the protein with $x_\alpha(j) = 0$ is

$$\Delta\Delta G_i = \tfrac{1}{2}(\Psi_{11} - \Phi_{11}) + z_i\left(\sum_{a=1}^{m} q_a(\Psi_{1a} - \Phi_{1a}) + \sum_{a=m+1}^{n} q_a\Psi_{1a} + \sum_{a=n+1}^{N} q_a\Psi_{1a}\right).$$

When the charge at j is equal to zero, only desolvation effects and interactions with the background of charges in the neutral protein affect the pKa of the protein; thus,

from $\Delta\Delta$Gi, the intrinsic pKa of site i can be calculated. This value, the pKa of the group in the hypothetical neutral protein is then

$$pKa_{int}(i) = pKa_{model}(i) - z_i \frac{\Delta\Delta G_i}{2.303RT}.$$

Similar equations apply to group j, and to any number of additional groups in an expanded analysis. In the case that both i and j are ionized, the additional electrostatic energy is $\Delta G_{ij} = z_i z_j \Psi_{1,m+1}$. For an ionization state α,

$$G_{elec,\alpha} = x_\alpha(i)\Delta\Delta G_i + x_\alpha(j)\Delta\Delta G_j + x_\alpha(i)x_\alpha(j)z_i z_j \Psi_{1,m+1}.$$

When this analysis is expanded to consider an arbitrary number M of sites, the number of these additional electrostatic energy terms is 2^M, the number of possible ionization states. The full expression for $G_{elec,\alpha}$, is then:

$$-\beta \sum_{i=1}^{n} x_\alpha(i) \left[\Delta\Delta G_i + \sum_{j>i}^{n} x_\alpha(j)\Delta G_{ij}\right]$$

where β=1/RT. Various methods for evaluation of this expression by enumeration of subsets of the possible ionization states, and their relative accuracy, will be discussed in the next chapter.

Knowledge-Based Potentials for Protein Structure Analysis and Prediction

David K. Tcheng[†^] and Shankar Subramaniam[†#*]

[†]Beckman Institute, National Center for Supercomputing Applications,
[^]Department of Computer Science,
[#]& Department of Physiology & Biophysics,
University of Illinois at Urbana-Champaign, Urbana, IL 61801

*Corresponding Author: Shankar Subramaniam
Beckman Institute
University of Illinois at Urbana-Champaign
405 N. Mathews Av.
Urbana, IL 61801
phone: (217) 244-4489
fax: (217) 244-2909
email: shankar@uiuc.edu

It is well known that the native conformation of a protein, in a given environment, is determined entirely by the various interatomic interactions dictated by the amino acid sequence (1,2). The determination of secondary and tertiary structures by the primary sequence has been called "the second coding problem", and is one of the most pressing problems in modern biology (3). Efforts to fold a protein from a random structure corresponding to its sequence have met with little success, to date. Using a well-defined set of high-resolution protein structures, we have derived statistical potentials, in the form of distance probability density functions, which describe the interatomic interactions of native proteins. When applied to highly randomized and noisy structures of proteins distinct from the basis set, native-like structures were obtained to very high precision (≤2Å). The examples tested include proteins of all sizes up to 461 amino acids long) and diverse topological structures (alpha, beta and alpha-beta classes). The potentials appear to define the protein energy landscape in a smooth manner and are sensitive enough to recognize subtle distortions from a native packing structure. They therefore also provide a powerful tool for refinement of X-ray derived structures at any degree of initial precision.

needs work

Efforts to fold a protein from a random structure corresponding to its sequence have met with little success. The objective of a number of these efforts has been to minimize an energy or free energy function that describes interatomic interactions (4-6) to obtain the folded protein structure. These energy functions have been obtained from theoretical or phenomenological considerations. The direct energy function methods include use of mechanics force-fields (7) and semi-empirical force

fields (8,9). The traditional molecular mechanics force fields use energy functions for bonds, angles, torsions and for pairwise nonbonded interactions. These have been employed for both local structure predictions and in conjunction with crystallographic data or distance-constraints obtained from magnetic resonance methods (10,11). Knowledge-derived potential functions have also been employed to fold protein sequences into structures to a limited degree of success. These include residue-based profiles (12,13), lattice models (14-16), threading methods (17-20) and homology models (21,22).

Statistical Potentials

The problem of describing a folded protein in terms of the optimal interatomic interactions can be inverted to obtain energy functions that are optimal for folded protein structures. A majority of these methods use high resolution protein structures to derive pairwise residue-level contact information or in a few cases atom level interactions (23,24). The knowledge of pairwise atomic contacts in known protein structures reflects the relative probability of finding atom pairs at specified distances and hence can provide a measure of the free energy of interaction. The theoretical foundations for this stem from the Boltzmann principle, which asserts that the probability of a given atomic configuration for a protein structure is related to the free energy. Minimizing the free energy of a protein is equivalent to maximizing concomitantly all the pairwise atomic distance probabilities.

We have used the above principle to develop statistically-derived potentials for refining and predicting protein structures. We derive the statistical potentials as probability density functions (PDFs) that describe the distribution of distances

between different groups of atoms. Each heavy atom in an amino acid is described as a group and the twenty amino acids yield 167 groups of atoms. The distance data for constructing the distributions is obtained from a database of 380 unique protein structures. The latter set is constructed from a larger database of protein structures by requiring each member of the unique set to have a resolution of less than 2.5 Å and any two members to have less than 50 percent sequence homology as defined by standard BLAST protocols (25). Distance examples are generated from this database for every pair of atomic contacts and these are used to construct the PDFs. The conditional pairwise distance PDFs take the form of Probability (X| R_i,A_k,R_j,A_l,S_n), where, X is the distance, R_i and R_j represent residue indices, A_k and A_l atom indices, and S_n represents the sequential distance between the residues R_i and R_j. The total probability of pairwise distance contacts in a protein is given by combining the conditional probabilities,

$$P(\text{protein}) = \prod_{k,l,i,j,S_n} P(X|R_i,A_K,R_j,A_l,S_n)$$

where the indices run over all atoms, residues and the specified sequential distances. The sequential distance is used so as to preserve the sequentially contiguous interactions that give rise to secondary structure in proteins. The case where n=0 represents the intra-residue PDFs which are a measure of the configurational and conformational geometry of the amino acid considered. We observe that for PDFs of atom pairs separated by more than 3 residues there are no specific secondary structure interactions and we consider these as tertiary PDFs.

A unique PDF is formed for each unique combination of R_i, R_j, A_k, A_l and S_n. For instance, P(X | Val,CG1,Leu,CD1,3) represents the PDF for Val CG1-Leu CD1 atom pairs for which the parent residues Val and Leu are sequentially in 1-3 positions. A key problem in deriving these potentials is the non-uniform distribution of pairwise

distances in the distance space. To overcome this limitation statistically rigorous methods of kernel density estimation and maximum likelihood evaluation are used to construct the PDFs (26). This method distributes the examples along the distance axis and slides a Gaussian kernel function across the distance axis while computing the weighted sum. The choice of the kernel width is based on a repeated cross-validation of the PDF performance and measurement of the accuracy in terms of the maximum likelihood. The result of this convolution is first normalized so that the area under the curve sums to unity. Further, squared distance division is carried out to obtain radial density normalization. In Fig. 1, we present examplar PDFs for 4 categories. The height of the resulting normalized PDF curve is a measure of the relative probability of finding two atoms belonging to two residues at the defined distance. In evaluations of protein structures, we subtract the expected mean logarithmic probability value corresponding to each PDF from the actual probability to assess how significantly better or worse that specific pair interaction is as compared to an average pair interaction of that type. Further, we can obtain either atomic or residue profiles of a protein, based on averaging over interactions of each atom or over each residue respectively and these profiles provide a relative measure of deviation from ideality of the interactions of the defined atom or residue in the context of the protein structure.

The PDF curves represent local structure and packing interactions in proteins. An ideal protein would have every pair of atoms in the regions of high or highest probability and thus possess optimal interactions. In general higher resolution protein structures have a better likelihood of higher pairwise atomic probabilities. In Table 1, we compare the total logarithmic probability scores averaged over all the pairwise interactions in the protein for 15 protein pairs, whose structures have been obtained at two resolutions. These proteins were not included in the 380 unique

protein set used to construct the PDFs. In each case the higher resolution protein structure has a higher probability score. In one case, where the structures had the same resolution, the one with a lower crystallographic R-factor had a higher probability score. To further illustrate the regions in the protein that have more ideal interactions as defined by the PDF scores, we show a comparison of the two structures and the residue-wise probability profiles of T4 phage lysozyme, 3lzm at 1.7 Å resolution and 1lzm at 2.4 Å resolution, in Fig. 2. The C-terminal domain is better resolved in 3lzm as reflected by the higher probability scores.

Annealing Noisy Protein Structures

An important use of the knowledge-based potentials is in the refinement of a non-native or poorly resolved protein structure to a native state. In conventional methods, optimization on an energy landscape is carried out to obtain the native protein structure. The potential functions that yield the energy landscape are based on either molecular mechanics-based, x-ray structure factors, NOE distance constraints or combinations of these (27). Molecular mechanics functions yield a very rough energy landscape and the resulting multiple minima render energy optimization complex. By virtue of being extremely specific, our statistical potentials, which describe each pairwise atomic interaction in accurate detail, yield a smooth and arguably unique minimum in the energy landscape and hence are ideally suited for folding non-native and noisy into native structures. We demonstrate the power of this method for diverse classes of proteins and suggest its possible use with low resolution x-ray or partial NOE data.

We use an annealing procedure to predict the structures of the proteins listed in Table 2, starting from noisy structures. Each of the initial structures was created

by adding noise to the x-ray structure. Noise was added by defining a sphere with a 10 Å radius around each atom and randomly relocating the atom within the sphere using a uniform sampling distribution, i.e., all points within the sphere were treated as equally likely.

Table 2 shows the r.m.s. deviations of the 15 proteins annealed from a randomized structure as compared to the x-ray structures. These proteins are chosen so as represent diversity in size, packing and fold. In all of the examples studied, a well-connected compact topological structure was formed in the early stages of annealing, i.e., within 50 steps of optimization and the resulting structures are similar to the x-ray structures. A large contribution to the small RMS deviations from the x-ray structures stem from the solvent exposed side-chain orientations. The PDFs do not take into account explicitly the protein-solvent interactions or crystal contacts. However, they improve the interactions in the protein interior so as to optimize packing.

In Fig. 3, we present the initial noisy, annealed and the x-ray structures of the two proteins, 461-residue glutathione reductase (3grs) and 162-residue dihydrofolate reductase (3dfr). In the latter, we also compare residue-averaged PDF profiles of the refined and the native x-ray structures. The x-ray structure has numerous improbable contacts, which are refined in the annealed structure.

In Fig. 4, we present the annealed and the x-ray structures of the protein cytochrome B562, (256b). We choose this protein to test the PDF potentials in assessing proteins that contain prosthetic groups. In the cytochrome B562, the non-inclusion of the prosthetic heme group in the PDF optimization does not appear to affect the overall structure. Fig. 3 shows that the side chain atoms of residues in

contact with the heme, Met 7, Asn 11, Phe 65, Arg 98 and Arg 106, reorient to provide better packing in the optimized structure which does not contain the heme group. Helices 3 and 4 in the native protein move towards each other so as to yield better packing. Despite the deviations in the local region near the prosthetic group, the rest of the protein is annealed to the native structure.

We examined the annealing of the protein structures with the PDF method, by following the folding process in bacteriophage T4 lysozyme. In Fig. 5, we present different stages of annealing of a noisy structure, with the colors representing the transition of the structure from low probability and consequently high energy to high probability interactions. The early stages of annealing produces compactness, while the secondary structures are formed within circa 50 steps. At 200 steps of annealing the protein has optimized close to the actual structure. The folding process shows the specificity and hence the accuracy of these statistical potentials for native protein structure.

In summary, we have developed statistical potentials that describe the folded state of proteins accurately. These potentials are independent of protein sequence homologies, secondary structures or folds and contain information at the fundamental level of pairwise atomic interactions specific for each pair of residues. The distance-based statistical potentials appear to be ideally suited for combining with x-ray and NMR structural refinement methods.

Methods

The January 1994 relase from the Brookhaven Protein Data Bank (3611 protein chain sequences) was used in building the non-homologous set of proteins. The

sequences were made into a BLAST database and each sequence was compared against all of the sequences in the database. A list of unique chains was selected from the BLAST set and compared for 50% identity. Amongst the homologous set, the highest resolution protein was chosen as a representative [28].

The total number of atom types corresponding to the heavy atoms in the twenty amino acids is 167. The pairwise atomic distance PDFs are generated for intra residue, residues related by positions, n-n+1, n-n+2 and n-n+3 and each of the other pairs, within 10 Å form the tertiary PDFs. The n-n+1, n-n+2 and n-n+3 and tertiary PDFS are computed seperately for N to C and C to N terminal directions. The PDFs are assumed independent of each other. The only additional PDF used is one corresponding to the S-S bond in disulfides. The total number of pdfs thus amount to 112,226 types and the number of atomic distance pairs in the 380 proteins considered are 80,670,588. The compressed PDFs occupy approximately 115 MBytes of storage. The computational time required for constructing all the pdfs is 268 hours on a single R8000 SGI processor. The annealing of medium sized protein from a random structure takes about 40 hours on a single R8000 processor.

The total normalized probability summed over all pairwise atomic probabilities was computed for all the 380 proteins data set chosen for PDF construction. It was found that there was a correlation between the total logarithmic probability and the resolution of the structures. The Spearman rank corelation for normalized probabilities yielded a Z-value of -5.6 and a P-value less than 0.0001.

In the annealing procedure, atoms are incrementally moved in the direction which maximizes probability of all the atom's interactions, weighting each interaction equally. In each step, atoms are moved one at a time and the order in which each

atom is moved is randomized each step. An atom is moved by defining a sphere of radius 0.2 Å around it, and randomly selecting 100 candidate points within the sphere using a uniform sampling distribution. The candidate points are evaluated one at a time and the difference between the candidate atom probability and current atom probability is calculated. The standard probabilistic simulated annealing acceptance criterion is used to determine when to move the atom. The only additional constraint used in addition to the distance PDFs was a torsional term that was biased towards the correct chirality for each amino acid. For these experiments, structures were predicted using 200 steps. The control parameters for annealing, the tertiary interactions weight, the chirality weight, and the temperature used for simulated annealing changed each step based on linear schedules. The weight of tertiary interactions was varied from 0.0 to 1.0, the weight of the chirality term varied from 0.08 to 0.01, and the temperature in normalized probability units varied from 1/32 to 1/1000.

Acknowledgements

We thank Drs. E. Jakobsson, S. Sligar, A. Crofts and C. Wraight for valuable discussions and Dr. J. Fenton for assistance with the figures. We gratefully acknowledge a metacenter computer allocation and computer resources at the National Center for Supercomputing Applications.

References and Notes

1. Anfinsen, C.B. Principles that govern the folding of protein chains. *Science* **181**, 223-230 (1973).

2. Dill, K.A. Dominant forces in protein folding. *Biochemistry* **29**, 7133-7155 (1990).

3. Lattman, E.E. and Rose, G.D. Protein folding - What is the question? Proc. Natl. Acad. Sci. U.S.A. 90, 439-441 (1993).

4. Levitt,M. and Warshel. A. Computer simulation of protein folding. *Nature* **253**, 694-698 (1975).

5. Godzik, A., Kolinski, A. and Skolnick, J. Are proteins ideal mixtures of amino acids - Analysis of energy parameter sets. *Protein Science* **10**, 2107-2117 (1995).

6. Elofsson, A., Le Grand, S.M., Eisenberg, D. Local moves - An efficient algorithm for simulation of protein folding. *Proteins: Struct. Funct. Genet.* **23**, 73-82 (1995).

7. McCammon, J.A. and Harvey, S.C., *Dynamics of Proteins and Nucleic Acids*. (Cambridge: Cambridge University Press, 1987).

8. Ponder, J.W. and Richards, F.M. Tertiary templates for proteins - Use of packing criteria in the enumeration of allowed sequences for different structural classes. *J. Mol. Biol.* **193**, 775-791 (1987).

9. Srinivasan, R. and Rose, G.D. LINUS: A hierarchic procedure to predict the fold of a protein. *Proteins: Struct. Funct. Genet.* **22**, 81-99 (1995).

10. Brunger, A.T., Kuriyan, J. and Karplus, M. Crystallographic R-factor refinement by molecular dynamics. Science 235, 458-460 (1987).

11. Branden, C.I. and Jones, T.A. Between objectivity and subjectivity. *Nature* **343**, 687-689 (1990).

12. Crippen, G.M. Prediction of protein folding from amino acid sequence over discrete conformation spaces. *Biochemistry* **30**, 4232-4237 (1991).

13. Luthy, R., Bowie, J.U. and Eisenberg, D. Assessment of protein models with three-dimensional profiles. *Nature* **356**, 83-85 (1992).

14. Sali, A., Shakhnovich, E. and Karplus, M. How does protein fold? *Nature* **369**, 248-251 (1994).

15. Dill, K.A., Bromberg, S., Yue, K., Fiebig, K.M., Yee, D.P., Thomas, P.D. and Chan, H.S. Principles of protein folding - A perspective from simple exact models. *Protein Sci.* **4**, 561-602 (1995).

16. Karplus, M. and Sali, A. Theoretical studies of protein folding and unfolding. *Curr. Opin. Struct. Biol.* **5**, 58-73 (1995).

17. Sippl, M.J. and Weitckus, S. Detection of native-like models for amino acid sequences of unknown three-dimensional structure in a data base of known protein conformations. *Proteins: Struct. Funct. Genet.* **13**, 258-271 (1992).

18. Jones, D.T., Taylor, W.R. and Thornton, J.M. A new approach to protein fold recognition. *Nature* **358**, 86-89 (1992).

19. Holm, L. and Sander, C. Protein structure comparison by alignment of distance matrices. *J. Mol. Biol.* **233**, 123-138 (1993).

20. Bryant, S.H. and Lawrence, C.E. An empirical energy function for threading protein sequence through the folding motif. *Proteins: Struct. Funct. Genet.* **16**, 92-112 (1993).

21. Hearst, D.P. and Cohen, F.E. GRAFTER - A computational aid for the design of novel proteins. *Prot. Eng.* **7**, 1411-1421 (1994).

22. Sali, A. and Blundell, T.L. Comparative protein modeling by satisfaction of spatial restraints. *J. Mol. Biol.* **234**, 779-815 (1993).

23. Sippl, M.J. Calculation of conformational ensembles from potentials of mean force. An approach to the knowledge-based prediction of local structures in globular proteins. *J. Mol. Biol.* **213**, 859-883 (1990).

24. Sun, S. Reduced representation model of protein structure prediction: Statistical potential and genetic algorithms. *Protein Sci.* **2**, 762-785 (1993).

25. Altschul, S.F., Gish, W., Miller, W., Myers, E.W. and Lipman, D.J. *J. Mol. Biol.* **215**, 403-410 (1990).

26. Hogg, R.V. and Tanis, E.A. *Probability and Statistical Inference* (New York: MacMillan Publ. Company, 1988).

27. Brunger, A. T. and Nilges, M. Computational challenges for macromolecular structure determination by x-ray crystallography and solution NMR-spectroscopy. *Q. Rev. Biophys.* **26**, 49-125 (1993).

28. Walsh, L.L. *An annotated guide to the Brookhaven Protein Databank, classification and comparisons of protein structures.* (Doctoral Dissertation Submitted to the University of Illinois, 1994).

FIGURE CAPTIONS

1. Representative PDFs for Val CG1-Leu CD1 atom pairs. N, N+1 represents adjacent Val-Leu residues, N,N+2 those seperated by one residue, N,N+3 those seperated by two and > N, N+3 stands for all other Val CG1-Leu CD1 atom pairs. The PDFs are first normalized to unity and then by radial density.

2. Comparison of (A) three dimensional structures of T4 phage lysozyme at 2.4 (1LZM) and 1.7 Å (3LZM) resolution, color coded by distance probability. The color scale is from blue to red, with red colors indicating higher probability pairwise atomic contacts. (B) residue profiles of 3LZM and 1LZM. The positive log(Probability) values indicate better pairwise atomic contacts averaged over all atoms for the residue. The C-terminal domain of 3LZM is better refined than that of 1LZM.

3. (A) Comparison of the randomized, annealed and x-ray structure of the 461-residue glutathione reductase (3grs). Only Ca atoms are displayed. (B) Comparison of the annealed and x-ray structures of the 162-residue dihydrofolate reductase (3dfr). The atoms are color coded by averaged atomic probability based on the pairwise interactions of the specified atom with all other atom pairs; the color scale in terms of probability goes from blue to red. The x-ray structure has numerous improbable contacts (colored in blue), which are corrected in the annealed structure (colored in red). (C) Residue-wise probability profiles for the x-ray and refined dfr structures.

4. Comparison of the x-ray and annealed structures of cytochrome B562 (256b). Helices are represented by cylinders and the side chains that repack in PDF-based

annealing are represented by spheres. The x-ray structure shows the heme group and the packing of the side chains and the annealed structure shows the packing reorganization; the heme group was not considered in the PDF-based annealing.

5. Structures of T4 phage lysozyme at different stages of annealing are shown. The color coding is from blue to red (low to high probabilities). The randomized structure anneals to a compact structure in the early stages and to secondary structures in the first 50 steps. The structure after 200 steps of annealing has achieved most of the secondary structure in the actual protein and has probabilities close to those in the x-ray structure.

Table 2. RMS Deviation and Total Probabilities of Refined Proteins. The RMSDs refer to comparison of the x-ray structure.

Protein	Number of Residues (Number of Atoms)	All Atom-RMSD in Å (random)	All Atom-RMSD in Å (refined)	Back-bone Atom-RMSD in Å	^Total dist. log(prob)
Pancreatic Trypsin Inhibitor(9pti)	58 (453)	7.826	1.998	1.557	-0.026
Alpha Bungarotoxin (3ebx)	62 (474)	7.849	2.040	1.496	-0.042
Cytochrome B5 (3b5c)	85 (692)	7.810	2.085	1.696	-0.001
Plastocyanin (1plc)	99 (737)	7.803	2.024	1.633	-0.030
Parvalbumin (4cpv)	108 (806)	7.791	2.180	1.636	0.001
Cytochrome B562 (256b)	106 (825)	7.782	1.913	1.475	0.036
Pseudoazurin (2aza)	129 (975)	7.784	2.128	1.558	-0.028
Proteinase A (2sga)	181 (1258)	7.751	2.129	1.657	-0.041
Dihydrofolate Reductase (3dfr)	162 (1293)	7.743	1.930	1.517	-0.017
Lysozyme (3lzm)	164 (1308)	7.741	2.081	1.610	0.006
Alpha-Lytic Protease (2alp)	198 (1390)	7.738	2.144	1.618	-0.040
Actinidin (2act)	218 (1645)	7.754	2.312	1.801	-0.038
Acid Proteinase (2apr)	325 (2402)	7.787	2.142	1.687	-0.027
Thermolysin (3tln)	316 (2431)	7.784	2.051	1.655	-0.014
Glutathione Reductase (3grs)	461 (3498)	7.777	2.157	1.652	-0.016

^ The total distance log (probability) is both mean value and r-squared normalized.

Table 1. Comparison of Total Probabilities of Low and High Resolution Protein Pairs

Protein	PDB Name (Resolution in Å)	Total distance log(prob)	PDB Name (Resolution in Å)	^Total distance log(prob)
Pancreatic Trypsin Inhibitor	3pti(1.50)	-0.0043	9pti(1.22)	-0.0037
Alpha Bungarotoxin	2ebx(1.40)	-0.0230	3ebx(1.40)	-0.0178
Cytochrome B5	2b5c(2.00)	0.0215	3b5c(1.50)	0.0338
Plastocyanin	1pcy(1.60)	-0.0113	1plc(1.33)	-0.0082
Parvalbumin	1cpv(1.85)	-0.0052	4cpv(1.50)	0.0361
Cytochrome B562	156b(2.50)	-0.0165	256b(1.40)	0.0877
Pseudoazurin	1aza(2.00)	-0.0324	2aza(1.80)	-0.0230
Proteinase A	1sga(2.80)	-0.0472	2sga(1.50)	-0.0141
Dihydrofolate Reductase	1dfr(2.50)	-0.1858	3dfr(1.70)	-0.1221
Lysozyme	1lzm(2.40)	-0.0142	3lzm(1.70)	0.0421
Alpha-Lytic Protease	1alp(2.80)	-0.0510	2alp(1.70)	-0.0192
Actinidin	1act(2.80)	-0.2524	2act(1.70)	-0.0045
Acid Proteinase	1apr(2.50)	-0.1147	2apr(1.80)	-0.0064
Thermolysin	1tln(2.30)	-0.8905	3tln(1.60)	0.0082
Glutathione Reductase	2grs(2.00)	-0.1496	3grs(1.54)	0.0016

^ The total distance log (probability) is both mean value and r-squared normalized.